Search for excited muons in the process $pp \rightarrow \mu\mu^* \rightarrow \mu\mu Z \rightarrow 4\mu$ with CMS data

von

THOMAS ESCH

MASTERARBEIT IN PHYSIK

vorgelegt der
FAKULTÄT FÜR MATHEMATIK, INFORMATIK UND NATURWISSENSCHAFTEN
DER RHEINISCH-WESTFÄLISCHEN TECHNISCHEN HOCHSCHULE AACHEN

im Januar 2014

angefertigt am
III. PHYSIKALISCHEN INSTITUT A

bei
PROF. DR. THOMAS HEBBEKER

Zweitgutachter
PROF. DR. CHRISTOPHER WIEBUSCH

Abstract

Some theories concerning new physics predict the existence of a substructure of leptons and quarks. Such a substructure could answer some of the open questions addressed to the Standard Model of Particle Physics. Therefore, many searches for excited fermions are performed at particle colliders, also at the LHC experiments CMS and ATLAS.

This thesis presents a search for excited muons in the channel $\mu\mu^* \to \mu\mu Z \to 4\mu$ where the μ^* is produced together with a Standard Model muon via contact interaction. The analysis is based on the complete 2012 dataset of proton-proton collisions recorded by the CMS experiment and corresponds to an integrated luminosity of 19.7 fb^{-1} at a center-of-mass energy of $\sqrt{s} = 8$ TeV. For this purpose, several selection criteria have been implemented to distinguish between signal and background, also taking into account influences of a Z-boson decay to nearby muons. Since there is no deviation from the Standard Model expectation, an exclusion limit has been set as a function of the compositeness scale Λ for the coupling parameters $f = f' = 1$ and $f = -f' = -1$. The existence of excited muons can be excluded up to $M_{\mu^*} = 1.64$ TeV for $f = f' = 1$ and $M_{\mu^*} = 1.85$ TeV for $f = -f' = -1$ (95 % C.L.) assuming a compositeness scale of $\Lambda = M_{\mu^*}$. In addition, a combination with the channel $\mu\mu^* \to \mu\mu Z \to 2\mu 2e$ has been performed, yielding a limit of $M_{\mu^*} > 1.75$ for $f = f' = 1$ and $\Lambda = M_{\mu^*}$.

Zusammenfassung

In einigen Theorien über neue Physik wird die Existenz einer Substruktur von Leptonen und Quarks vorhergesagt. Eine solche Substruktur könnte manche der offenene Fragen an das Standardmodell der Teilchenphysik beantworten. Deswegen werden an Teilchenbeschleunigern viele Suchen nach angeregten Fermionen durchgeführt, auch an den beiden LHC Experimenten CMS und ATLAS.

In dieser Arbeit wird eine Suche nach angeregten Myonen im Kanal $\mu\mu^* \to \mu\mu Z \to 4\mu$ präsentiert, wobei das μ^* gemeinsam mit einem Standardmodell-Myon durch Kontaktwechselwirkung produziert wird. Die Analyse basiert auf dem vollständigen Datensatz an Proton-Proton Kollisionen der 2012 vom CMS Experiment aufgenommen wurde und einer integrierten Luminosität von 19.7 fb^{-1} bei einer Schwerpunktsenergie von $\sqrt{s} = 8$ TeV entspricht. Zu diesem Zweck wurden mehrere Selektionsschritte eingebaut um das Signal vom Untergrung unterscheiden zu können, auch unter Beachtung des Einflusses von Zerfällen eines Z-Bosons in nahe beieinander liegende Myonen. Da keine Abweichung vom erwarteten Untergrund beobachtet werden konnte, wurde eine Ausschlussgrenze in Abhängigkeit von der Substrukturskala Λ für die Parameter $f = f' = 1$ und $f = -f' = -1$ gesetzt. Die Existenz von angeregten Myonen kann bis zu einer Masse von $M_{\mu^*} = 1.64$ TeV für $f = f' = 1$ und $M_{\mu^*} = 1.85$ TeV für $f = -f' = -1$ (95 % C.L.) bei einer Substrukturskala von $\Lambda = M_{\mu^*}$ ausgeschlossen werden. Zusätzlich wurde noch eine Kombination mit dem Kanal $\mu\mu^* \to \mu\mu Z \to 2\mu 2e$ durchgeführt, die zu einer Ausschlussgrenze von $M_{\mu^*} > 1.75$ für $f = f' = 1$ und $\Lambda = M_{\mu^*}$ führt.

Contents

1. Introduction

In particle physics, the Standard Model describes the interaction of particles using the weak, strong and electromagnetic interaction with a very high accuracy. But there are still open questions that cannot be answered by the Standard Model, for example why do leptons and quarks have a similar structure in their different generations or why do leptons have an electric charge of minus one (charged leptons) and zero (neutrinos) while quarks have a charge of -2/3 and 1/3. These are some of the main reasons why there are many models predicting compositeness of leptons and quarks. One of these models describes the production and decay of excited fermions at hadron colliders introducing a new strong interaction between possible substructure-particles which is called contact interaction.

In nature, there are many examples for the existence of excited states. Atoms which are built out of electrons, protons and neutrons, do have excited states as well as baryons and mesons which are constructed by quarks. In all cases, the excited states are a consequence of compositeness. For this reason, a discovery of excited leptons or quarks that are expected to be pointlike particles in the Standard Model could show evidence for an unknown substructure of these particles.

In this thesis, a search for excited muons in the decay channel $\mu\mu^* \to \mu\mu Z \to 4\mu$ for data collected with the Compact Muon Solenoid (CMS) experiment at the Large Hadron Collider (LHC) will be presented. It is the first time that a search is performed in another channel than the "golden channel" $\mu\mu^* \to \mu\mu\gamma$ which has a higher cross section, but also a higher background. In theory, it is also possible to produce excited muons without a decay into photons. Therefore, an additional search with another decay channel is useful.

The next chapter will give a brief summary of the Standard Model and its weaknesses, followed by the description of the investigated model.
Chapter four will present a short overview of the experimental setup, namely the LHC and the CMS experiment. Here, also the detector components of the CMS detector will be described.
The fifth chapter discusses the reconstruction of muons, especially of high-p_T and nearby muons followed by the description of the analysis framework and the used data samples in chapter six.
Chapter seven then shows the different steps of the analysis including the selection of the signal and the data to background comparison. Here, also more detailed studies concerning boosted Z-bosons to two nearby muons will be presented.
Afterwards, the final selection will be applied and the results will be presented in chapter eight followed by a summary with a short outlook in chapter nine.

2. Theoretical Foundations

In this chapter, a brief summary of the Standard Model of Particle Physics will be presented. If not indicated otherwise, it is based on [1] and [2].

2.1. The Standard Model of Particle Physics

As far as known, there are three kinds of particles: Leptons and quarks (fermions) that form matter and bosons which transmit forces. While fermions are particles with spin 1/2, bosons have an integer spin. The Standard Model of Particle Physics (SM) describes how these particles build matter and how they interact with each other. It has been tested with a high precision several times and withstood many tests. Although it does not describe all observed phenomena (see Sec. 2.2), its predictions are very accurate.

Three out of four forces are explained in the SM: The electromagnetic, strong and weak force. Although the gravity is added in the list of forces (Tab. 2.1), it is not part of the SM yet. All interactions are transmitted by bosons: The photon (γ) is the mediator of the electromagnetic, the gluon (g) of the strong and the $Z^0/W^\pm$ - bosons of the weak interaction. While there is only one type of photons, eight types of gluons are needed to describe the strong interaction. Not every particle interacts via all forces, it depends on its quantum numbers: Only electrically charged particles can interact via electromagnetic force while the strong interaction only affects particles carrying colour charges. The weak interaction can act on leptons as well as on quarks. While the Z^0 describes the neutral current of the weak force, the $W^\pm$ appears in charged currents. One example for the weak interaction is the decay of neutrons to protons ($n \rightarrow p + e^- + \bar{\nu}_e$). A list of all forces with their corresponding mediators is given in Tab. 2.1.

Force	Mediator	Charge	Spin	Mass (GeV)	Range (m)
Strong	Gluon (g)	0	1	0	10^{-15}
Electromagnetic	Photon (γ)	0	1	0	∞
Weak	$Z^0/W^\pm$	0 / $\pm$ 1	1	91.2 / 80.2	10^{-18}
Gravitational	Graviton (G)	0	2	0	∞

Table 2.1.: List of forces, bosons and their corresponding attributes in order of decreasing strength.

For leptons as well as for quarks three generations or families are observed. Each lepton family consists of one charged lepton (e, μ, τ) and one uncharged neutrino (ν_e, ν_μ, ν_τ). Tab. 2.2 shows the three families and the corresponding leptons. Not added in this table are anti-leptons which have the opposite characteristics, for example positive instead of negative charges. In particle processes, the number of leptons of one family and the global lepton number are conserved. The charged leptons can interact via electromagnetic and weak forces while neutrinos only interact weakly.

Just the same as leptons, each family of quarks consists of two particles: one up-like quark with charge 2/3 and one down-like quark with charge -1/3. Tab. 2.3 summarizes the quark

Generation	Lepton	Charge	Spin	Mass
I.	Electron (e^-)	-1	1/2	511 keV
	Electron neutrino (ν_e)	0	1/2	< 2 eV
II.	Muon (μ^-)	-1	1/2	105.7 MeV
	Muon neutrino (ν_μ)	0	1/2	< 0.19 MeV
III.	Tau (τ^-)	-1	1/2	1.78 GeV
	Tau neutrino (ν_τ)	0	1/2	< 18.2 MeV

Table 2.2.: List of leptons and their attributes [3].

generations and their characteristics. Unlike leptons, quarks do have a colour charge. There are three types of colour charges: red (r), blue (b) and green (g). In a free state, particles can only exist with a neutral colour charge. Therefore, quarks can only be observed in bound states of three quarks (baryons, for example protons and neutrons) or one quark and one anti-quark (mesons, for example π^0).

Generation	Quark	Charge	Spin	Mass
I.	Up (u)	2/3	1/2	$2.3^{+0.7}_{-0.5}$ MeV
	Down (d)	-1/3	1/2	$4.8^{+0.7}_{-0.3}$ MeV
II.	Charm (c)	2/3	1/2	1.28 ± 0.03 GeV
	Strange (s)	-1/3	1/2	95 ± 5 MeV
III.	Top (t)	2/3	1/2	$173.5 \pm 0.6 \pm 0.8$ GeV
	Bottom (b)	-1/3	1/2	4.18 ± 0.03 GeV

Table 2.3.: List of quarks and their attributes [3].

2.1.1. Gauge Theories

The Standard Model of Particle Physics is formulated as a relativistic local gauge theory, namely a quantum field theory (QFT). It describes the electromagnetic, strong, and weak interaction using a $U(1)_Y \times SU(2)_L \times SU(3)_C$ symmetry group where $U(1)_Y \times SU(2)_L$ stands for the electroweak part (Sec. 2.1.3) and $SU(3)_C$ for the strong interaction.

In classical mechanics, the motion of a particle can be described by the Euler-Lagrange equation

$$\frac{d}{dt}\left(\frac{\partial L}{\partial \dot{q}}\right) = \frac{\partial L}{\partial q_i} \tag{2.1}$$

with the 'Lagrangian' $L = T - U$ where T is the kinetic and U is the potential energy of the particle. While in classical mechanics the equation describes the motion of particles, one is also interested in the way how the gauge fields interact with particles in quantum field theory. Therefore, an Euler-Lagrange equation which is a function of the fields and their position (x, y, z) and time (t) derivatives is formulated:

$$\partial\left(\frac{\partial \mathscr{L}}{\partial\left(\partial_\mu \phi_i\right)}\right) = \frac{\partial \mathscr{L}}{\partial \phi_i} \qquad (i = 0, 1, 2, 3)\,. \tag{2.2}$$

The Lagrangian $\mathscr{L} = \frac{1}{2}\left(\partial_\mu \phi\right)\left(\partial^\mu \phi\right) - \frac{1}{2}m^2\phi^2$ leads to the Klein-Gordon equation for scalar (Spin-0) fields ϕ

$$\partial_\mu \partial^\mu \phi + m^2 \phi = 0 \qquad \text{(Klein-Gordon equation)} \tag{2.3}$$

where m is the particle mass. If the Lagrangian $\mathscr{L} = i\bar{\psi}\gamma^\mu \partial_\mu \psi - m\bar{\psi}\psi$ is used, the result is the Dirac equation which describes a spinor (Spin-$\frac{1}{2}$) field ψ

$$\left(i\gamma^\mu \partial_\mu - m\right)\psi = 0 \qquad \text{(Dirac equation)}. \tag{2.4}$$

The Dirac equation is important because it describes the fermions of the Standard Model. The idea behind the formulation of the SM as a gauge theory is to make it invariant under global and local phase transformation:

$$\psi \to e^{i\theta}\psi \qquad \text{(global phase transformation)} \tag{2.5}$$

$$\psi \to e^{i\theta(x)}\psi \qquad \text{(local phase transformation)}. \tag{2.6}$$

If the global phase transformation is used on the Dirac Lagrangian and inserted into the Euler-Lagrange equation, it is invariant, but if a local phase transformation is applied, additional terms that do not cancel out appear. To make the Standard Model invariant under local phase transformations, the Lagrangian has to be modified by introducing terms that remove these contributions. This will be discussed in the following sections.

2.1.2. Quantum Electrodynamics

Quantum electrodynamics (QED) describes the interaction of electrically charged particles. As explained in Sec. 2.1.1, the Dirac Lagrangian is not invariant under local phase transformation. Since quantum electrodynamics shall also be formulated as a local gauge theory for an accurate description, the Dirac Lagrangian cannot be used the way it is. Using a local phase transformation on the Dirac Lagrangian results in

$$\mathscr{L} \to \mathscr{L} - \left(\partial_\mu \theta\right)\bar{\psi}\gamma^\mu \psi. \tag{2.7}$$

To make the Lagrangian of the QED locally invariant, the partial derivative ∂_μ is replaced by the covariant derivative

$$D_\mu = \partial_\mu + ieA_\mu(x) \tag{2.8}$$

where A_μ is a vector field (Spin 1) with the transformation

$$A_\mu(x) \to A_\mu(x) + \frac{1}{e}\partial_\mu \theta(x). \tag{2.9}$$

This vector field has to be massless and represents the photon (γ) which is the mediator of the electromagnetic interaction. The Lagrangian is now locally invariant, but a additional kinetic term describing the free propagation of the new vector field A_μ has to be introduced. The complete **QED Lagrangian** is:

$$\mathscr{L}_{QED} = \left[i\bar{\psi}\gamma^\mu\partial_\mu\psi - m\bar{\psi}\psi \right] - \left[\frac{1}{4}F^{\mu\nu}F_{\mu\nu} \right] - \left(e\bar{\psi}\gamma^\mu\psi \right) A_\mu. \tag{2.10}$$

The first two terms represent the free Dirac equation, the third and the fourth term are added to guarantee local gauge invariance. $F^{\mu\nu}$ is defined by $F^{\mu\nu} = (\partial^\mu A^\nu - \partial^\nu A^\mu)$. All in all, QED is a U(1) symmetry group which means it is invariant under unitary transformations U:

$$\psi \to U\psi, \qquad \text{with} \quad U^\dagger U = 1. \tag{2.11}$$

In this case, $U = e^{i\theta(x)}$. The gauge field of QED is not charged, this means photons do not interact with each other, except for higher orders in the perturbation theory. This is different for quantum chromodynamics[1] (QCD) where the gluons are colour charged and therefore couple to each other.

2.1.3. Electroweak Unification

The electroweak interaction unifies the weak with the electromagnetic interaction by using a combined formalism. It is formulated as a U(1) × SU(2) gauge theory with spontaneous symmetry breaking. The weak interaction consists of two parts: Charged currents (CC) which are transmitted by $W^\pm$-bosons and neutral currents (NC) that are connected to Z^0-bosons. In contrast to neutral currents, charged currents can change the flavour of quarks and leptons:

$$n(udd) \to p(uud) + W^- \to p(uud) + e^- + \bar{\nu}_e \qquad \text{(neutron decay)} \tag{2.12}$$
$$\mu^- \to \nu_\mu + W^- \to \nu_\mu + e^- + \bar{\nu}_\mu \qquad \text{(muon decay)}. \tag{2.13}$$

The weak interaction is described by quantum flavour dynamics (QFD). In contrast to QED and QCD, the weak interaction is parity violating. While interactions with charged currents are maximally parity violating, neutral currents are less violating except for interactions with neutrinos. The W-boson interacts only with left-handed particles and right-handed anti-particles. Therefore, the symmetry group used for the weak interaction is $SU(2)_L$ where the L stands for left-handed. While the electromagnetic and strong interactions depend on the electric and colour charge, the charge of the weak interaction is the weak isospin T. The $SU(2)_L$ group predicts three particles where the third one should be the neutrally charged Z^0. This leads to a problem: According to the theory, the Z^0 should only interact with left-handed fermions, but a coupling to right-handed fermions is observed, too.

The solution is a combination of the electromagnetic and weak interaction since the electromagnetic current also includes left- and right-handed components. Using this, the neutral currents can be described as a combination of left-handed current from the $SU(2)_L$ and right-handed currents from $U(1)_Y$ group. Here, Y stands for the hypercharge which is related to the third component of the weak isospin T^3 and the electric charge Q by

$$Q = T^3 + \frac{Y}{2} \qquad \text{(Gell-Mann-Nishijima formula)}. \tag{2.14}$$

The combined group is a $U(1)_Y \times SU(2)_L$ symmetry group. It predicts four bosons: W_μ^1, W_μ^2, W_μ^3 and B_μ where the first two bosons are charged while the other two are neutral. Now, the

---

[1]Quantum Chromodynamics is the formalism to describe the strong interaction.

known bosons can be reconstructed from the four gauge fields by using the electroweak mixing angle θ_W:

$$W_\mu^\pm = \frac{1}{\sqrt{2}} \left(W_\mu^1 \mp i W_\mu^2 \right) \tag{2.15}$$

$$A_\mu = B_\mu \cos\theta_W + W_\mu^3 \sin\theta_W \tag{2.16}$$

$$Z_\mu = -B_\mu \sin\theta_W + W_\mu^3 \cos\theta_W \tag{2.17}$$

Here, $W_\mu^\pm$ are the W-bosons, A_μ is the photon and Z_μ the Z-boson. The electroweak mixing angle is not predicted and has been measured to

$$\sin^2\theta_W = 0.23 \qquad \text{(Weinberg angle)}. \tag{2.18}$$

With the combination of weak and electromagnetic interactions, all three forces of the Standard Model can be described as local gauge symmetries. But there is still one problem: According to the electroweak theory, the W- and Z-bosons have to be massless for local gauge invariance while measurements show a mass of 80.4 GeV and 91.2 GeV. This problem can be solved by introducing the Higgs Mechanism (Sec. 2.1.4).

2.1.4. The Higgs Mechanism

The Standard Model of Particle Physics can describe the interactions of bosons and fermions, but there are still some problems in this theory. One open question addresses the masses of the gauge bosons Z^0 and $W^\pm$: To guarantee local gauge invariance, they have to be massless which is a contrast to the measured masses of 80.4 GeV and 91.2 GeV. A solution for this problem is given by the Higgs mechanism that is based on spontaneous symmetry breaking. The idea is to add a new field to the Lagrangian which fulfills the Klein-Gordon equation. It is given by

$$\phi = \frac{1}{2} \left(\phi_1 + i\phi_2 \right). \tag{2.19}$$

The potential of the field has to be symmetric:

$$V(\phi) = \mu^2 \phi^* \phi + \lambda \left(\phi^* \phi \right), \qquad \text{with } \lambda > 0 \text{ and } \mu^2 < 0. \tag{2.20}$$

It has the form of a "mexican hat" (Fig. 2.1) with its ground state at $\phi \neq 0$. In the ground state, the gauge symmetry is spontaneously broken. The corresponding Lagrangian of the new scalar field is

$$\mathscr{L} = \frac{1}{2} \left(\partial_\mu \phi \right) \left(\partial^\mu \phi \right) + \frac{1}{2} \mu^2 \phi^2 - \frac{1}{4} \lambda^2 \phi^4. \tag{2.21}$$

With the new gauge field (Higgs field), the Standard Model Lagrangian obtains new terms that explain the mass of the gauge bosons without loosing its local invariance since the Lagrangian stays symmetric while the ground does not. As a result, a new massive particle that is referred to as Higgs boson is predicted. In addition to this important feature, it can also explain the masses of the fermions which makes this theory much more interesting.
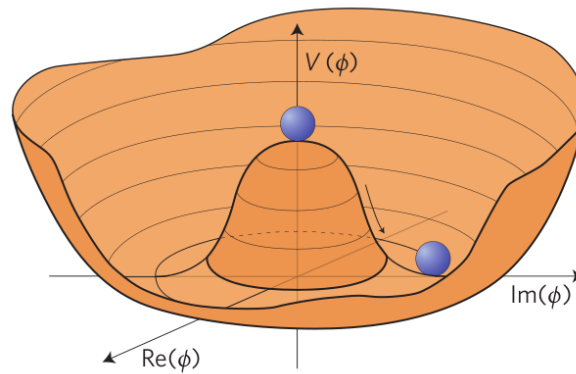
Figure 2.1.: Mexican hat potential of the Higgs field, taken from [9].

In July 2012, the observation of a new particle with a mass of about 125 GeV which is compatible with the Higgs boson was announced by the two LHC experiments CMS and ATLAS [4, 5]. Although the characteristics of the observed particle are very similar to the expectation of the Higgs boson, additional measurements have to be performed. More advanced results with the full 2012 dataset and a higher number of investigated decay channels are also compatible with the Higgs boson [6, 7]. As a result of this discovery, Francois Englert and Peter Higgs who proposed main parts of this theory are the winners of the Nobel Price of Physics 2013 [8].

2.2. Beyond the Standard Model

Although the predictions of the Standard Model have been tested and confirmed many times, it still has some shortcomings of which some will be described in this section.

First of all, the Standard Model describes three out of four known forces. The strength of these forces highly depends on the energy of the corresponding interaction. In case of the electroweak force, it is possible to unify two of these forces, but there is no known formalism to include also the strong force. One of the main targets for the future will be to find a way to describe all three forces in a Great Unified Theory (GUT) leading to the unification of all couplings at a certain energy scale. In addition to this problem, the fourth force, gravitation, is still not part of the Standard Model yet. Therefore, it is also not possible to explain why gravity is so much weaker than the other three forces. Its couplings get important at the Planck scale where a new theory concerning quantum gravitation has to be developed.

Another question addresses the mass of the Higgs boson. For the Standard Model Higgs boson, a mass at the electroweak scale has to be given. Since the Higgs boson is a scalar boson, loop corrections contribute to its mass which lead to a quadratic divergent term. To realize a Higgs mass below 1 TeV, the effect of this term has to be neglected. One theory to realize this is the so called Supersymmetry (SUSY) which introduces an additional fermion for each boson and an additional boson for each fermion.

The next question targets the structure of the Standard Model. It is known why the fermions of the Standard Model are ordered in at least three families, but it is not known why there are exactly three observed generations. Therefore, searches for additional generations of fermions

are performed at particle accelerators. The next question that cannot be answered is why each generation has the same structure with the same type of particles and charges and why there is such a huge difference in the mass of the particles.

These are some of the main shortcomings of the Standard Model, but there are still some more, like the question for Dark Matter and Dark Energy, the mass of neutrinos, the question why there is more matter than antimatter observed in the universe and others. To find at least some answers to these questions, different analyses search for new particles or effects that could lead to a solution for some of the problems. The following chapters will focus on a search for a substructure of leptons.

3. Excited Leptons

One of the main questions of particle physics that cannot be answered by the Standard Model is why do we observe exactly three generations of quarks and leptons and why is there the same structure in each family? Why does every lepton generation consist of two parts, one charged object with high mass (e, μ, τ) and one uncharged object with small mass (ν_e, ν_μ, ν_τ)?

These questions could be answered if quarks and leptons would possess a substructure (compositeness). This substructure would lead to excited states of these fermions [10–14]. There are many examples where excited states can be observed in nature, for example atoms, but also mesons and baryons have excited states. The possible substructure of quarks and leptons can be the same in both cases and is characterized by a new strong interaction described by the scale Λ.

3.1. Theoretical Setup

Excited fermions are expected to have a spin and an isospin of $\frac{1}{2}$. The only theoretical difference between excited electrons and muons is the mass of the particles. It is assumed that excited leptons and neutrinos form a weak isospin doublet [10]

$$\begin{pmatrix} \nu_l \\ l^- \end{pmatrix}_L, \quad l_R^- \begin{pmatrix} \nu_l^* \\ l^{*-} \end{pmatrix}_L, \quad \begin{pmatrix} \nu_l^* \\ l^{*-} \end{pmatrix}_R. \tag{3.1}$$

This scenario allows excited leptons to acquire masses prior to SU(2) × U(1) symmetry breaking and to limit the number of parameters [12, 14]. The quantum numbers of excited and ordinary leptons are expected to be the same and to be conserved in the production and decay processes. Excited leptons can couple to other fermions via contact interaction which results from the interaction between the subcomponents. It strongly depends on the energy scale of the substructure Λ (compositeness scale) and can be described by the effective four-fermion Lagrangian

$$\mathscr{L}_{CI} = \frac{g_*^2}{2\Lambda^2} j^\mu j_\mu \tag{3.2}$$

with the current

$$j_\mu = \eta_L \bar{f}_L \gamma_\mu f_L + \eta_L' \bar{f}_L^* \gamma_\mu f_L^* + \eta_L'' \bar{f}_L^* \gamma_\mu f_L + h.c. + (L \to R) \tag{3.3}$$

where f and f^* represent the Standard Model and the excited fermions and γ_μ the gamma matrices. Here, it is assumed that the coupling of the substructure g_*^2 is equal to 4π. The η-factors for left-handed currents are set to one and the η-factors for right-handed currents are set to zero for simplicity. Additionally to the coupling via contact interaction, excited fermions can also interact to each other via gauge interaction. For excited leptons, the Lagrangian is given by

$$\mathscr{L}_{Gauge} = \bar{f}^* \gamma^\mu \left(g \frac{\tau}{2} W_\mu + g' \frac{Y}{2} B_\mu \right) f^* \tag{3.4}$$

where W_μ and B_μ describe the SU(2) and U(1) gauge fields and $g = e/\sin\theta_W$ and $g' = e/\cos\theta_W$ are the electroweak gauge couplings. The effective Lagrangian which describes the transition between excited and ordinary states via gauge interaction is given by

$$\mathscr{L}_{trans} = \frac{1}{2\Lambda} \bar{f}^*_R \sigma^{\mu\nu} \left(gf \frac{\tau}{2} W_{\mu\nu} + g'f' \frac{Y}{2} B_{\mu\nu} \right) f_L + H.c. \tag{3.5}$$

Here, $W_{\mu\nu}$ and $B_{\mu\nu}$ are the field-strength tensors of the SU(2) and U(1) gauge fields and

$$\sigma^{\mu\nu} = \frac{i}{2} \left(\gamma^\mu \gamma^\nu - \gamma^\nu \gamma^\mu \right) \tag{3.6}$$

is a commutator of gamma matrices. The factors f and f' are parameters which depend on the compositeness dynamics. Normally, the setting $f = f' = 1$ is investigated in analyses, but $f = -f' = -1$ is an interesting case, too. In contrast to the gauge coupling of excited leptons that is independent from the compositeness scale, the coupling of excited leptons to ordinary leptons is a function of $1/\Lambda$.

3.2. Production of excited leptons

There are two ways to produce excited leptons [12–14]. The first way is the production via gauge interaction. In this case, a rise to the three signatures $l^*\bar{l}$, $l^*\nu$ (single production) and $l^*\bar{l}^*$ (double production) is given. The second way is the production via contact interactions. Here, the excited leptons can also be produced together with a standard model lepton ($l^*\bar{l}$) or in pairs ($l^*\bar{l}^*$). At hadron colliders, the ratio of excited leptons produced via gauge interactions with respect to the number produced via contact interactions is smaller than 1% [11,15] for l^*-masses above the Z-boson mass and a compositeness scale Λ of a few TeV. For much higher Λ, the gauge production would become more important, but searches in this region cannot be realized at the LHC since the cross section is too low. Therefore, the concentration will be on the production of excited leptons via contact interaction. In Fig. 3.1, the feynman diagram for excited lepton production in pp-collisions is shown.
The parton cross sections for single and double excited lepton production are [10,11]

$$\hat{\sigma}\left(q\bar{q} \to l\bar{l}^*, l^*\bar{l}\right) = \frac{\pi}{6\hat{s}} \left(\frac{\hat{s}}{\Lambda^2}\right)^2 \left(1 + \frac{v}{3}\right) \left(1 - \frac{M_{l^*}^2}{\hat{s}}\right)^2 \left(1 + \frac{M_{l^*}^2}{\hat{s}}\right) \sim \frac{1}{\Lambda^4} \tag{3.7}$$

$$\hat{\sigma}\left(q\bar{q} \to l^*\bar{l}^*\right) = \frac{\pi\tilde{v}}{12\hat{s}} \left(\frac{\hat{s}}{\Lambda^2}\right)^2 \left(1 + \frac{\tilde{v}^2}{3}\right) \sim \frac{1}{\Lambda^4} \tag{3.8}$$

with

$$v = \frac{\hat{s} - M_{l^*}^2}{\hat{s} + M_{l^*}^2}, \qquad \tilde{v} = \left(1 - 4\frac{M_{l^*}^2}{\hat{s}}\right)^{1/2} \tag{3.9}$$

where $\hat{s}$ is the center-of-mass energy of the parton system and M_{l^*} the excited lepton mass. The decay of excited leptons (Sec. 3.3) leads to final states which can be reconstructed with small backgrounds like for example $ll\gamma$, $4l$ or $2l2j$ in case of single production and $ll\gamma\gamma$, $6l$, $2l4j$ or $4l2j$ in case of double production.
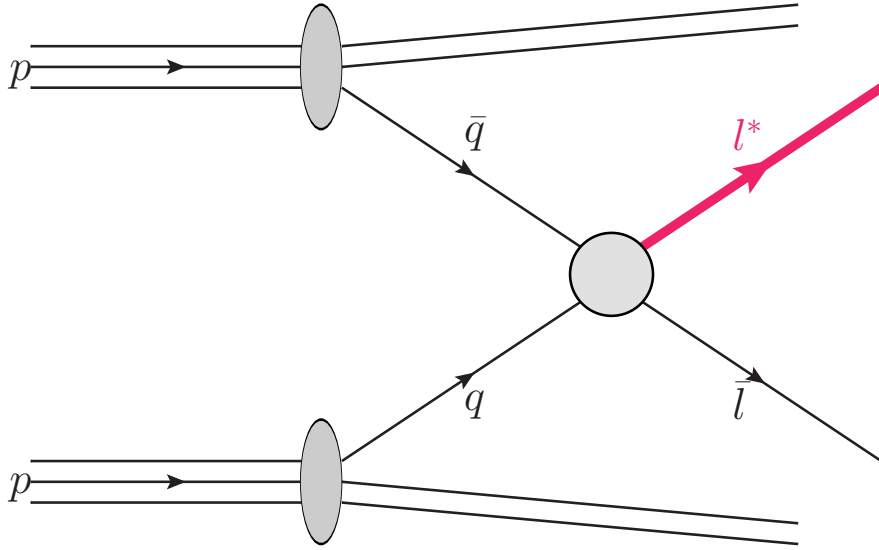
Figure 3.1.: Single excited lepton production together with a Standard Model lepton via contact interaction.

3.3. Decay of Excited Leptons

Excited leptons can decay in two different ways. The first way is the decay via gauge interaction. In this case, excited leptons emit a gauge boson (γ, $W^{\pm}$, Z^0) which leads to a final state of a lepton (a neutrino case of $W^{\pm}$ radiation) and the decay products of the gauge bosons. For example, if the Z^0-boson decays to two leptons, a four lepton final state is given based on the three leptons from the l*- and Z^0-decay and the additional lepton that was produced together with the excited lepton. The second way is the decay via contact interaction. Here, the excited lepton decays directly to a lepton and two fermions which means that it can also result in four leptons, but with a different kinematic than the decay via Z radiation. Fig. 3.2 shows the feynman diagrams of all possible excited lepton decays.

Starting with the decay via gauge interaction, one obtains the decay widths [10, 11]

$$\Gamma_G\left(l^* \to lV\right) = \frac{\alpha_V}{4} \frac{M_{l^*}^3}{\Lambda^2} f_V^2 \left(1 - \frac{M_V^2}{M_{l^*}^2}\right)^2 \left(1 + \frac{M_V^2}{2M_{l^*}^2}\right) \qquad (V = \gamma,\ W,\ Z) \qquad (3.10)$$

with $f_\gamma = fT_3 + f'Y/2$, $f_W = f/\sqrt{2}$ and $f_Z = fT_3\cos^2\theta_W - f'(Y/2)\sin^2\theta_W$. Here, T_3 is the third component of the weak isospin and Y the hypercharge. The coupling constants for the W- and Z-boson decay widths are

$$\alpha_W = \frac{\alpha_\gamma}{\sin^2\theta_W} \qquad \text{and} \qquad \alpha_Z = \frac{\alpha_W}{\cos^2\theta_W} = \frac{\alpha_\gamma}{\sin^2\theta_W \cos^2\theta_W} \qquad (3.11)$$

where θ_W is the electroweak mixing angle. Here, $\alpha_\gamma \approx 1/128$ is used because the energy scale of the compositeness is expected to be beyond the Z-boson mass. Since the photon is massless, the terms in the brackets of Eq. 3.10 are neglected for this case. For $M_{l^*} \gg M_V$ (V = W, Z), the terms with $\frac{M_V^2}{M_{l^*}^2}$ can also be neglected and the total decay width of the gauge interaction decay [10] approximately forms to
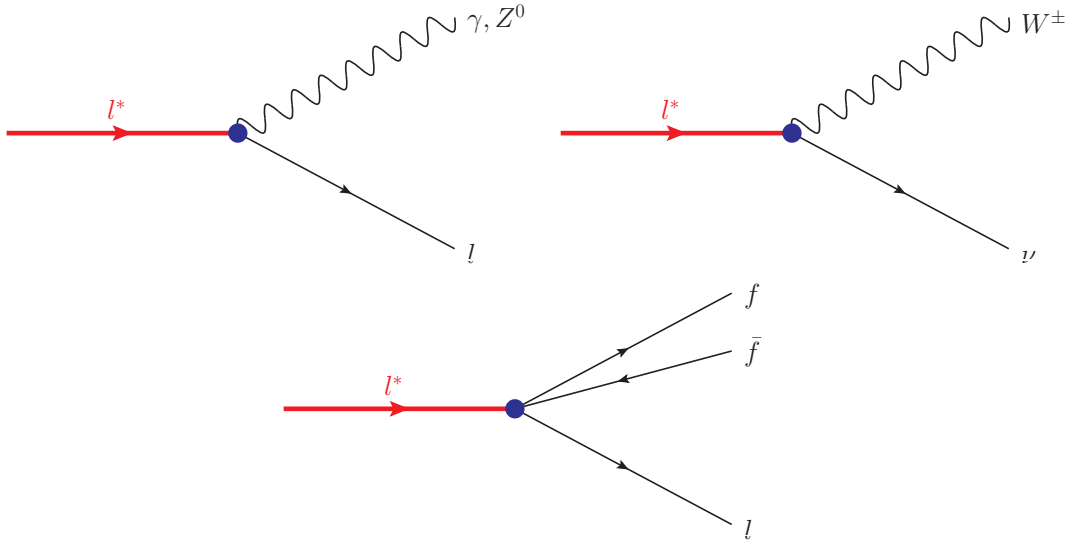
Figure 3.2.: Decay modes of excited leptons. Upper left: Decay to a photon/Z^0-boson and a lepton; Upper right: Decay to a $W^\pm$-boson and a neutrino; Bottom: Decay via contact interaction to a lepton and two fermions.

$$\Gamma_G\left(l^* \to all\right) \simeq \frac{1}{4}\frac{M_{l*}^3}{\Lambda^2}\left(\alpha_\gamma f_\gamma^2 + \alpha_W f_W^2 + \alpha_Z f_Z^2\right). \tag{3.12}$$

Since the decay widths of the three gauge decays have all a M_{l*}^3/Λ^2 dependence, the branching ratio of them is independent from this term and is constant for $M_{l*} \gg M_V$ [10, 11]. Tab. 3.1 shows the branching ratios for different l^* masses if only the gauge decays are considered. Fig. 3.3 and Fig. 3.4 show the branching ratio of gauge decays for all channels and for the case of leptonic decays (here: γ, e, μ). It can be seen that the photon decay width becomes zero for $f = -f' = -1$ meaning that there is the possibility of excited lepton production without any photon radiation.

The decay via contact interaction leads to a more complicated model. Its width is given by

$$\Gamma_C\left(l^* \to l + f\bar{f}\right) = \frac{1}{96\pi}N_C S\frac{M_{l*}^5}{\Lambda^4} \tag{3.13}$$

where N_C is the number of colours of fermions. For quarks it is equal to three and for leptons equal to one. The factor S depends on the type of the two fermions:

M_{l*} (GeV)	BR($l^* \to l\gamma$)	BR($l^* \to \nu W$)	BR($l^* \to lZ$)
100	0.73 (0.0)	0.26 (0.86)	0.01 (0.14)
250	0.32 (0.0)	0.58 (0.62)	0.10 (0.38)
500	0.29 (0.0)	0.60 (0.61)	0.11 (0.39)
1000	0.28 (0.0)	0.61 (0.61)	0.11 (0.39)

Table 3.1.: Branching ratio of gauge decays for different l^* masses with respect to the sum of all gauge decays for $f = f' = 1$ ($f = -f' = -1$).

Figure 3.3.: Branching ratio of the gauge decay channels of excited muons as a function of the invariant mass M_{l*} for $f = f' = 1$ ($f = -f' = -1$) on the left (right) side.
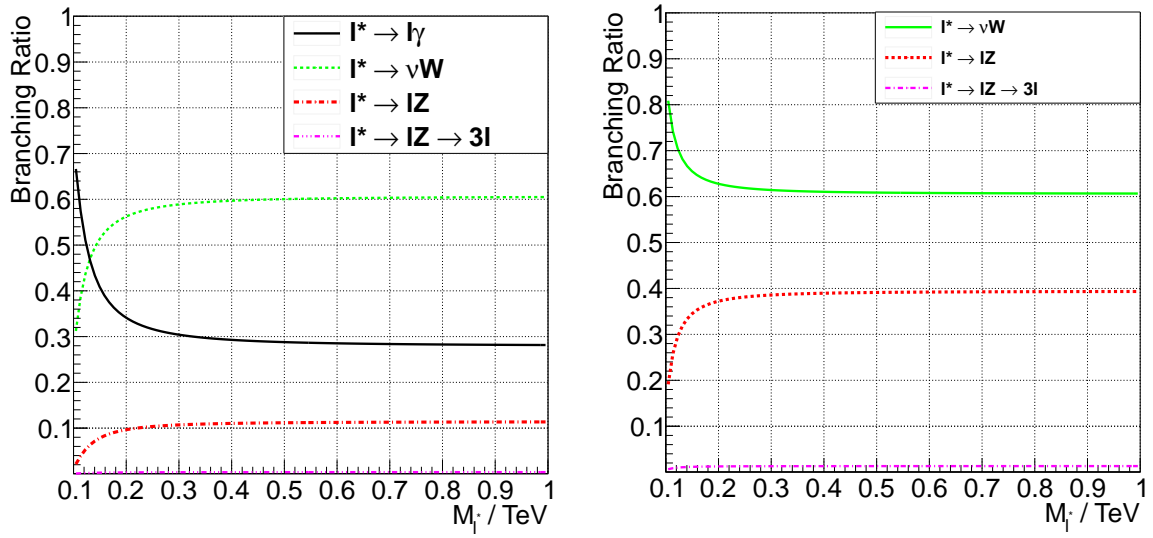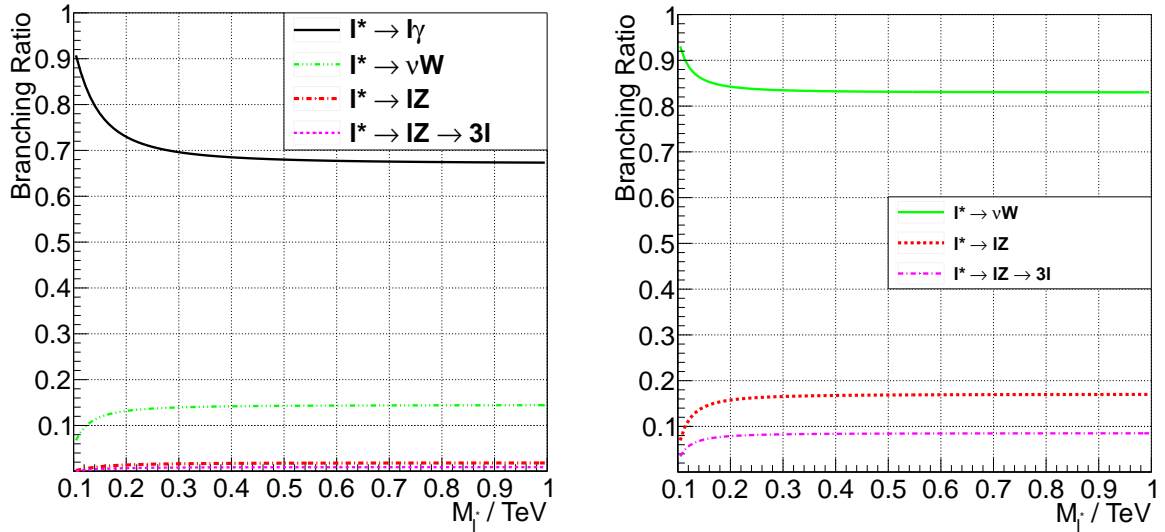

Figure 3.4.: Branching ratio of the gauge decay channels of excited muons as a function of the invariant mass M_{l*} for $f = f' = 1$ ($f = -f' = -1$) on the left (right) side. Here, only the decays to leptons (l = e, μ) and photons (γ) are included.

$$S = 1 \qquad \text{for} \qquad f = q \ \text{ and } \ l' \neq l \tag{3.14}$$

$$S = 2 \qquad \text{for} \qquad f = l. \tag{3.15}$$

Since the contact interaction decay has a different dependence of the term M_{l*}/Λ in contrast to the gauge decays, the full branching ratio is also given as a function of this term. Fig. 3.5 shows the full branching ratio including the contact interaction decay for $f = f' = 1$. For low masses with respect to Λ, the gauge decays are dominant while for high masses the contact interaction decay dominating. In Tab. 3.2, a summary of branching ratios for different masses is presented.

M_{l*} (GeV)	Γ_{tot} (GeV)	Γ_G/Γ_{tot}	Γ_C/Γ_{tot}
100	8.56 ($2 \cdot 10^{-4}$)	0.08 (0.98)	0.92 (0.02)
250	22.3 ($6 \cdot 10^{-3}$)	0.08 (0.95)	0.92 (0.05)
500	44.7 (0.06)	0.08 (0.84)	0.92 (0.16)
1000	89.9 (0.76)	0.08 (0.57)	0.92 (0.43)
2000	180 (13.9)	0.08 (0.25)	0.92 (0.75)
3000	270 (90.5)	0.08 (0.13)	0.92 (0.87)
4000	360 (360)	0.08 (0.08)	0.92 (0.92)

Table 3.2.: Comparison of the branching ratios of the gauge interaction and the contact interaction decay for $\Lambda = M_{l*}$ ($\Lambda = 4$ TeV).
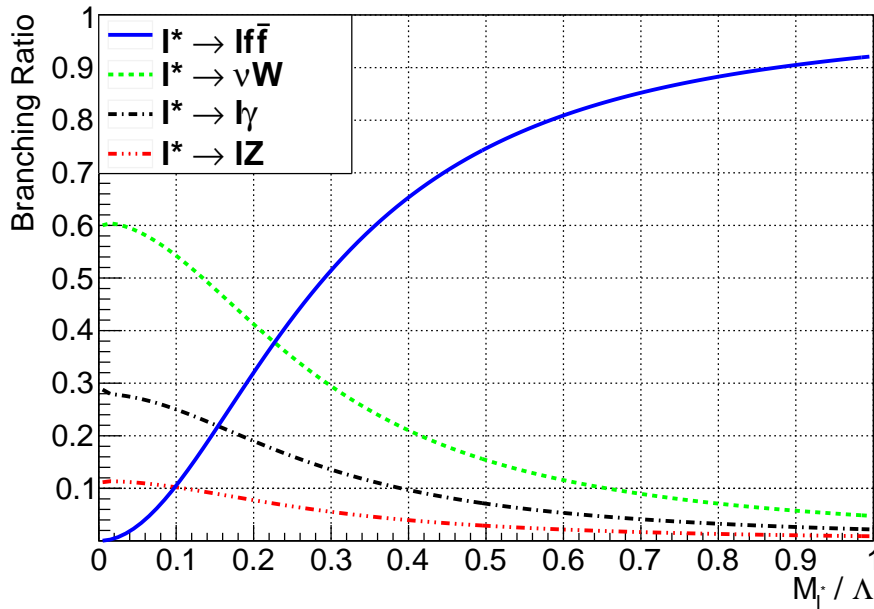

Figure 3.5.: Branching ratio of different decay channels of excited muons as a function of M_{l*}/Λ. Here, $M_{l*} \gg M_{\mathrm{W/Z}}$ is used.

3.4. Existing Limits

Many experiments have provided searches for excited lepton production at previous colliders. The four LEP experiments performed searches for the production and decay of excited leptons via gauge production by investigating the single excited lepton production as well as the excited lepton pair production. Since excited lepton pair production is independent from Λ, f, and f', a direct limit on the excited lepton mass can be calculated. The single excited lepton production via gauge interaction is depending on $|f/\Lambda|$ and therefore, limits on the coupling $|f/\Lambda|$ are set as a function of M_{l*} for this case:

- ALEPH has excluded excited leptons (e^*, μ^*, and τ^*) for masses below 65 GeV from pair production. Under the hypothesis of $M_{l*} = 130$ GeV, a limit on the coupling $\lambda/M_{l*} = \frac{f}{\sqrt{2}\Lambda}$ was set to $\lambda/M_{l*} < 0.04$ GeV^{-1} (μ^*, τ^*) and $\lambda/M_{l*} < 0.0007$ GeV^{-1} (e^*). The searches were performed in the $ll\gamma\gamma$ (pair) and $ll\gamma$ (single) decay channel [16].

- OPAL could exclude excited leptons from pair production for masses below 91 GeV ($f = f'$) and 86 GeV ($f = -f'$). The coupling $|f/\Lambda|$ has been excluded below $(10^{-4} - 10^{-1})$ GeV^{-1} for masses between 100 and 200 GeV from single production. In addition to the decay to photons, the hadronic channels of the W and Z decay were used for the analysis [17].

- The exclusion limits from L3 and DELPHI are similar. Excited leptons below 103 GeV are excluded by the DELPHI experiment (L3: 101.5 GeV) from pair production and $|f/\Lambda| < (10^{-4} - 10^{-1})$ GeV^{-1} for $M_{l*} = (100\text{-}200)$ GeV from single production. In addition to channels used by OPAL, the invisible decay of the Z-boson was included [18, 19].

Since HERA is a electron-proton collider, only searches for excited electrons could be performed by the experiments ZEUS and H1. Here, only the single production of excited electrons was investigated:

- ZEUS has excluded excited electrons up to a mass of $M_{e*} = 228$ GeV under the hypothesis $\frac{f}{\Lambda} = \frac{1}{M_{e*}}$. Here, only the production via gauge interaction was included [20].

- The analysis at H1 was performed by including the production via gauge and contact interaction. This analysis is also the only one including the decay of the Z-boson to leptons. In contrast to the analysis described in this theses, a final state of three leptons has been investigated at H1 while here, four leptons are selected. The decay via contact interaction was neglected which means that the result is conservative. For the scenario $f = f' = 1$, a limit was set on $\frac{1}{\Lambda}$ below $(10^{-4} - 10^{-2})$ GeV^{-1} for $M_{l*} = (100\text{-}290)$ GeV [21].

The two experiments CDF and D0 at the Tevatron did also perform searches for excited leptons. Here, the production via contact interaction was the dominant process:

- CDF included the production via gauge and contact interaction. The analysis was performed in the $ll\gamma$ channel for electrons and muons. In case of contact interaction production, excited muons can be excluded for 107 GeV $< M_{\mu*} <$ 853 GeV ($\Lambda = M_{\mu*}$) by CDF. The exclusion limit for gauge production from CDF is 100 GeV $< M_{\mu*} <$ 410 GeV ($\frac{f}{\Lambda} = 0.01$ GeV^{-1}) [22].

- D0 has performed only a search with production via contact interaction in the $ll\gamma$ channel. Excited muons have been excluded up to $M_{\mu*} = 618$ GeV for $\Lambda = 1$ TeV [23].

The newest and best limits on excited muons are from the CMS and ATLAS collaborations. CMS excluded excited muons with 5 fb $^{-1}$ data at $\sqrt{s} = 7$ TeV [24] for the range

$$M_{\mu^*} > 1.9 \text{ TeV for } \Lambda = M_{\mu^*}. \tag{3.16}$$

The exclusion limit from ATLAS is

$$M_{\mu^*} > 2.2 \text{ TeV for } \Lambda = M_{\mu^*} \tag{3.17}$$

for 13 fb^{-1} data at $\sqrt{s} = 8$ TeV [25]. Fig. 3.6 shows the exclusion limit from the ATLAS experiment. As far as known, there are no limits for the four lepton final state of excited leptons, only a search in a three lepton final state has been performed [21].
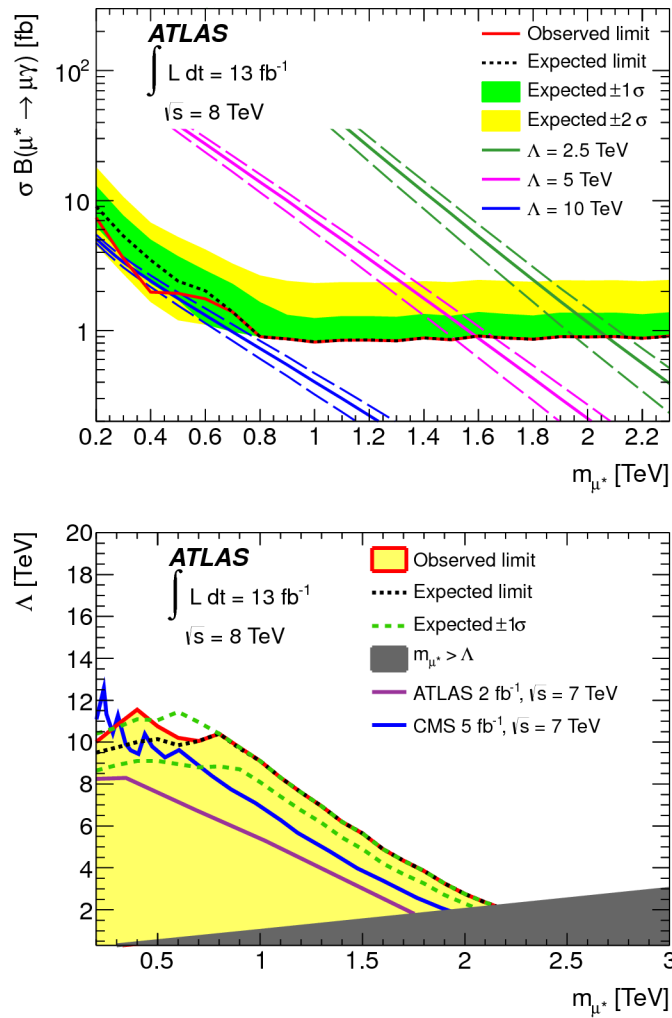

Figure 3.6.: Exclusion limits for excited muon production in the $\mu\mu\gamma$ channel from the ATLAS experiment with 13 fb^{-1} data at $\sqrt{s} = 8$ TeV. Left: Cross section limit; right: Limit on the compositeness scale Λ [25]

.

4. Experimental Setup

In this chapter, a short overview on the experimental setup is given. It describes the Large Hadron Collider (LHC) and the Compact Muon Solenoid (CMS) that were used to produce and collect the data for this analysis.

4.1. The Large Hadron Collider

The LHC [26] was developed with a design luminosity of $\mathscr{L} = 10^{34}$ cm^{-2}s^{-1} and a center-of-mass energy of $\sqrt{s} = 14$ TeV for proton-proton collisions ($\mathscr{L} = 10^{27}$ cm^{-2}s^{-1} and $\sqrt{s} = 2.75$ TeV per nucleon for lead-lead ion collisions). It was built in the LEP[1] [27] tunnel and has a circumference of 26.7 km which makes it the largest collider with the highest energy of the world. The event production rate $\dot{N}$ is given by

$$\dot{N} = \mathscr{L} \cdot \sigma \tag{4.1}$$

where σ is the cross section and $\mathscr{L}$ the instantaneous luminosity. The full number of expected events for a certain theory can then be written as $N_{theory} = \mathscr{L}_{int} \cdot \sigma_{theory}$, using the integrated luminosity $\mathscr{L}_{int} = \int \mathscr{L} \, dt$. The instantaneous luminosity per interaction region is given by

$$\mathscr{L} = \frac{N_b^2 n_b f_{rev} \gamma_r}{4\pi \epsilon_n \beta^*} F \tag{4.2}$$

where all parameters are machine parameters: N_b is the number of particles per bunch, n_b the number of bunches per beam, f_{rev} the revolution frequency, γ_r the relativistic gamma factor, ϵ_n stands for the normalized transverse beam emittance, β^* represents the beta function at the collision point, and F the geometric luminosity reduction factor which is given by $F = \left(1 + \left(\frac{\theta_c \sigma_z}{2\sigma^*}\right)^2\right)^{-\frac{1}{2}}$. In this case, θ_c is the full crossing angle at the interaction point, σ_z the RMS bunch length and σ^* the transverse RMS beam size [26].

There are four main experiments placed at the LHC: ATLAS [28], CMS [29], LHCb [30] and ALICE [31]. The first two experiments are high luminosity experiments that try to collect as much data as possible. Both where developed to find the Higgs boson and to search for supersymmetry (SUSY) and other exotic particles. LHCb does not collect the same amount of data as CMS and ATLAS, it is optimized for the investigation of physics including bottom-quarks. The last detector, ALICE, was developed for the investigation of lead-lead ion and proton-lead ion collisions. Fig. 4.1 shows the LHC accelerator complex with its experiments and injectors. It starts with the linear collider LINAC 2 where the protons are accelerated to an energy of 50 MeV. Afterwards, different colliders are used to increase the energy of the protons, starting with the Proton Synchrotron Booster (1.4 GeV) which is followed by Proton Synchrotron (25 GeV) and the Super Proton Synchrotron (450 GeV) before the LHC increases the energy to 7 TeV. For the data collection 2012 an energy of 4 TeV per proton was used.

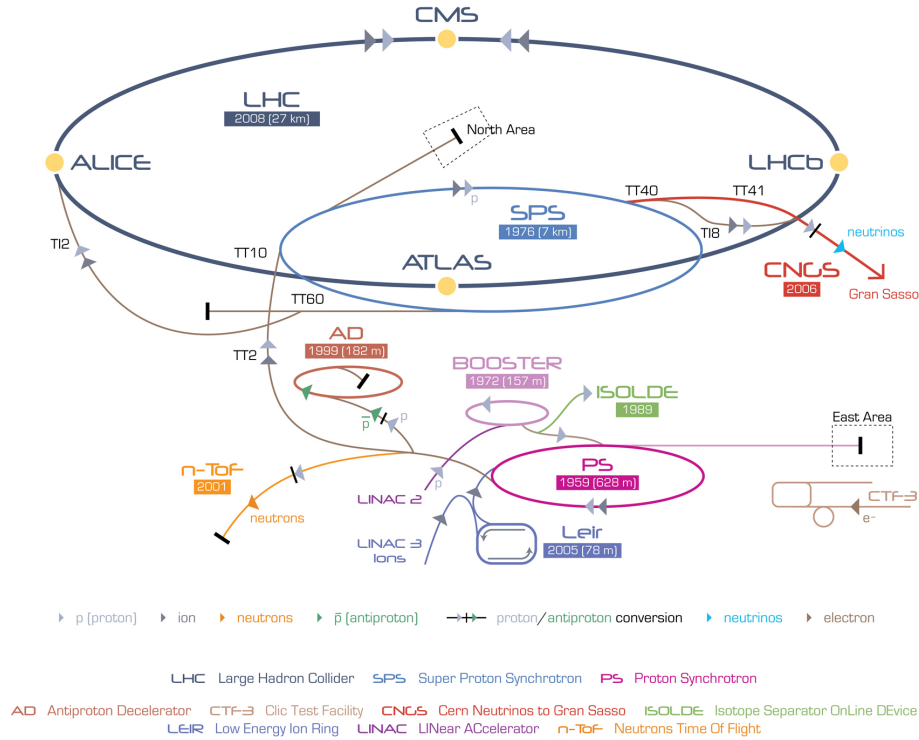
[1]Large Electron-Positron Collider

Figure 4.1.: The CERN accelerator complex with its experiments and injectors [32].

4.2. The Compact Muon Solenoid

The Compact Muon Solenoid (CMS) [29] is a multi-purpose apparatus at the LHC. It is located about 100 metres underground at the french site of the LHC and has a diameter of 14.6 m and a length of 16 m. The experiment was developed to detect as many different kinds of particles as possible. Therefore, it tries to achieve a full 4π coverage around the interaction point. It consists of two parts: The central part is called "barrel" and the forward parts are called "endcaps". The main requirements of the CMS detector are [29]:

- Accurate muon identification and momentum resolution for muons with low and high transverse momentum (p_T)

- Good charged particle momentum resolution and reconstruction efficiency

- Good electromagnetic energy resolution

- Accurate missing-transverse-energy measurement and dijet-mass resolution.

The CMS detector is built out of different subdetectors. Main parts are the inner tracker for the momentum determination that is supported by a strong solenoid magnet with a field strength of 3.8 T (it also includes the ECAL and parts of the HCAL), the electromagnetic and hadronic calorimeter (ECAL and HCAL) for energy measurements and the muon chambers that are used for the identification of muons. Fig. 4.2 shows the CMS detector with its main components.

4.2.1. The Coordinate System of CMS

The origin of the coordinate system used by CMS is the nominal collision point in the beam pipe. The x-axis radially points to the center of the LHC while the y-axis points vertically to the
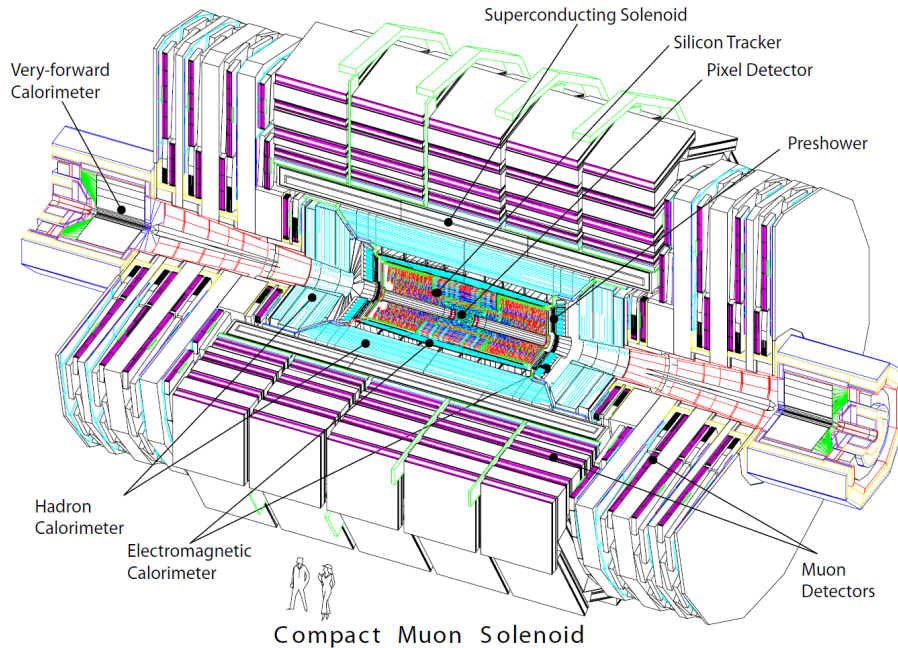
Figure 4.2.: Schematic view of the CMS detector, taken from [33].

surface of the earth and the z-axis is orientated along the beam direction to the Jura mountains. The azimuthal angle ϕ is measured from the x-axis in the x-y plane and the radial coordinate in this plane is represented by r. The angle measured from the z-axis in the y-z plane is the polar angle θ. Instead of θ one can also use the pseudorapidity

$$\eta = -\ln\tan\left(\frac{\theta}{2}\right) \tag{4.3}$$

which has the advantage of Lorentz invariance in z-direction for the spatial difference $\Delta\eta = \eta_1 - \eta_2$ of two highly boosted ($E \gg m$) objects. As a possibility to describe distances in the detector, one uses

$$\Delta R = \sqrt{(\Delta\eta)^2 + (\Delta\phi)^2}. \tag{4.4}$$

This variable defines a distance between two particles and can be used for different measurements (Sec. 7).

4.2.2. Inner Tracker

Here, the inner tracker of the CMS experiment will be described, based on [34]. Two parts form the inner tracker: A pixel detector and a strip detector. Fig. 4.3 shows a schematic overview of the tracking system of CMS. It was developed for a high number of particles per bunch crossing and for the measurement of a momentum of charged particles up to $|\eta| < 2.5$ based on their bending by the magnetic field. Another purpose is the reconstruction of decay vertices with a very high precision. Both goals are archived by detecting the hits produced by charged particles in the pixel and strip detectors. Due to the short time between two bunch crossings (25 ns), the tracker has to have a fast response time. For these reasons, the tracker is based on silicon and
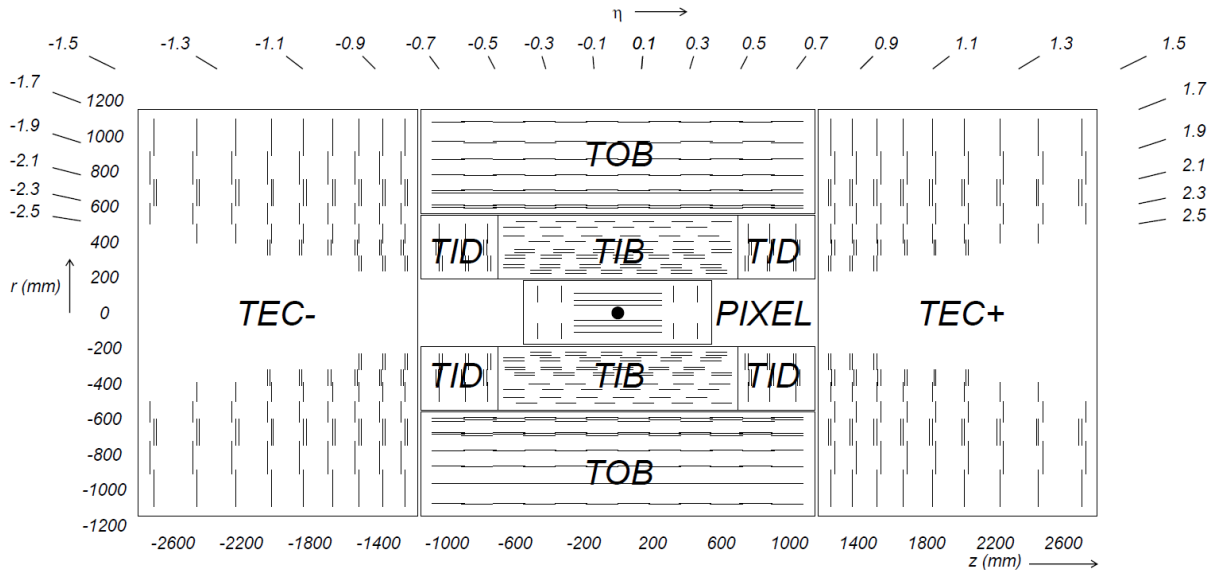
Figure 4.3.: Scheme of the CMS inner tracking system [29].

placed close to the beamspot, 4.4 cm apart from the interaction point.

The pixel detector

The pixel detector is built out of 66 million silicon pixels with a size of 100×150 μm^2 that are distributed over three layers in the barrel and two disks in the endcap region. It is the inner part of the tracking system and important for a good reconstruction of the primary and decay vertices (for example of b-jets), but also for the measurement of the transverse momentum. The pixel detector can measure coordinates in two dimensions and reaches a spatial resolution of 15 μm.

The strip detector

The outer part of the tracking system is the strip detector whose main task is the determination of the transverse momentum of charged particles by using the curvature caused by the magnetic field of the solenoid. In contrast to the pixel detector, it has a lower density of tracker layers. The strip detector consists of different sub-components: The tracker inner barrel (TIB), tracker inner disks (TID) and tracker outer barrel (TOB) that form the barrel region ($|\eta| < 0.9$) and the tracker endcaps (TEC) in the endcap region ($0.9 < |\eta| < 2.5$).

In contrast to the pixel detector, the strip detector can only measure coordinates in one direction. This problem is covered by adding strip modules to some layers with a stereo angle of 100 mrad that make a measurement in z-direction possible. In the central region of the detector the momentum resolution is 1-2 % for particles with a transverse momentum of about 100 GeV. For the outer region and particles with higher momentum [29], the resolution decreases because of higher distances between the tracker layers and a p_T dependence of the resolution $\left(\frac{\sigma_{p_T}}{p_T} \propto p_T \right)$.

4.2.3. Calorimeters

The CMS experiment consists of two calorimeters which are important for the measurement of the energy of different particles. The inner one is the electromagnetic calorimeter (ECAL) and the outer one is the hadronic calorimeter (HCAL). While the ECAL is completely covered by the inner magnetic field of the solenoid, the HCAL has a tail catcher outside of the magnet.

Electromagnetic Calorimeter

The main task of the electromagnetic calorimeter (ECAL) [35] is the measurement of the energy deposit of electrons and photons in a range of $\eta < 3.0$. It is built out of 75848 tungstate (PbWO$_4$) crystals with a length of 230 mm, a density of 8.28 g/cm^3 and a radiation length of $X_0 = 0.89$ cm which results in nearly 26 radiation lengths for each crystal. The high number and density of the crystals lead to a fast calorimeter response with a precise measurement of the energy deposit of electrons and photons. With a light radiation of 80% in 25 ns, the ECAL is close to the design bunch crossing time of the LHC. Avalanche photodiodes in the barrel region and vacuum phototriodes in the endcaps are used to detect light. An incoming particle produces an electromagnetic shower that excites the material of the ECAL which afterwards emits light. This light can then be detected by the photodetectors to measure the energy of the particle. At the endcaps in front of the ECAL, preshower detectors are applied. They are used to distinguish between photons from π^0-decays and photons from the hard interaction. The granularity of those preshower detectors is even higher than in the ECAL to distinguish two nearby photons from boosted π^0-decays.

The resolution of the ECAL gets better for higher energies because of the rising number of particles from the electromagnetic shower. This leads to higher statistics for the energy measurement. The resolution is given by

$$\left(\frac{\sigma_E}{E}\right)^2 = \left(\frac{a}{\sqrt{E}}\right)^2 + \left(\frac{\sigma_n}{E}\right)^2 + c^2. \tag{4.5}$$

The first term contains the stochastic effects of the energy deposit, the second one represents the noise of the ECAL from electronics and pileup, and the third one is a constant for calibration errors. The design values of these constants lead to [29]:

$$\left(\frac{\sigma_E}{E}\right)^2 = \left(\frac{2.8\%}{\sqrt{E/\text{GeV}}}\right)^2 + \left(\frac{12\%}{E/\text{GeV}}\right)^2 + (0.3\%)^2. \tag{4.6}$$

Hadronic Calorimeter

The main task of the hadronic calorimeter (HCAL) [36] is the detection of hadronic jets. Therefore, it needs to reconstruct the energy deposit of each particle which was not measured in the ECAL. The only particles whose reconstruction do not depend on the energy deposit are muons (they are measured in the muon system and tracker). Neutrinos cannot be detected directly by the detector, but they can be reconstructed as Missing Transverse Energy (MET) if the source of MET is no particle arising from new physics.
The HCAL can be divided into two main parts, namely the inner and outer hadronic calorimeter. They are separated by the magnetic coil which is used as an additional absorber material. While the outer HCAL (HO) only consists of detectors in the barrel region, the inner HCAL has
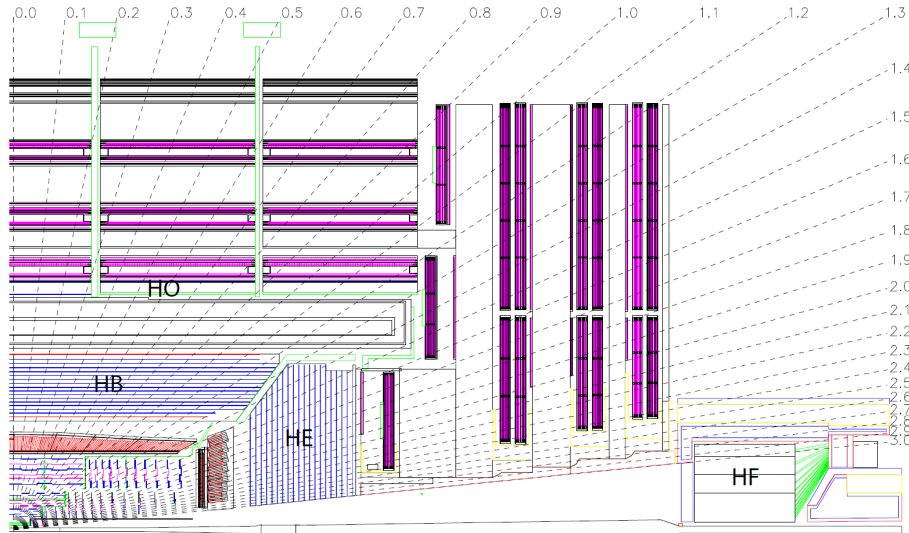
Figure 4.4.: Schematic overview of the CMS detector [29] showing the location of the hadron barrel (HB), endcap (HE), outer (HO), and forward (HF) calorimeter.

three parts: The hadronic barrel (HB), endcap (HE) and forward (HF) calorimeter (Fig. 4.4). The HCAL consists of alternating layers with plastic scintillators for energy measurement and material with a high density (mostly brass and steel) for absorption. The absorber depth of the HCAL corresponds to a minimum of 5.8 radiation lengths. For showers that are not completely stopped in the inner part of the HCAL, the hadronic outer calorimeter is used.

The resolution of the hadronic calorimeter is much worse than the resolution of the ECAL, it is given by [36]

$$\left(\frac{\sigma}{E}\right)^2 = \left(\frac{100\%}{\sqrt{E/\text{GeV}}}\right)^2 + (4.5\%)\,. \tag{4.7}$$

4.2.4. Solenoid Magnet

The momentum of particles and their charge is measured by their curvature in the tracker. To guarantee a good resolution also for particles with a high momentum, one needs a magnetic field of a high strength. The magnet of the CMS experiment is realized as a superconducting solenoid [29], resulting in a field strength of 3.8 T[2]. It covers the tracker, the ECAL and parts of the HCAL and is returned outside by an iron yoke. The cooling system uses liquid helium with a temperature of 4.65 K. Since the magnetic field is parallel to the beam axis, the transverse momentum can be measured due to the bending of a particle with

$$\frac{p_T}{\text{GeV}} \approx 0.3 \cdot \frac{B}{\text{T}} \frac{r}{\text{m}} \tag{4.8}$$

where B is the magnetic field strength and r the radius of the bending.

---

[2]It was designed for a strength up to 4 T

4.2.5. Muon System

One of the essential parts and the outermost component of the CMS detector is the muon system [37, 38]. Many interesting signatures in particle physics result in final states with muons, for example the decay of the Higgs boson via $H \rightarrow ZZ^* \rightarrow 4\mu$, but also this analysis depends on an accurate measurement of the muon momentum and charge up to high energies. Since muons are relatively long living and minimum ionizing particles, they can leave the detector and can be detected in the muon system. Due to the small interaction with the ECAL and HCAL material, their energy cannot be measured. The way how the muon system works is similar to the tracker: A charged particle, here a muon, travels through the muon system and produces hits in the different layers. To guarantee an optimal momentum resolution, the hits from the muon system and the silicon tracker can be combined (see Chap. 5). This gives the possibility to reach a resolution in the order of 5 % for high energetic muons of 1 TeV.

Fig. 4.5 presents a schematic overview of the CMS muon system. It can be seen that it is built out of three different kinds of gaseous detectors - namely the drift tubes (DT), cathode strip chambers (CSC), and resistive plate chambers (RPC) - that will be described below. The three detectors together cover a range of $|\eta| < 2.4$.
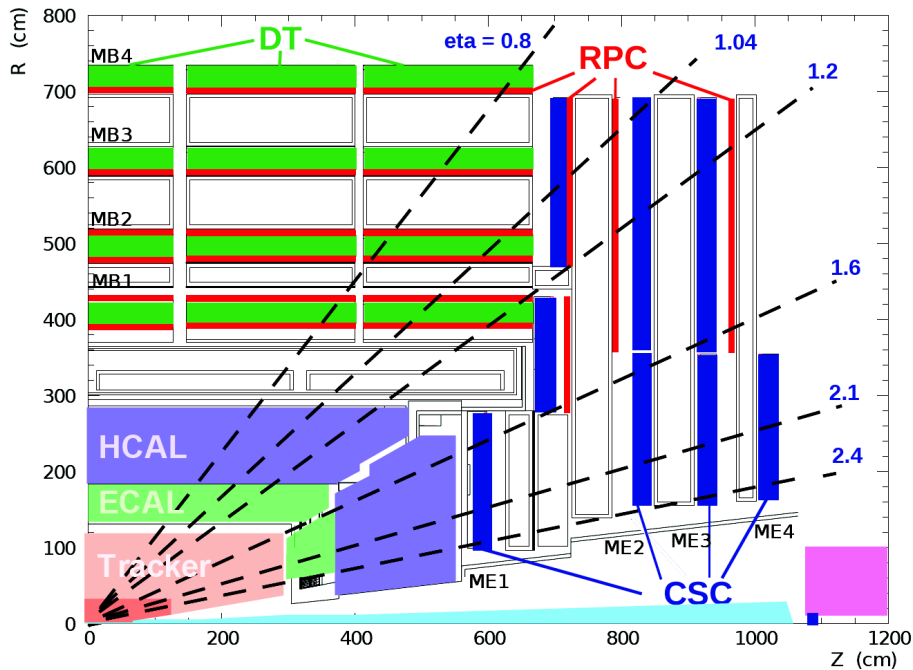
Figure 4.5.: Schematic overview of the CMS muon system [29].

Drift Tubes

In the barrel region of the detector ($|\eta| < 1.2$), a system built out of drift tubes (DT) is used since the magnetic field is nearly homogeneous and the muon rate is expected to be small here. The DTs are arranged in four concentric cylinders (muon stations) around the beam pipe - one between the hadronic calorimeter and the iron yoke (MB1), two inside the iron yoke (MB2 + MB3) and one outside the yoke which is the outermost part of the detector (MB4). Except for MB4 which has 70 drift tube chambers, all muon stations consist of 60 chambers, summing up to a number of 250 drift chambers in total. Each of them is built out of superlayers which

Figure 4.6.: Schematic overview of a drift cell, taken from [29].

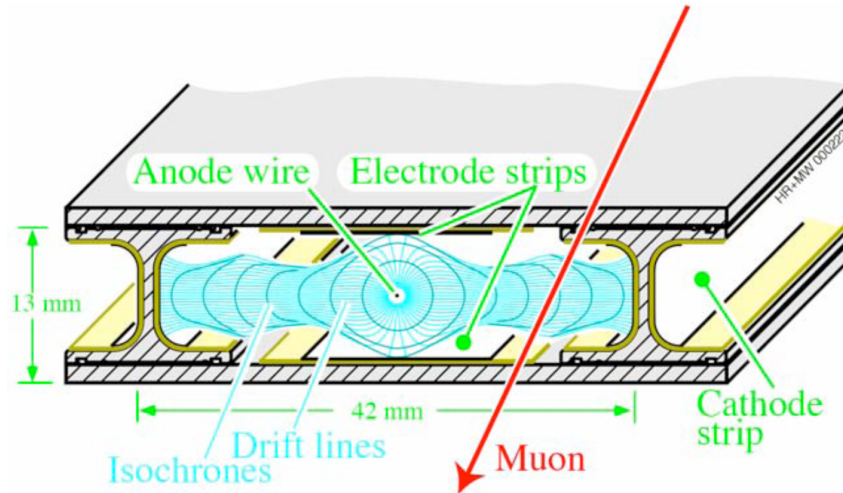themselves are formed from four layers of drift cells. The drift cells contain 50 μm anode wires with a voltage of +3600 V, two cathodes with -1200 V, and two electrodes with a voltage of +1800 V (Fig. 4.6). They are filled with 85 % Argon and 15 % CO2. If a charged particle passes the DT, it ionises the gas in the cells. The produced ions and electrons travel to the cathode and anode and cause an electric pulse that can be measured.

While the fourth muon station contains only two superlayers, the other stations have three. In case of the three first stations, the two outer ones are used for the measurement of the $r - \phi$ component and the inner one is used for the measurement in z-direction. In comparison to this, both layers of MB4 do only measure the $r - \phi$ component, meaning that no z-measurement is performed here.

Cathode Strip Chambers

In the endcap region of the detector, cathode strip chambers (CSC) are used, covering a range from $0.9 < |\eta| < 2.4$ which means that there is an overlap region with the DTs for $0.9 < |\eta| < 1.2$. In the endcaps, the magnetic field is inhomogeneous and the expected muon rate higher than in the barrel region. Therefore, CSCs are used since they have a shorter response time and perform better in an inhomogeneous magnetic field. The CSCs are shaped trapezoidal and consist of seven panels with cathode strips installed radially for a precise measurement in ϕ direction (Fig. 4.7). In the gas filled gaps between the panels, six planes of anode wires are orientated perpendicular, allowing the CSCs to measure the radial component of the muon momentum. Each endcap contains four CSC stations that are installed perpendicularly to the beam pipe and separated by the iron yoke. The working principle is similar to the one of DTs: A passing charged particle causes an ionisation of gas that leads to an electric pulse. The CSCs guarantee a spatial resolution between 75 μm next to the beam spot and 150 μm for CSCs which are further away due to more separated wires.

Resistive Plate Chamber

The third type of muon detectors are the resistive plate chambers (RPC). In comparison to DTs and CSCs, RPCs have a worse spatial resolution, but a much better response time of a few ns.
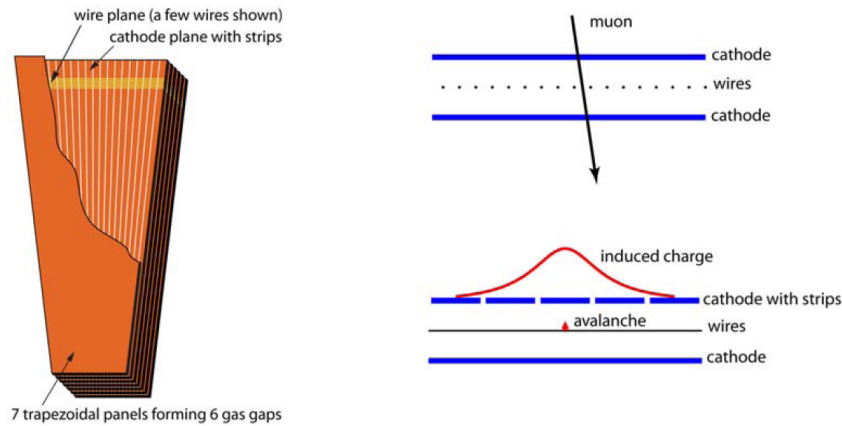
Figure 4.7.: Left: Schematic view of a cathode strip chamber (CSC) as it is used in the endcaps. Right: Working principle of CSCs [29].

Due to this short time resolution, RPCs can separate between different bunch crossings, meaning that a detected particle can be matched to its origin bunch crossing. Therefore, RPCs are mainly used as a trigger system. In the barrel region, six layers of RPCs are installed: Two at MB1 and MB2 and one at MB3 and MB4. This is done because of the fact that also low-p_T muons which do not travel through the whole muon system shall have a high number of hits in the RPCs. The endcaps consist of three layers of RPCs, covering a range of $|\eta| < 1.6$. They are built out of two gas filled chambers with a small gap of 2 mm where the read-out strips are located. RPCs are operating in avalanche mode: If a particle passes the RPC, ionises the gas. The detached electrons themselves ionise additional gas atoms producing an avalanche. This avalanche leads in the end to a strong signal that can be read out.

4.2.6. Data Acquisition, Trigger Setup and Computing

The LHC was designed for a bunch crossing time of 25 ns which corresponds to a collision rate of 40 MHz. Although the LHC did only operate with a bunch crossing time of 50 ns in 2012, a huge number of events was produced. These processes do also contain events that are not interesting for further studies. Since it is not possible to store every single event, a pre-selection has to be performed. Therefore, a trigger system has been developed for CMS which is based on two levels: The Level-1 trigger (L1) and the high level trigger (HLT).

The Level-1 Trigger

The first part of the CMS trigger system is the Level-1 trigger. It is located in the electronics of the different components of the calorimeters and the muon system, but not the silicon tracker. The L1 trigger uses only coarse information about the objects (for example muons and electrons). For this purpose, it selects characteristic information about them like the energy deposit in the calorimeter and hits in the muon system to form the trigger object. The information of all measured muon and calorimeter objects of the local triggers are then combined in the global muon and calorimeter trigger and afterwards in the global trigger which takes the final decision if an event passes the L1 trigger (Fig. 4.8). With help of the L1 trigger system, the output rate can be decreased to a few 100 kHz [39]. The Data Acquisition (DAQ) system collects the events that pass the L1 trigger and sends them to a computer farm where the HLT are processed.
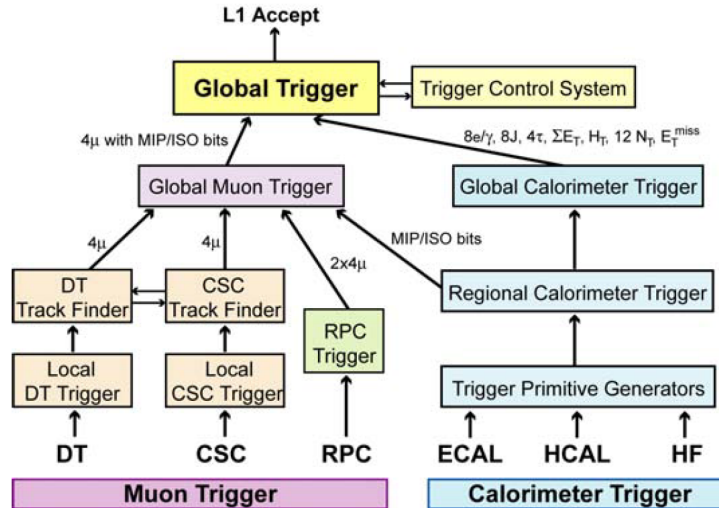
Figure 4.8.: Composition of the Level-1 trigger system, showing the combination of the local trigger to the global trigger [29].

The High Level Trigger

After an event passes the Level-1 trigger, it is send to a computer farm to be further processed in the high level trigger. In contrast to the L1 trigger, the HLT is software based and depends on the full data information. Therefore, its selection is more advanced. Depending on the analysis target, different HLT can be selected, for example muon, electron (photon) or jet triggers. The HLT starts with L1 trigger objects and improves their performance by adding additional information. In the case of muons, the L1 track is optimized by including for example tracker information to decide if the muon is a HLT object. The typical p_T threshold for single muon triggers is about 40 GeV and for double muon triggers between 8-22 GeV. The HLT_Mu17_Mu8 which is used in this analysis has trigger thresholds of 17 GeV and 8 GeV for the two muons. The combination of the L1 trigger and the HLT reduces the event rate to about 100 Hz.

The recorded data that pass the HLT are reconstructed and send to computing centers (Tiers) all over the world by the world wide LHC computing grid [40]. One copy of the recorded data is stored at the Tier-0 at CERN where it can be used for several reprocesses and (re-)reconstructions. The Tier-1 computing centers can also be used to reconstruct data events, but also the computation of Monte-Carlo simulation can be performed here. Tier-2 are used for the storage of a small amount of reconstructed data and Monte-Carlo simulation that is needed for analyses.

5. Muon Reconstruction

Compared to other processes, the decay to four leptons is very rare. Since the rate of events with four muons and an additional object such as electrons is even smaller, it is not necessary to apply a veto on events with other objects to increase the signal sensitivity. Therefore, only a brief documentation concerning the reconstruction of muons with the CMS detector will be given here based on [41, 42].

5.1. Tracking Algorithm

A muon passing the CMS detector causes hits in different subdetectors. These hits are used to reconstruct its trajectory within the detector. An accurate track reconstruction is essential for the measurement of the muon momentum and its charge, both can be computed from the bending of the track in the magnetic field. Three main effects have to be taken into account in the muon reconstruction procedure: The magnetic field is not homogeneous across the detector, muons with high momentum suffer from an energy loss due to photon radiation in the whole detector (especially in the iron yoke between the muon chambers), and the flight direction of muons is affected by multiple scattering. An algorithm based on four steps - trajectory seeding, building, cleaning and smoothing - converts the muon hits to track segments in the silicon tracker and the muon system [42]:

1. **Trajectory Seeding:** The starting point, also called seed, for the track reconstruction is defined in this step. It has to be compatible with the beam-spot as well as with the assumed physics process from the hard interaction. The two most common trajectory seeds in CMS are either "hit-based" seeds which require a pair or triplet of hits compatible with the beam spot or "state-based" seeds which are specified by an initial momentum and direction without requiring any hits.

2. **Trajectory Building:** The building of the trajectory starts at the trajectory seed which was defined in the first step. From this point, the algorithm proceeds in the direction specified by the seed to find compatible hits in the following detector layers. This is done by using a combinatorial Kalman filter [43] which depends on an iterative approach to update the trajectory estimate and its covariance matrix by incorporating material effects, for example energy loss due to radiation or multiple scattering. The final estimate of the trajectory is then weighted with the information from the measurement of the new layer combined with the measurements of the other layers. The propagation of a trajectory state to another position has to take into account the effects due to the inhomogeneous magnetic field and the detector materials.

3. **Trajectory Cleaning:** Within the trajectory building, a large number of trajectories is produced. Most trajectories share a large fraction of their hits which means that they are not unambiguous. Therefore, a cleaning step is applied which resolves these ambiguities and keeps a maximum number of track candidates.

4. **Trajectory Smoothing:** In the last step of the track building, a backward it is applied which allows to use all covariance matrices to all the intermediate points that have been

measured, meaning that the full gathered information is used to build the track.

5.2. Reconstruction Algorithms

There are different ways to reconstruct muons in CMS. All of them start with an independent reconstruction of the muon in the silicon tracker (tracker track) and in the muon system (standalone-muon track). In the next step, the two tracks are used to optimize the muon reconstruction [42].

Standalone Muon

The reconstruction of standalone muon tracks uses measurements and trajectory building in the muon system. Most of the standalone muons can later be associated with a tracker track, only a fraction of 1 % of all muons are standalone without and associated tracker or global muon. If the combination with a tracker track is successful, the muon can be classified as a global muon, as described below.

Tracker-only track

The tracker-only track reconstruction is similar to the standalone muon reconstruction, but based on silicon tracker hits. In contrast to standalone muons, tracker-only tracks cannot be identified as muons but rather have to be matched to segments in the muon spectrometer.

Global Muon

Global muons combine the information of the silicon tracker and the muon system to describe the muon with a higher accuracy. At low transverse momentum ($p_T < 200$ GeV), the inner tracker measurement provides the best momentum resolution since the reconstruction in the muon system suffers from multiple scattering while at high-p_T the momentum measurement can be improved by combining both sub-detectors. The global muon reconstruction follows an outside-in approach, starting with the standalone muon track and matching it to a subset of appropriate tracker tracks. For this purpose, a rectangular $\eta - \phi$ tracking region is defined which includes a number of possible tracker-only tracks. Only tracks that have a transverse momentum of at least 60 % of the standalone muon track are considered here. Afterwards, additional spatial and momentum criteria are applied to reduce the number of possibly matching tracker track for the combination with the standalone muon track. In a last step, a global fit is applied to all remaining pairs and the one with the lowest χ^2 is finally used as the reconstructed global muon. In comparison to the inside-out reconstruction (see tracker muon), this approach can improve the momentum resolution at high transverse momentum ($p_T > 200$ GeV).

Tracker Muon

While the global muon reconstruction follows an outside-in approach, the tracker muon reconstruction depends on an inside-out propagation which means that it starts with the tracker-only track and matches it to hits in the calorimeters and the muon system to obtain the tracker muon track. This approach is very useful for muons that cannot be reconstructed as standalone muons for some reasons which is the case for a large fraction of low p_T muons ($p_T < 6$-7 GeV) since they do not add enough hits in the muon spectrometer. Nevertheless, the tracker muon approach can still use the hits in the muon system for the reconstruction.

5.3. Muon Reconstruction at High-p_T

Because of the kinematics of the signal (Sec. 7.1), this analysis depends on an accurate reconstruction of high-p_T muons. The reconstruction of muons with high momentum suffers highly from energy loss by bremsstrahlung in the iron of the magnet return yoke and from additional hits produced by the resulting electromagnetic showers. Therefore, CMS has developed specialized algorithms for the measurement of TeV muons [41]:

- **Tracker-Plus-First-Muon-Station (TPFMS) fit:** Since the first muon station is located before the magnetic return yoke, the measurements in this station suffer less from Bremsstrahlung than the downstream stations. This is exploited in the TPFMS fit which starts with the list of hits used in the global track, but then only uses the hits from the first muon station.

- **The Picky Fit:** Just like the TPFMS fit, the Picky fit starts with the hits from the global track, but then requires the hits used from muon chambers with possible contributions from showers (high occupancy) to have a χ^2 below a certain threshold.
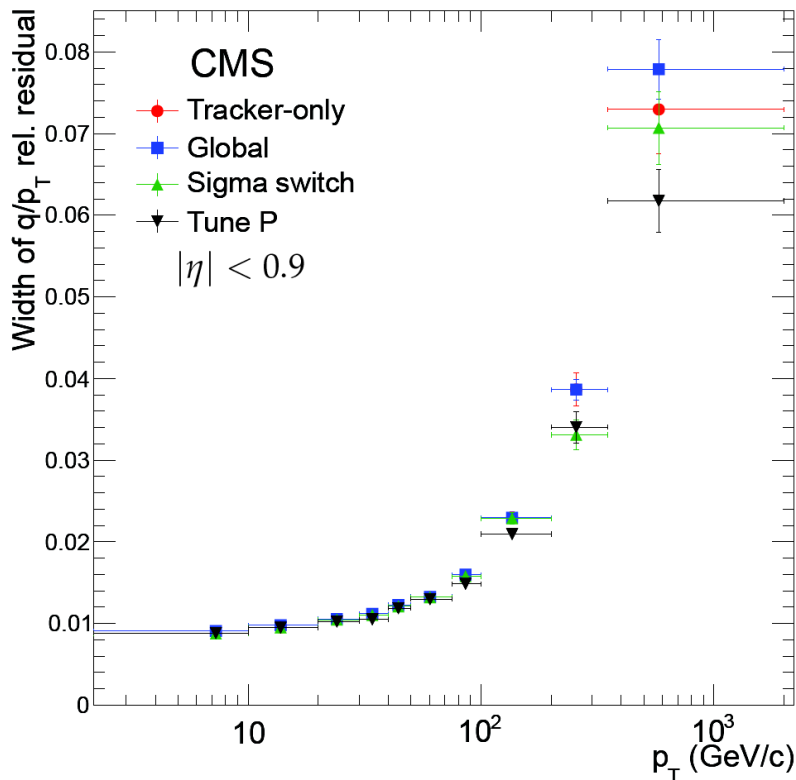
Figure 5.1.: Resolution as a function of the muon momentum for the tracker, global, and Tune-P reconstruction algorithm [41].

To improve the resolution of high-p_T muons (and to reduce the tails of the momentum resolution distribution), the so called "Cocktail" or "Tune-P" algorithm has been developed. Based on a muon-by-muon approach, the algorithm chooses between the tracker, global, TPFMS, and picky fits. At the beginning of the algorithm, it is checked if there is at least one muon with $\frac{\Delta p_T}{p_T} <$ 0.25. Here, Δp_T is the uncertainty of the transverse momentum that is extracted from the muon

fit. If no muon with $\frac{\Delta p_T}{p_T} < 0.25$ can be found, the threshold is raised by 0.15 until at least one muon can be selected. After a valid muon has been selected, it is tested if the p_T of the inner track is smaller than 200 GeV. If yes, it is used, if not, the algorithm proceeds with the picky fit if it is valid. In this case, it is compared to the inner track fit to decide which one is used. If there is no Picky fit, the TPFMS fit and afterwards the global track is chosen. In the end, the chosen muon track is compared to the TPFMS fit and the better one is selected [44, 45]. The effect of the Tune-P algorithm on the muon resolution at high transverse momentum can be seen in Fig. 5.1.

5.4. Identification of close-by Muon Pairs

Since this will be a serious issue of this analysis, a short summary of the identification of close-by muon pairs will be given here. A study about the identification of such muon pairs is documented in [41]. In this study, data from 2010 was used together with Monte-Carlo samples of low-mass resonances (J/ψ, ϕ and ρ/ω) to compare the efficiencies of medium muon selection (including tracker muon requirement) to the tight muon selection (including global muon requirement). The reason for the selection of low-mass resonances was the fact that they can have a very high boost which can lead to two close-by muons. The comparison of the two selection criteria in dependence of the angular separation $\Delta R = \sqrt{(\Delta\eta)^2 + (\Delta\phi)^2}$ showed an inefficiency in the tight muon selection for $\Delta R < 0.4$ that cannot be seen for the medium muon selection. This inefficiency is caused by a cleaning procedure used at the seeding stage of the global muon reconstruction to eliminate muon seeds leading to duplicates. The effect can be seen in data as well as in Monte-Carlo, meaning that it is well simulated.

To evaluate this effect for the Z-boson decay of the signal, a similar study was performed with $ee^* \to eeZ \to 2e2\mu$ signal samples. The kinematics of this process are similar to the signal of this analysis. Here, the muons are only required to be reconstructed as global or tracker muons. Results of this study are shown in Fig. 5.2. The left plot compares the efficiency where both muons are reconstructed as global muons (black points) with the one where only one muon is a global muon and the other one is a tracker muon (red points) as a function of ΔR. It can be seen that the reconstruction efficiency for the case that both muons are global muons decreases for $\Delta R < 0.4$ while the efficiency for a tracker and a global muon stays flat. The right plot shows the same effect in dependence of the transverse momentum of the Z-boson. The inefficiency starts for a Z-boson $p_T > 500$ GeV ($\gamma = E/m > 5.5$) and increases for higher transverse momenta.
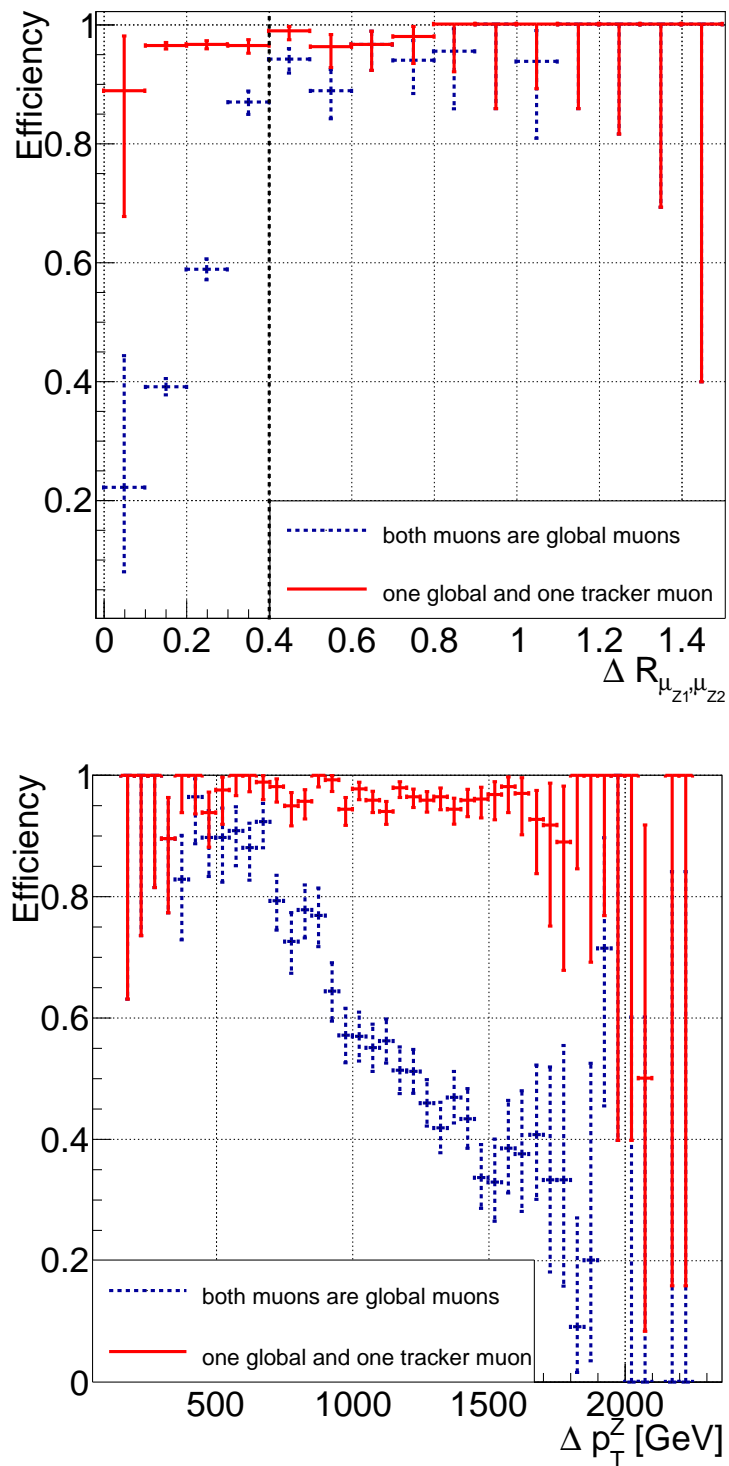
Figure 5.2.: Reconstruction efficiency of muon pairs in dependence of the angular separation ΔR of both muons (top) and the transverse momentum of the Z-boson (bottom).

6. Analysis Framework

In this chapter, the analysis framework will be described, starting with the reconstruction of the data followed by the explanation of the data and Monte-Carlo samples.

6.1. Data Reconstruction

The data handling and object reconstruction in CMS is based on the analysis software CMSSW (CMS Software) [46] which is provided by the CMS collaboration. In addition to data handling, CMSSW is also used for the simulation and reconstruction of background processes. Therefore, various generators are implemented in the framework, for example MADGRAPH [47], POWHEG [48], PYTHIA [49], and TAUOLA [50]. The simulation of the CMS detector is based on GEANT4 [51] which is also included as well as different tools for additional purposes like for example the calculation of the analysis luminosity or cross section limit computation. For this analysis, the version CMSSW_5_3_9 will be used.

The events recorded by the detector are contained in different data formats, depending on the included information: RAW, RECO and AOD. RAW stores the data taken by the detector, the trigger information and some information about the high-level trigger (HLT) objects. At this point, no reconstruction has been performed. The RECO data does include all the information of reconstructed high-level objects like leptons and jets, but also low-level information that are important for the reconstruction. The last data format is the AOD (Analysis Object Data) which has the smallest size of the mentioned three. It contains all the high-level objects that are needed for the analysis, but it has less information about the reconstruction, for example the information about the hits for the muon track reconstruction is removed. Most analyses depend on AOD data and therefore this data format is also used here.

Based on the ACSUSYANALYSIS [52] skimming software, minimum selection requirements are applied to the AOD data to reduce the file size before they are stored locally as flat ROOT [53] trees. The size of one event is now in the order of a few kB. The produced trees are later analysed with the ACSUSYANALYSIS framework to implement the final event selection.

6.2. Data and Simulation Samples

6.2.1. Data samples

For this analysis, the full CMS dataset collected in 2012 with proton-proton collisions at a center-of-mass energy of $\sqrt{s} = 8$ TeV is used. Tab. 6.1 shows the corresponding list of datasets, run ranges, and integrated luminosities. The luminosities of all runs sum up to $\mathscr{L}_{int} = (19.7 \pm 0.5)\,\mathrm{fb}^{-1}$ [54, 55].

All data events are triggered with two muons by the HLT_Mu17_Mu8 high-level-trigger. This means that the event contains at least two muons with a transverse momentum of 17 GeV and 8 GeV or higher. The information of the run-quality is saved in so called JSON files. There are different kinds of JSON files depending on the working detector components, for example the "muon" JSON and the "golden" JSON file. To be qualified as a good muon event, it is sufficient

CMS Run Range	Dataset Name	$\mathscr{L}_{int}$ (fb^{-1})
190456 - 193621	/DoubleMu/Run2012A-22Jan2013-v1/AOD	0.876
193833 - 196531	/DoubleMuParked/Run2012B-22Jan2013-v1/AOD	4.412
198022 - 203742	/DoubleMuParked/Run2012C-22Jan2013-v1/AOD	7.055
203777 - 208686	/DoubleMuParked/Run2012D-22Jan2013-v1/AOD	7.369
190456 - 208686	/DoubleMu*/Run2012-22Jan2013	17.712

Table 6.1.: List of datasets used in this analysis with the corresponding run ranges and integrated luminosities.

that the muon system is working well. If this is the case, the event is saved in the muon JSON file. The golden JSON file does only involve events where all components of the detector are in a good shape. Because of that, the muon JSON has about 1 fb^{-1} more data. Since this analysis uses Particle Flow isolation for the muons (Sec. 7.2.2) which also depends on the calorimeter information, the golden JSON file

Cert_190456-196531_8TeV_22Jan2013ReReco_Collisions12_JSON.txt

is used [56]. As the dataset names show, the re-reconstruction (ReReco) of all runs is used. Re-reconstructions are done to optimize the calibration and alignment of the data.

6.3. Parton Distribution Function and Cross Sections

In order to make a reliable prediction of the event rate of a background process or the signal, it is important to know its cross section with a high accuracy. Therefore, the production process has to be understood well. Since the LHC is a hadron collider based on proton-proton collisions, the compositeness structure of the protons has to be taken into account [3]. This substructure consists of quarks (valence and sea quarks) and gluons, also called partons, which all have a variable stake to the full proton momentum, meaning that the center-of-mass energy of two partons $\sqrt{\hat{s}}$ differs from the center-of-mass energy $\sqrt{s}$ of the two colliding protons. If x_1 and x_2 ($x_{1/2} < 1$) are the fractions of the parton momenta with respect to the proton momenta, the center-of-mass energy of the two interacting partons is given by

$$\sqrt{\hat{s}} = \sqrt{x_1 \cdot x_2}\sqrt{s}. \tag{6.1}$$

Although the exact momentum of the two partons is unknown, they can be described by parton distribution functions (PDFs) which are statistical distributions of the parton momenta at proton-proton colliders. The PDFs have to be determined experimentally and have been extrapolated to the LHC energies from measurements of previous experiments. Each parton has its own function that describes the probability of this parton to have the fraction x_i of the proton momentum depending on the energy scale Q^2. There is more than one method to derive PDFs from the measurements of cross sections, leading to a number of different sets that can be selected. Fig. 6.1 presents the PDFs obtained with the method MSTW2008 for $Q^2 = 10$ GeV^2 and $Q^2 = 10^4$ GeV^2 in dependence of the parton fraction x with respect to the proton momentum.

The predicted cross section of a process at hadron colliders depends on the used PDF set, meaning that it can differ if another one is used. It can be calculated by summing up all partons and integrating over the momentum fraction x_i of the partons:
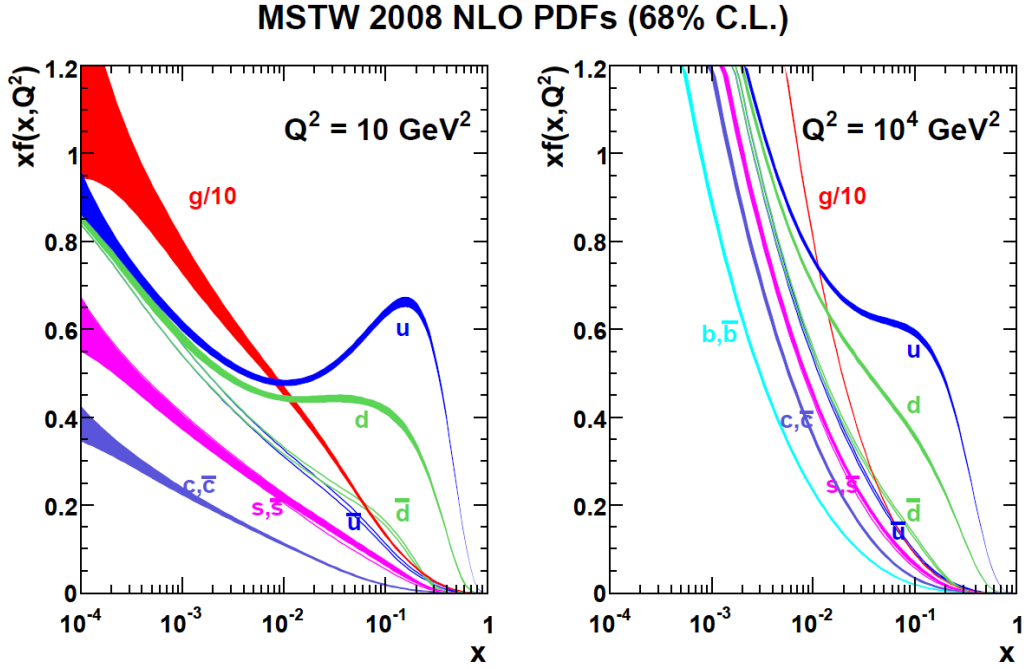
MSTW 2008 NLO PDFs (68% C.L.)

Figure 6.1.: Next-to-leading order PDF sets MSTW2008 for a energy scale $Q^2 = 10$ GeV^2 (left) and $Q^2 = 10^4$ GeV^2 (right) [57].

$$\sigma = \sum_{i,j} \int_0^1 \int_0^1 dx_1 dx_2 f_i \left(x_1, Q^2\right) f_j \left(x_2, Q^2\right) \hat{\sigma_{i,j}}(\hat{s}). \tag{6.2}$$

Here, $\hat{\sigma}_{i,j}(\hat{s})$ is the cross section of the parton-parton collision, $x_{1/2}$ the momentum fraction of the two partons with respect to the proton momenta, and $f_{i/j}$ the parton distribution functions. The theoretically calculated cross section can also be a higher order cross section (NLO[1] or NNLO[2]) that takes loop corrections in the production process into account. Therefore, it can be used to give a more accurate prediction of the background. Some generators (for example POWHEG [48]) do already produce NLO processes, but other generators (MADGRAPH [47], PYTHIA [49]) do only calculate leading order (LO) cross sections. In these processes, a scale factor

$$k = \frac{\sigma_{(N)NLO}}{\sigma_{LO}} \tag{6.3}$$

can be applied to extrapolate them to higher orders.

6.3.1. Standard Model Background Samples

To determine the expected background in this analysis, various Standard Model background processes were simulated, including the full simulation of the CMS detector based on GEANT4 [51]. The Standard Model background samples applied here are produced centrally with the Summer12 MC production scenario [58]. Afterwards, these background samples run through the

---

[1] next-to-leading order
[2] next-to-next-to-leading order

same analysis chain as the data, including the trigger and other selections. To get the number of expected background events, the different processes are scaled to the correct luminosity, using the event weight

$$w = a \cdot \frac{\mathscr{L}_{int}^{data} \cdot \sigma}{N_{bkg}} = a \cdot \frac{\mathscr{L}_{int}^{data}}{\mathscr{L}_{int}^{bkg}}. \tag{6.4}$$

In this case, N stands for the number of generated background events, σ for the cross section of the process, $\mathscr{L}_{int}^{data}$ for the integrated luminosity of the data (for data $\mathscr{L}_{int}^{data} = 19.7$ fb^{-1}), $\mathscr{L}_{int}^{bkg}$ for the luminosity of the background process, and "a" for an additional factor to include effects from pileup re-weighting or muon scale factors (see Sec. 7.3).

Standard Model Background	Generator	$\sigma_{(N)NLO}$ (pb)	# events	$\mathscr{L}_{int}^{bkg}$ (fb^{-1})	weight
$q\bar{q} \rightarrow ZZ \rightarrow 4\mu$	Powheg	0.07691(a)	$1.5 \cdot 10^6$	19 503	0.001
$q\bar{q} \rightarrow ZZ \rightarrow 4\tau$	Powheg	0.07691(a)	$7.5 \cdot 10^5$	9 752	0.002
$q\bar{q} \rightarrow ZZ \rightarrow 2\mu2\tau$	Powheg	0.1767(a)	$7.5 \cdot 10^5$	4 244	0.005
$gg \rightarrow ZZ \rightarrow 4l$	GG2ZZ	0.0048(a)	$5 \cdot 10^5$	104 167	0.0002
$gg \rightarrow ZZ \rightarrow 2l2l'$	GG2ZZ	0.01203(a)	$5 \cdot 10^5$	41 563	0.0005
$(Z \rightarrow ll) + $ jets	MadGraph	3503.7(b)	$30.5 \cdot 10^6$	8.71	2.26
$WZ \rightarrow 3l\nu$	MadGraph	1.057(a)	$2 \cdot 10^6$	1 892	0.01
$t\bar{t}$	Powheg	245.8(b)	$21.6 \cdot 10^6$	87.9	0.22
$t\bar{t}Z$	MadGraph	0.208(a)	$2 \cdot 10^5$	962	0.020
$t\bar{t}W$	MadGraph	0.232(a)	$2 \cdot 10^5$	862	0.023
$t\bar{t}WW$	MadGraph	0.002(a)	$2 \cdot 10^5$	100 000	0.0002
WWZ	MadGraph	0.0579(a)	$2 \cdot 10^5$	3 454	0.006
WZZ	MadGraph	0.0197(a)	$2 \cdot 10^5$	10 152	0.002
ZZZ	MadGraph	0.0055(a)	$2 \cdot 10^5$	36 364	0.0005
$gg \rightarrow H \rightarrow ZZ \rightarrow 4l$	Powheg	0.0051(b)	$1 \cdot 10^6$	195 620	0.0001
$VBF \rightarrow qqH$ $(H \rightarrow ZZ \rightarrow 4l)$	Powheg	$4.2 \cdot 10^{-4}$(a)	$5 \cdot 10^4$	118 902	0.0002
$qq \rightarrow t\bar{t}H$ $(H \rightarrow ZZ \rightarrow 4l)$	Pythia	$3.4 \cdot 10^{-5}$(a)	$1 \cdot 10^5$	2 918 270	$6.8 \cdot 10^{-6}$
$qq \rightarrow WH$ $(H \rightarrow ZZ \rightarrow 4l)$	Pythia	$1.9 \cdot 10^{-4}$(a)	$2 \cdot 10^6$	1 055 699	$1.9 \cdot 10^{-5}$
$qq \rightarrow ZH$ $(H \rightarrow ZZ \rightarrow 4l)$	Pythia	$1.1 \cdot 10^{-4}$(a)	$2 \cdot 10^6$	1 874 744	$1.1 \cdot 10^{-5}$

Table 6.2.: Standard Model background samples, cross sections σ ((a) NLO, (b) NNLO), number of generated events and corresponding integrated luminosity.

The theory investigated in this analysis results in a four muon final state. Therefore, it is important to include all processes which can produce four leptons. The main source of background is the Standard Model double Z-boson production, but also $t\bar{t}Z$ and triple boson production have to be taken into account. Tab. 6.2 presents the backgrounds for this analysis. The listed cross sections are given either for the next-to-leading order (NLO) or the next-to-next-to-leading order (NNLO) accuracy [59]. The way how these background processes can lead to a four lepton final state is summarized below:

- **$q\bar{q} \rightarrow ZZ \rightarrow 4l$:** This is the dominant background for analyses with a four muon final state. Here, more than 90% of the background expectation in the control region as well as in the signal region comes from dibosons decaying to four muons. This can also happen if the Z-bosons decay to τ-leptons and they subsequently decay to muons and neutrinos. For

this background, the officially produced POWHEG [48] samples which have a larger statistics than the official MADGRAPH [47] sample are used. The generator POWHEG simulates the background process directly at NLO. Fig. 6.2 shows the corresponding feynman diagrams for this background.
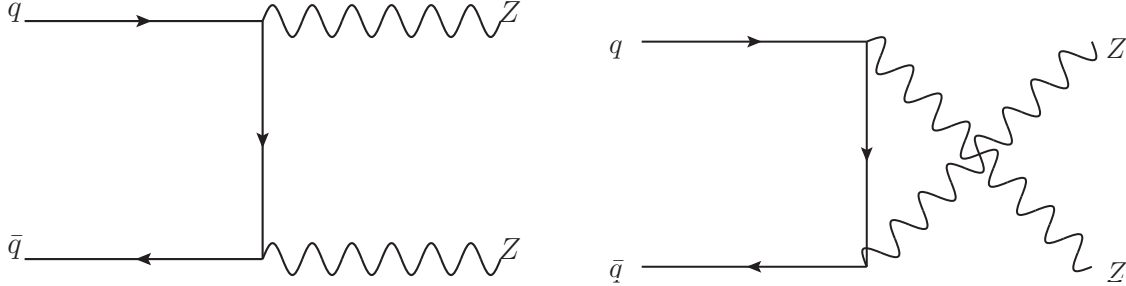

Figure 6.2.: Feynman diagrams of the main background $q\bar{q} \to ZZ$.

- **$gg \to ZZ \to 4l$:** In addition to ZZ production from $q\bar{q}$ annihilation, there is also the chance to produce two Z-bosons via gluon fusion (Fig. 6.3). For this background, NLO samples produced with the generator GG2ZZ [60] are used.
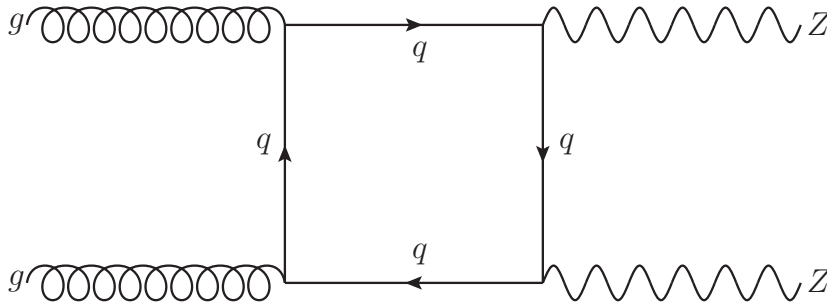

Figure 6.3.: Feynman diagrams of ZZ production via gluon fusion $gg \to ZZ \to 4l$.

- **$Z \to ll +$ jets:** There is a small probability that Drell-Yan processes with additional jets can result in four muons. For this process, a MADGRAPH sample with NNLO predictions has been used. Since no event passes the selection of this analysis, the Drell-Yan background will be neglected hereafter.

- **$WZ \to 3l\nu$:** This process can also lead to a four muon final state, but there is no contribution from it in this analysis based on the investigation of the MADGRAPH sample. The signal of the fourth muon can arise for example from additional jets.

- **$t\bar{t} \to 2l2\nu2q$:** A possible contribution can arise from $t\bar{t}$ events with two isolated muons and two muons from b-jets. To investigate this process, the POWHEG sample with NNLO prediction was used. Since there was no contribution due to the strict acceptance cuts, this background process will be neglected hereafter.

- **$t\bar{t}V \to 2l2\nu2qV$ $(V = W, Z)$:** The second most dominant background is the production of $t\bar{t}V$ $(V = W, Z)$. Both processes can result in a four muon final state by decaying the

same way as $t\bar{t}$ events, but with a higher probability if the additional boson decays to muon. The samples used have been generated with MADGRAPH using NLO predictions. Since only the $t\bar{t}Z$ production (Fig. 6.4) led to a contribution in this analysis, $t\bar{t}W$ will be neglected.

- **$t\bar{t}WW$:** A very rare process with a small contribution to the background is the $t\bar{t}WW$ production. It has been investigated using a MADGRAPH sample with NLO predictions.

- **WZZ, WWZ and ZZZ:** Four muon final states can also be produced by rare backgrounds like triple-boson production. These processes have very small cross sections, less than 1% of the complete background expectation arise from them (Fig. 6.4). The samples have all been generated with MADGRAPH using NLO predictions.
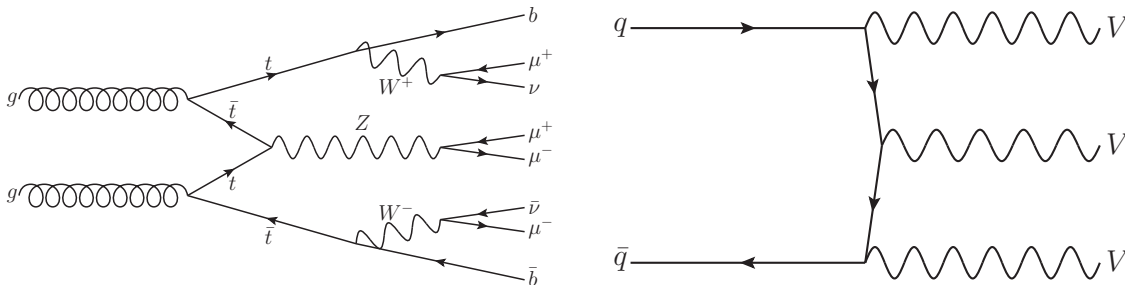

Figure 6.4.: Feynman diagram of $t\bar{t}Z$ production and multi-boson production.

- **$H \rightarrow ZZ^* \rightarrow 4l$:** The decay of the Standard Model Higgs boson[3] to two Z-bosons[4] and subsequently to four leptons can also result in a four muon final state [61]. The Higgs boson can be produced in different ways, the process with the highest cross section is the production via gluon fusion shown in Fig. 6.5. This process has been investigated by using a POWHEG sample with NNLO cross section [62]. In addition, the Higgs boson can also be produced by the processes vector boson fusion (VBF), radiation from a vector boson, and $t\bar{t}$-annihilation which have been included with NLO cross section. In case of VBF, the Higgs boson is produced with two additional jets. The investigated sample is simulated with POWHEG. The production via Higgs radiation and $t\bar{t}$ annihilation is estimated by using PYTHIA samples. In these cases, additional leptons can arise from the W, Z and $t\bar{t}$ decay and four lepton final states can also be realized if the Higgs decays to two W-bosons. Since there were no simulated samples for these three processes with the decay $H \rightarrow WW$, they are not included, but their contribution can expected to be in the same order of magnitude as from the decay with $H \rightarrow ZZ$. The cross section used here are taken from [62] From now on, the contribution of all Higgs samples will be summarized as $H \rightarrow ZZ^* \rightarrow 4l$.

These samples should describe the background expectation of this analysis with the needed accuracy.

6.3.2. Signal Samples

The signal samples for this analysis have been produced privately with PYTHIA8 [63] at leading order (LO) and at a compositeness scale of $\Lambda = 10$ GeV. Thirteen mass points between 200 GeV

---

[3]It is expected that the Higgs boson has a mass of 125 GeV
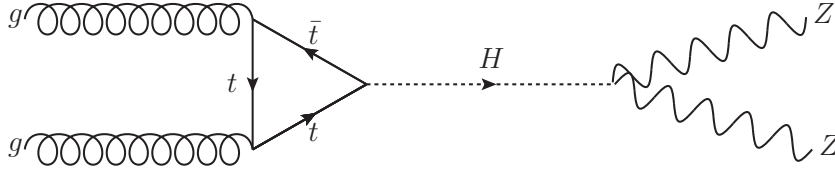[4]One of the Z-bosons is produced off-shell

Figure 6.5.: Feynman diagram of the Higgs boson production via gluon fusion with the subsequent decay $H \rightarrow ZZ^*$.

and 2600 GeV with a step size of 200 GeV and a number of 8 000 to 10 000 events have been simulated for the process $\mu\mu^* \rightarrow \mu\mu Z \rightarrow 2\mu 2l$ $(l = e, \mu, \tau)$. Since this analysis only includes the decay of the Z-boson to muons, the number of interesting events is about one third of the originally generated number. The feynman diagram of the investigated process is given in Fig. 6.6.
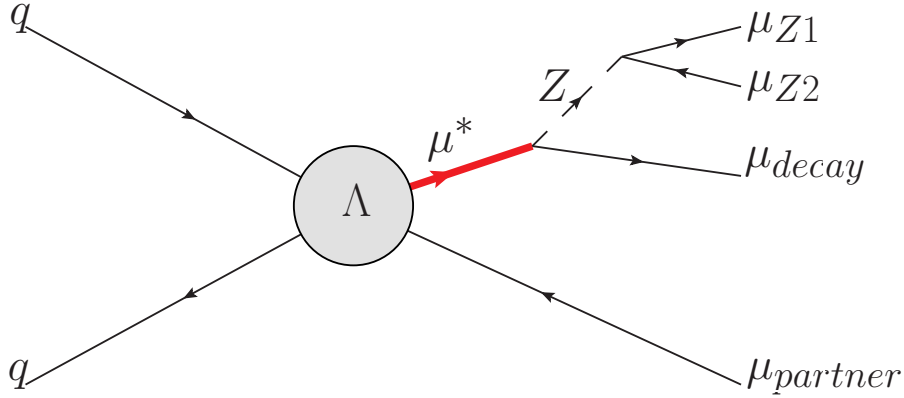

Figure 6.6.: Feynman diagram of the investigated signal. The excited muon is produced together with a Standard Model muon before decaying to three additional muons.

PYTHIA8 can only simulate the production via contact interaction and the decay via gauge interaction. This also means that the decay via contact interaction is not included in the cross section calculation. Since the theory described in Chap. 3 shall be investigated, the cross section has to be scaled to the correct value including the correct branching ratios. The calculation of the PYTHIA8 cross section is done via

$$\sigma^{Pythia\,8}_{\mu\mu^* \rightarrow \mu\mu Z \rightarrow 2\mu 2l} = \frac{\Gamma_Z \cdot \Gamma_{Z \rightarrow ll}}{\Gamma_Z + \Gamma_W + \Gamma_\gamma} \cdot \sigma^{Pythia\,8}_{\mu\mu^*} = \frac{\Gamma_Z \cdot \Gamma_{Z \rightarrow ll}}{\Gamma_G} \cdot \sigma^{Pythia\,8}_{\mu\mu^*} \tag{6.5}$$

where Γ_G is the decay width of all gauge interaction decays. The cross section we are interested in is given by

$$\sigma_{\mu\mu^* \rightarrow \mu\mu Z \rightarrow 2\mu 2l} = \frac{\Gamma_Z \cdot \Gamma_{Z \rightarrow ll}}{\Gamma_G + \Gamma_{CI}} \cdot \sigma_{\mu\mu^*} \tag{6.6}$$

with the contact interaction decay width Γ_{CI}. To get this cross section, the one given by PYTHIA 8 has to be scaled with the correction factor

$$c = \frac{\Gamma_G}{\Gamma_G + \Gamma_{CI}}. \tag{6.7}$$

This factor strongly depends on the ratio m_{μ^*}/Λ due to the fact that Γ_{CI} has a $m_{\mu^*}^5/\Lambda^4$ and Γ_G a $m_{\mu^*}^3/\Lambda^2$ dependence (Sec. 3.3). For $\Lambda = 10$ TeV and $m_{\mu^*} = 200$ GeV, the factor is $c = 0.993$ while for a mass of 2600 GeV, it is $c = 0.538$. The highest value is given at $m_{\mu^*} = \Lambda$ with $c = 0.08$. Once the cross section is corrected for a certain Λ value, it can be scaled to different Λ easily as long as one uses the correct branching ratios [64]. The decay via contact interaction can also result in a four lepton final state. It would increase the strength of the signal and therefore the sensitivity for the excited lepton search in this channel. Since there is no signal simulation for the contact interaction decay, it is not included here which means that the results will be conservative. A short discussion of the contribution of the CI decay is given in Sec. 8.5. Tab. 6.3 shows all produced working points with the corresponding leading order cross section, corrected cross section (also LO), NLO k-factor and number of generated events. The k-factor is based on [65] and was calculated for $\Lambda = 6$ TeV, although it does not depend on Λ. Fig. 6.7 shows the signal cross section for different Λ values and the mass dependence of the k-factor for $\sqrt{s} = (7, 8, 14)$ TeV.

M_{μ^*} (GeV)	cross section × BR without CI decay (pb)	cross section × BR incl. CI decay (pb)	k-factor	# events	# events 4μ
200	$2.095 \cdot 10^{-4}$	$2.081 \cdot 10^{-4}$	1.296	8 500	2 842
400	$1.363 \cdot 10^{-4}$	$1.334 \cdot 10^{-4}$	1.290	10 000	3 373
600	$8.122 \cdot 10^{-5}$	$7.757 \cdot 10^{-5}$	1.282	10 000	3 340
800	$4.817 \cdot 10^{-5}$	$4.449 \cdot 10^{-5}$	1.273	9 000	3 017
1000	$2.844 \cdot 10^{-5}$	$2.520 \cdot 10^{-5}$	1.268	10 000	3 341
1200	$1.675 \cdot 10^{-5}$	$1.414 \cdot 10^{-5}$	1.265	8 000	2 701
1400	$9.786 \cdot 10^{-6}$	$7.826 \cdot 10^{-6}$	1.267	9 000	3 021
1600	$5.686 \cdot 10^{-6}$	$4.286 \cdot 10^{-6}$	1.272	10 000	3 352
1800	$3.286 \cdot 10^{-6}$	$2.325 \cdot 10^{-6}$	1.282	10 000	3 303
2000	$1.875 \cdot 10^{-6}$	$1.242 \cdot 10^{-6}$	1.295	10 000	3 416
2200	$1.062 \cdot 10^{-6}$	$6.569 \cdot 10^{-7}$	1.311	10 000	3 292
2400	$5.936 \cdot 10^{-7}$	$3.424 \cdot 10^{-7}$	1.329	10 000	3 281
2600	$3.280 \cdot 10^{-7}$	$1.763 \cdot 10^{-7}$	1.348	10 000	3 264

Table 6.3.: Summary of Monte Carlo signal samples with corresponding cross sections × branching ratio ($\sigma \times BR$), k-factors, and numbers of generated events used for $\mu\mu^* \to \mu\mu Z \to 2\mu 2l$ ($l = e, \mu, \tau$) at $\Lambda = 10$ TeV.

For some studies concerning the decay of the Z-boson, $ee^* \to eeZ \to 2e2l$ ($l = e, \mu, \tau$) signal samples that are also produced with PYTHIA 8 [63] will be used for comparison reasons. The kinematics of the Z-boson from the e^* decay should be nearly the same as for the μ^*, but with the advantage that one has not to select the best Z-boson if it decays to leptons ($l \neq e$). The characteristics of the e^* signal samples are similar to the μ^*, the branching ratio is the same within the uncertainties for corresponding mass points and also the number of simulated events is comparable to the μ^* samples [66].
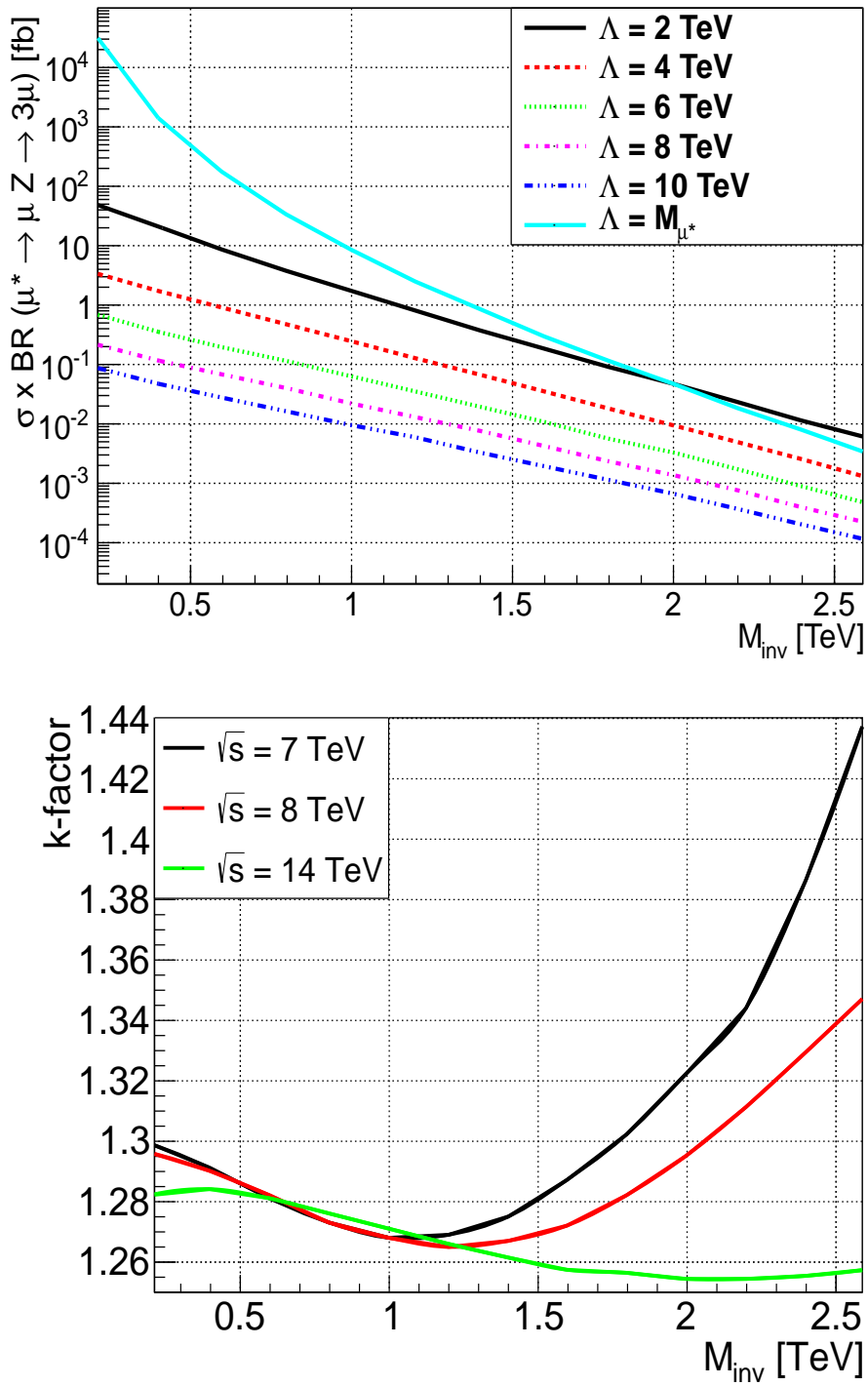
Figure 6.7.: Left: Signal cross section $\times$ branching ratio ($\sigma \times BR$) depending on the excited muon mass for different Λ values; right: Mass dependence of the k-factor for $\sqrt{s} = (7, 8, 14)$ TeV [65]

7. Analysis

In this chapter, the the analysis is described, by presenting the characteristics of the signal, the selection criteria, applied corrections and the determination of the systematic uncertainties.

7.1. Signal Properties

Before starting with the optimization of the event selection (Sec. 7.2), the behaviour of the signal has to be understood. Therefore, characteristic distributions on generator level are studied, showing the expected kinematics of the final states and their dependence on the μ^* mass. Later, this will help to distinguish signal from background events to discriminate the background without loosing much signal efficiency.

As said before, a search for in excited muons in the four muons final state will be performed. The excited muon decays to a Standard Model muon and a Z-boson which subsequently decays to two leptons leading to a three muon final state. Its mass can be directly reconstructed from the decay kinematics. Nevertheless, there is still a small problem: Each event contains four muons due to the additional muon from the production process, but only three of them are from the μ^* decay (Fig. 6.6). At the beginning, there are four possible muon combinations which could all be the correct one: $M_{inv}^{\mu 123}$, $M_{inv}^{\mu 124}$, $M_{inv}^{\mu 134}$ and $M_{inv}^{\mu 234}$. Even if the Z-boson can be reconstructed with a very high accuracy, there are two combinations left. Those two combinations can be divided into the minimum invariant mass M_{min} and the maximum invariant mass M_{max}, shown in Fig. 7.1(a) and Fig. 7.1(b) at generator level for different μ^*-masses. It can be seen that the mass peak from the excited muon is well reconstructed for low invariant masses if M_{min} is used and for high invariant masses if M_{max} is used. This leads to the problem that it is not really sure which of the two distributions is the better one for the optimization of the search window. A possible solution can be found by using the two-dimensional M_{min}-M_{max} invariant mass plane which is given in Fig. 7.1(c). This application leads to an "inverse letter L" which can be used for a combined cut on M_{min} and M_{max}. If the excited muon is reconstructed by using M_{min}, it leads to the vertical leg around the signal mass while a reconstruction via M_{max} gives the entries for the horizontal leg. After performing the full detector simulation, the "L" can be expected to have a much larger width because of the muon momentum resolution (see Sec. 8.2).

The next step is to study the mass dependence of the decay kinematics. The reconstructed invariant mass from the muons μ_{Z1} and μ_{Z2} as well as from $\mu_{partner}$ and μ_{decay} are shown in Fig. 7.2(a) and 7.2(b). Fig. 7.2(c) presents the transverse momentum from the Z-boson for different μ^*-masses. It can be seen that p_T^Z increases for higher μ^*-masses to very high values for $\mu^* = 2.6$ TeV. Important here is the fact that p_T^Z is often larger than 500 GeV for μ^*-masses beyond 1 TeV. This should lead to a low angle between the decay products (see Sec. 5.4). The effect is shown in Fig. 7.2(d) which demonstrates the $\Delta R = \sqrt{(\Delta\phi)^2 + (\Delta\eta)^2}$ distribution of the two muons from the Z decay for different μ^*-masses. As expected, the angle between the two muon decreases for higher masses, leading to a high number of events with $\Delta R < 0.4$. As discussed in Sec. 5.4, a small distance between two muons can lead to problems in the global muon reconstruction. The effect of this behaviour on the given signal will be investigated in more detail in Sec. 7.2.3.
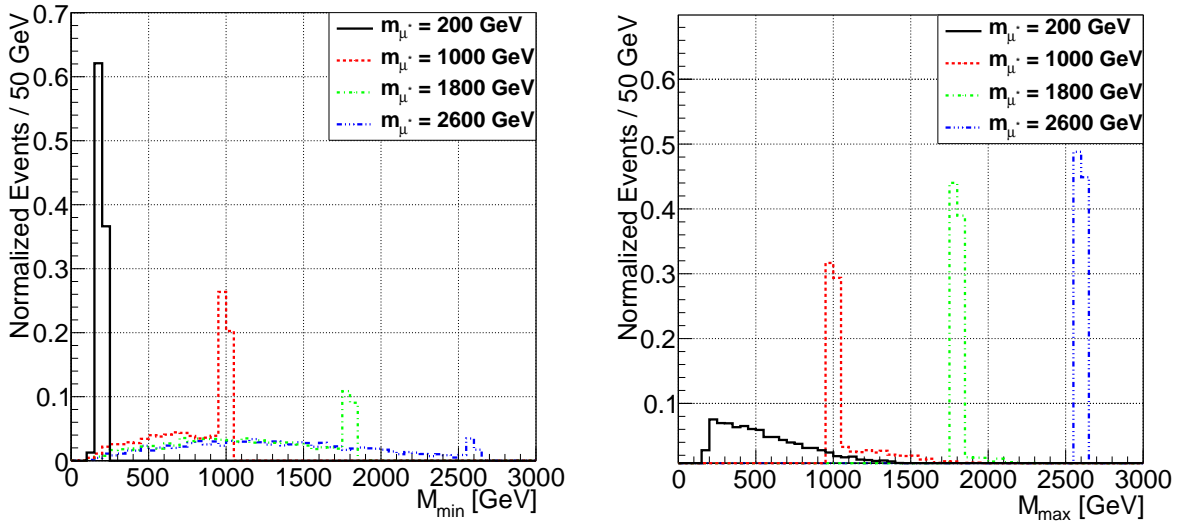
(a) Minimum invariant mass M_{min}

(b) Maximum invariant mass M_{max}
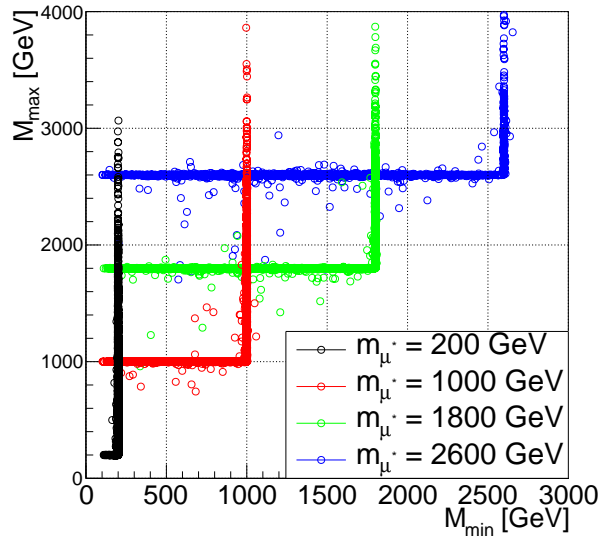
(c) Minimum-maximum invariant mass plane

Figure 7.1.: Invariant mass plots on generator level for different μ^*-masses: (a) Minimum invariant mass M_{min}; (b) Maximum invariant mass M_{max}; (c) 2-dimensional minimum-maximum invariant mass plane, also called "L-shape" diagram.

The last important step is to understand the properties of the final state objects. The final state is represented by four muons, one from the μ^*-production, one from the μ^*-decay, and two from the decay of the Z-boson (Fig. 6.6). Although the Z-boson momentum increases for higher masses, it can be expected that one of its muons has the lowest momentum of the four. Since the selection of the identification criteria as well as the acceptance cuts depend on the transverse momentum of the four muons it is important to have a look at the generated p_T of these four objects (see Fig. 7.3(a) - 7.3(d)). The two leading muons have a p_T of at least 35 GeV for every
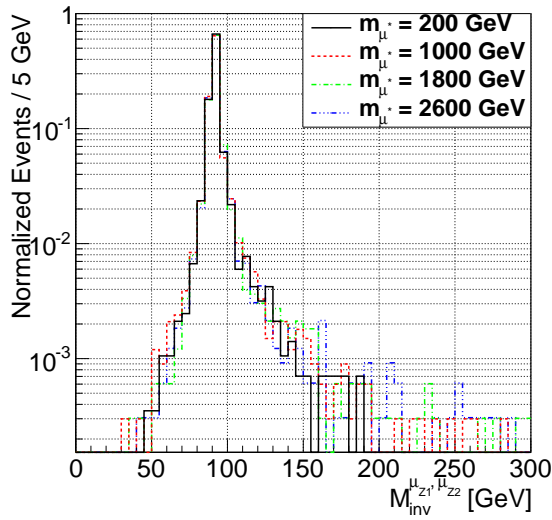
(a) Reconstructed Z-boson mass from the two muons μ_{Z1} and μ_{Z2}
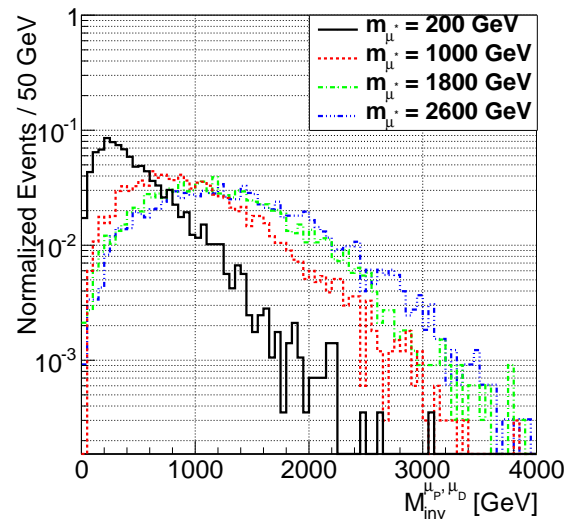
(b) Reconstructed mass from the two muons $\mu_{partner}$ and μ_{decay}
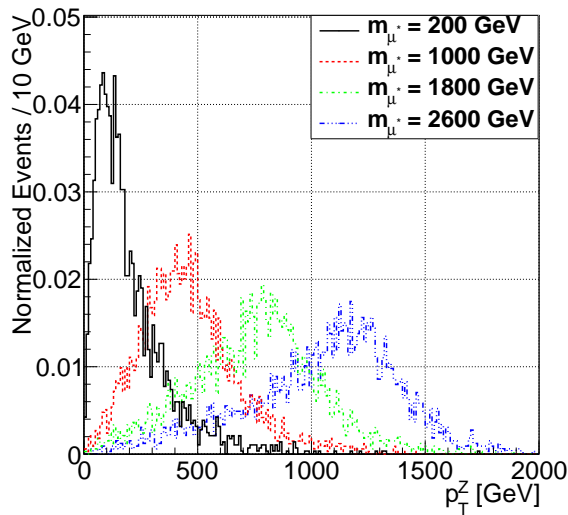
(c) p_T-distribution of the Z-boson
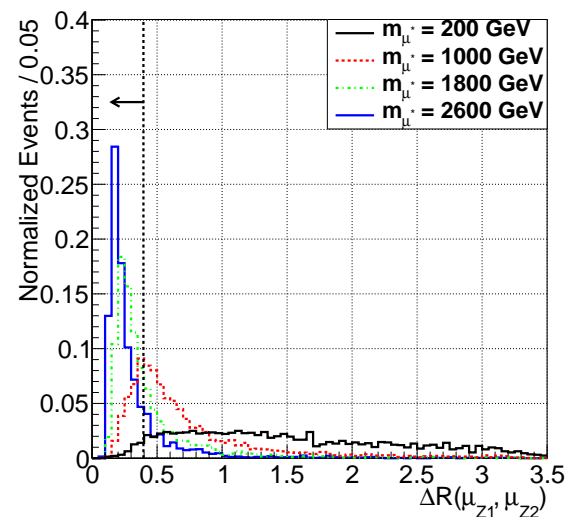
(d) ΔR between the two muons from the Z decay

Figure 7.2.: Kinematics of the Z-boson and its decay on generator level for different μ^*-masses.

mass point. In addition to this, it can be seen that even for low masses a large fraction of them have a $p_T > 200$ GeV. The two slowest muons have a much softer spectrum. While μ_3 still has a transverse momentum above 20 GeV, μ_4 often has a $p_T < 20$ GeV. Even for high μ^* masses, in some cases the p_T of the fourth muon is less than 20 GeV. Nevertheless, most events contain at least three muons with $p_T > 200$ GeV which will be used for an optimal signal selection (see Sec. 7.2).

(a) Leading muon $p_T^{\mu 1}$

(b) Second leading muon $p_T^{\mu 2}$

(c) Third muon $p_T^{\mu 3}$

(d) Lowest muon $p_T^{\mu 4}$
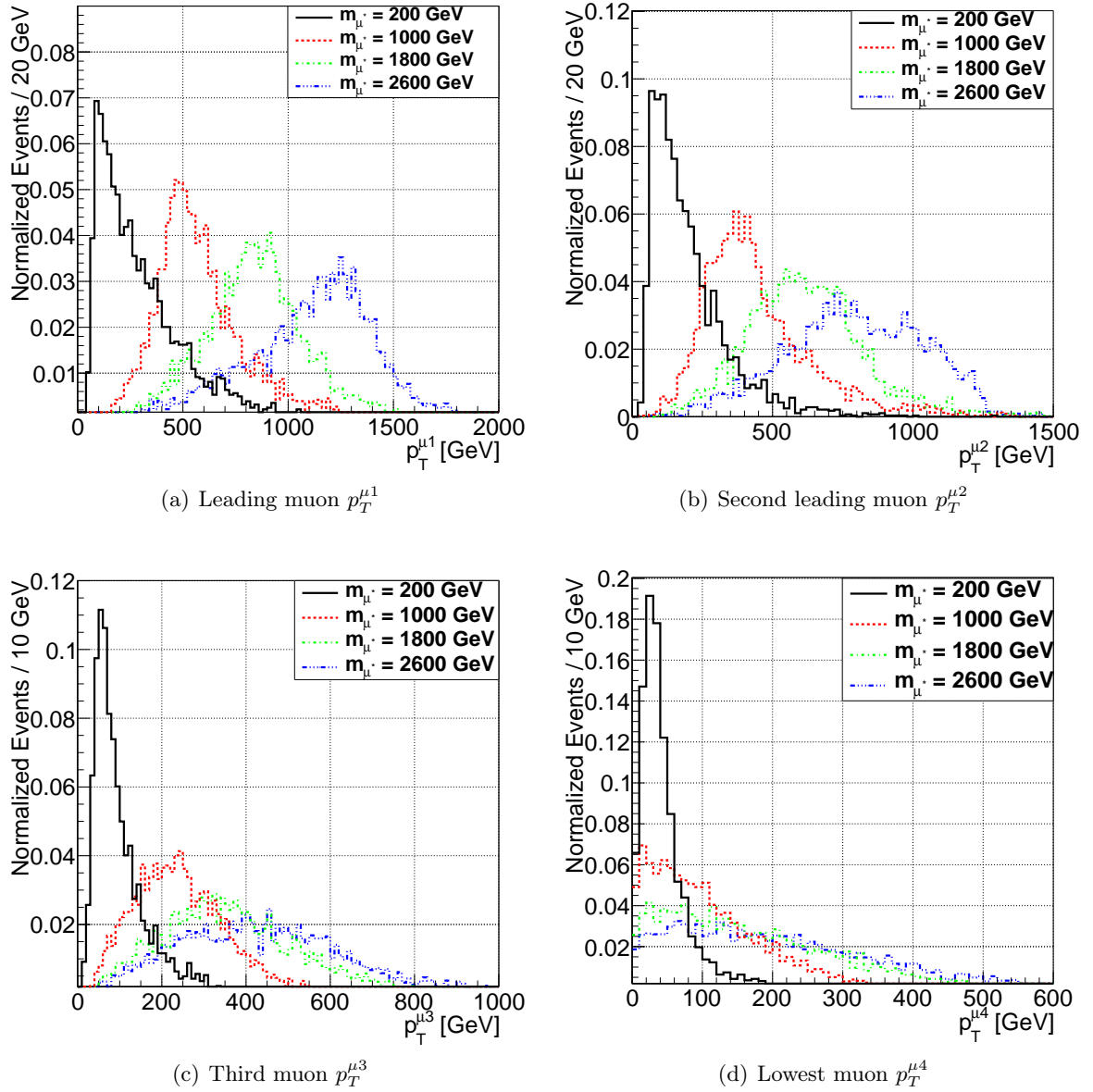
Figure 7.3.: Transverse momentum on generator level for the four muons in the final state.

7.2. Signal Optimization

After understanding the signal kinematics, its selection can be discussed. The main goal is to distinguish it from the background. Therefore, selection criteria have to be applied based on the signal and background behaviour. Luckily, this analysis suffers only from one main background process which makes the reduction of it much easier. If there is no excess in data after applying all the cuts, a exclusion limit will be set on the excited muon mass for this channel.

7.2.1. Trigger and Acceptance

The trigger used in this analysis is the HLT_Mu17_Mu8 trigger. The threshold of the two trigger legs are 17 GeV and 8 GeV within a pseudorapidity of $|\eta| < 2.4$. Because of the multi muon final state, this trigger should have a very high efficiency. The four muons from the signal lead to six possible muon pairs (two same sign and four opposite sign) which can be triggered. Normally, at least three leptons are above the trigger threshold for every masspoint of the signal as discussed in Sec. 7.1. Only the fourth lepton has sometimes a smaller transverse momentum. Therefore, the acceptance cuts are set to $|\eta| < 2.4$ and $p_T > 20$ GeV for all four muons. If one wants to use the single muon trigger with $p_T > 40$ GeV and $|\eta| < 2.1$, one could set the transverse momentum for the two leading muons to $p_T > 45$ GeV without loosing much signal efficiency. The summary of the trigger and acceptance cuts:

- Trigger: HLT_Mu17_Mu8

- Geometrical acceptance: $|\eta| < 2.4$
- Transverse momentum: $p_T > 20$ GeV

} for all four muons.

7.2.2. Muon Identification

After setting the trigger and the geometrical acceptance, the quality criteria for the muon identification (muon ID) have to be applied. Only well reconstructed muons should pass the quality criteria. There are different kinds of muon requirements based on the target of an analysis. Since the signal leads to muons with medium or high transverse momenta (Sec. 7.1), the high-p_T muon ID [67] recommended by the CMS Muon Physics Object Group (POG) [68] for muons with high transverse momentum (> 200 GeV) is used. The quality criteria for the high-p_T muon ID are:

- The muon has to be reconstructed as a **global muon**: A global-muon track (outside-in) has been fitted by combining the hits from the standalone-muon track and the tracker muon track. More details about muon reconstruction are given in Chap. 5.

- There has to be at least **one muon chamber with hits included in the global-muon track fit**. If this is not the case, the muon is most likely also not reconstructed as a global muon.

- At least **two muon stations must have muon segments**. This cut also implies that the muon has to be a **tracker muon**. It is applied to suppress the hadronic "punch-through" as well as muons from decays-in-flight. Hadronic "punch-throughs" are high energy hadrons that are not fully absorbed in the HCAL and generate hits in the muon system. Normally, these events do not reach the second muon station being absorbed by the iron yoke of the magnet before. Muons from decays-in-flight originate from the decay of, for example, kaons and pions [69].

- The **transverse impact parameter with respect to the primary vertex d_{xy} has to be less than 0.02 cm**. This selection is used to suppress cosmic muons and again muons from decays-in-fight. The standard recommendation for this cut is 0.2 cm, but since this cut is a very loose one, it can be tightened to 0.02 cm without loosing much efficiency.

- The **longitudinal distance with respect to the primary vertex d_z has to be less than 0.5 cm**. This selection suppresses cosmic muons and again muons from decays-in-flight. In addition, it can also suppress tracks from pileup [69].

- For a good p_T Requiring more than five tracker layers leads to a better p_T measurement and to a smaller uncertainty. Until 2012, the number of tracker layers with hits had to be more than 8, but it has been reduced and an additional cut on $\Delta p_T / p_T <$ has been applied to increase the selection efficiency.

- The ratio of the uncertainty on the p_T measurement with respect to the measured p_T has to be less than 30% ($\boldsymbol{\Delta p_T / p_T < 0.3}$). This cut was added to compensate the reduction of the number of tracker hits, leading to an increase of absolute the overall efficiency per muon by 5% without additional, badly reconstructed muons passing the selection.

- There has to be at **least one hit in the pixel detector** to suppress muons from decays-in-flight and to guarantee a good vertex reconstruction.

In addition to the muon identification criteria, it is required that the muons have to be isolated. There are different ways of applying isolation to muons, but the two most common ones are the tracker relative isolation (TRK-isolation) and the particle-flow isolation (PF-isolation). The TRK-isolation adds up any track in a cone of $\Delta R = \sqrt{(\Delta\phi)^2 + (\Delta\eta)^2} < 0.3$ with respect to the muon, except the track of the muon itself. Afterwards, the ratio between the sum-p_T of those tracks and the muon track p_T is used as the discriminator variable for the isolation. In contrast to TRK-isolation, particle-flow isolation uses the sum-p_T of all charged hadrons and the transverse energy of all photons and neutral hadrons within a cone of $\Delta R < 0.4$. The discriminator variable is then the ratio of this number and the muon track p_T. In comparison to TRK-isolation, PF-isolation mostly has a better performance and can also include pileup corrections [41]. Therefore, PF-isolation with $\Delta\beta$-correction (pileup correction) is applied to the muons in this analysis with a loose cut of

$$\boldsymbol{I_{PF} = \left(\sum_{\text{ch. had.}} p_T + \max\left[0., \sum_{\text{n. had.}} E_T + \sum_{\gamma} E_T - c \cdot \sum_{\text{pileup}} p_T \right] \right) / p_T^{\mu} < 0.2} \qquad (7.1)$$

where the factor $c = 0.5$ corresponds to a naive average of neutral to charged particles [70]. Here, "ch. had." are the charged hadrons, "n. had." are the neutral hadrons, "γ" are the photons and "pileup" are the additional pileup tracks in $\Delta R < 0.4$. Fig. 7.4(a) shows the acceptance $\times$ efficiency at this point of the analysis while Fig. 7.4(b) exhibits the efficiency with respect to the acceptance. It can be seen that there is a drop in the efficiency for high invariant masses. This drop is caused by the decay of boosted Z-bosons to two nearby muons (Sec. 5.4). The influence of this feature and how to solve the caused problems will be discussed in Sec. 7.2.3.

7.2.3. Muon Identification for boosted $Z \to \mu\mu$

As seen in Fig. 7.4, the standard high-p_T muon ID shows a lower efficiency at high invariant masses due to the decay of the Z-boson to two muons. Because of the boost of the Z-boson for high μ^*-masses, the two muons are close to each other (Sec. 7.1). In Sec. 5.4 it was mentioned that in case of two nearby muons only one of them is reconstructed as a global muon while the other muon is treated like a duplicate and can only be reconstructed as a tracker muon. Here, a way to keep the signal efficiency flat will be shown based on [71].
For a better understanding of this behaviour, $ee^* \to eeZ \to 2e2\mu$ have been used. The kinematics of the decay products are nearly the same as for the μ^*, but its signal only consists of the two muons from the Z decay. This makes an examination of this problem easier and more accurate. Fig. 7.5(a) shows the single leg efficiency of each muon ID cut. The efficiency for reconstructing
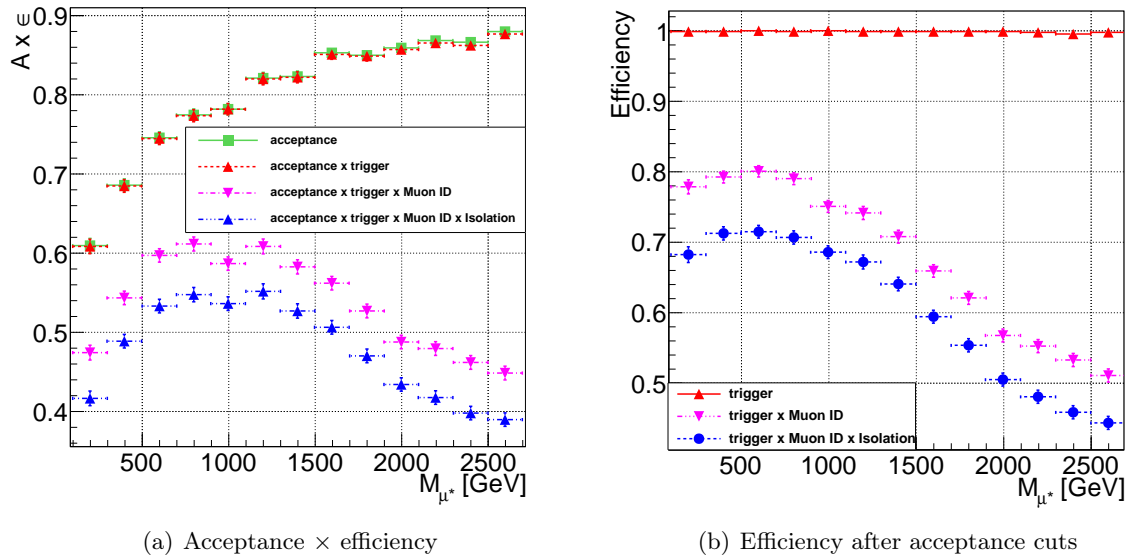
(a) Acceptance × efficiency

(b) Efficiency after acceptance cuts

Figure 7.4.: Acceptance × efficiency (A × ε) and efficiency with respect to the acceptance after applying the high-p_T muon ID and PF-isolation.

muons as global muons drops for higher μ^* masses. The same loss of efficiency can be seen for the number of valid muon hits and for the $\Delta p_T/p_T$ cut. The origin of this inefficiency is the same in all cases: One of the two muons is treated as a duplicate. Therefore, its number of muon hits in the global track is set to zero which is the reason for the inefficiency of this identification step. Consequently, this muon does not qualify as a global muon. As a solution for this inefficiency, the identification criteria will be changed. Instead of a global and a tracker muon, one of the two muons from the Z decay has to be reconstructed only as a tracker muon. For this muon, the cut on the number of muon hits in the global track will be removed. This change should help to regain the efficiency and is also used by other analyses [71–73].

The last problem can be seen for the $\Delta p_T/p_T$ cut. Here, the error on the track is divided by the transverse momentum of the cocktail algorithm, but the cocktail algorithm can only be used by muons which are global muons. This, again, results in the known inefficiency. Since the muons are reconstructed as tracker muons in the most cases, the tracker variables can be used for the $\Delta p_T/p_T$ cut.

Fig. 7.5(b) shows how the new muon ID performs before an isolation requirement. Here, different cases have been compared, using the $ee^* \rightarrow eeZ \rightarrow 2e2\mu$ signal for the muon pair from the Z decay (red points) and the $\mu\mu^* \rightarrow \mu\mu Z \rightarrow 2\mu 2e$ signal for the standard muon pair (black points). In both cases, the standard (triangles) and the modified (circles) identification criteria have been applied. It can be seen again that the standard ID leads to an increasing inefficiency for higher l^* masses in case of the muon pair from the Z decay, resulting in a drop by 50% for $M_{l^*} = 2600$ GeV while the efficiency for the two other muons stays flat. After applying the modified ID to both muon pairs, one can see that the efficiency stays flat in both cases. Since the modified ID has looser identification criteria, it has a slightly higher efficiency what can be seen by comparing the black circles and triangles.

After applying the correction of the identification criteria, we will also have a look at the isolation.
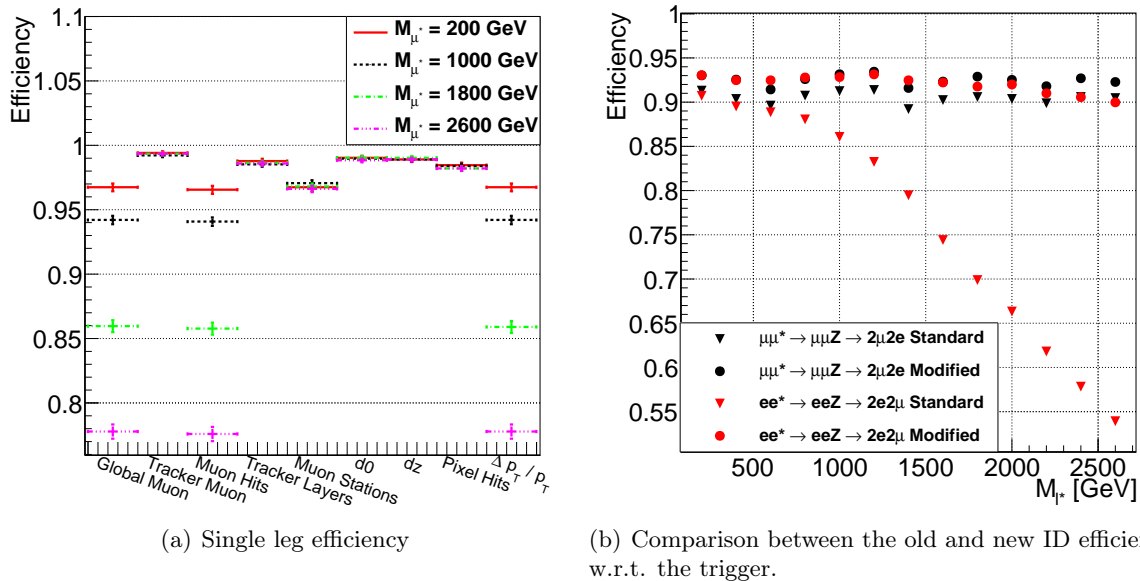
(a) Single leg efficiency

(b) Comparison between the old and new ID efficiency w.r.t. the trigger.

Figure 7.5.: (a) Single leg muon efficiency for each ID step at different μ^*-masses. (b) Comparison between old and modified identification criteria using $ee^* \to eeZ \to 2e2\mu$ and $\mu\mu^* \to \mu\mu Z \to 2\mu 2e$ signals.

As explained in Sec. 7.2.2, it is planned to use the Particle-Flow isolation for this analysis which is defined in a cone size of $\Delta R < 0.4$ where also the efficiency drop takes place. This can also lead to an inefficiency caused by the isolation requirement if both muons are close to each other. Therefore, the isolation efficiency will again be compared with respect to the modified muon ID by using $ee^* \to eeZ \to 2e2\mu$ events. Fig. 7.6(a) shows the single leg efficiency for PF-isolation for $M_{e^*} = 200$ GeV and $M_{e^*} = 2600$ GeV. The cut is set to $I_{PF} < 0.2$. The fraction of events with an isolation above 0.2 is much higher for the high mass samples (23%) compared to the low mass samples (5%). To regain these lost events, both muons from the Z decay have to pass a modified isolation based on tracker relative isolation. Tracker relative isolation sums up the tracker p_T of all muons in a cone of $\Delta R < 0.3$ and divides it by the muon tracker p_T. The modification takes place if two muons are within a cone of $\Delta R < 0.3$: At this point, the contribution of the other muon is removed from the isolation calculation leading to the requirement

$$\frac{\sum_{n_\mu} p_T^{\text{trk}} (\Delta R < 0.3) - p_T^{\mu Z2}}{p_T^{\mu Z1}} < 0.1. \tag{7.2}$$

The comparison between the two cases new ID/isolation and old ID/isolation with respect to the trigger is shown in Fig. 7.6(b). The efficiency stays flat for all l^* masses except the working point $M_{l^*} = 200$ GeV. Here, the tracker relative isolation is inefficient because of pileup tracks which have a higher influence for low p_T muons.

The modifications of ID and isolation lead to a flat signal efficiency. All the modifications applied are:

- One of the two muons from the Z decay is allowed to be a tracker muon instead of a tracker and a global muon. The cut on the muon number of hits is removed for this muon.

(a) PF-isolation for boosted Z muons

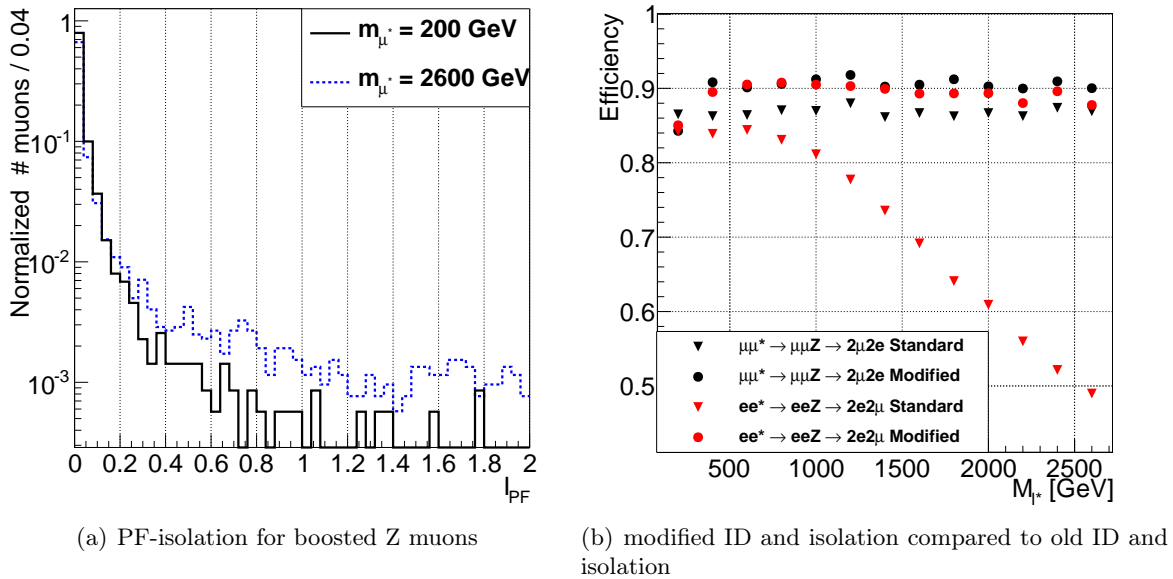(b) modified ID and isolation compared to old ID and isolation

Figure 7.6.: Comparison plots for the old and new isolation criteria.

- Use tracker variables for the $\Delta p_T/p_T$ cut of the selected muon.

- Instead of PF-isolation, tracker based relative isolation is used for both muons from the Z decay. The contribution of the other muon will be removed if the distance between both is $\Delta R < 0.3$.

It has been shown that the modified ID and isolation helps to regain efficiency for the decay of boosted Z-bosons to muons. Now, the effect of this ID on the signal $\mu\mu^* \to \mu\mu Z \to 4\mu$ has to be investigated. Fig. 7.7 shows a comparison between the acceptance × efficiency of the old ID and isolation, new ID and old isolation, and new ID and new isolation. The old configuration leads to a drop in the efficiency to less than 50%. Using the new ID, but old isolation, most of the lost efficiency can be regained. Here, the difference between the old and the new isolation can be seen very well. If the old isolation is used, the efficiency drops for masses above 1600 GeV to a value of about 60%. If the new isolation is applied, the acceptance × efficiency stays flat within the uncertainties for high masses. The value here is about 66%. In all three cases, there are some signal masses with upward- and downward-fluctuations due to limited statistics of the simulated μ^*-samples.

7.2.4. Background Expectation

At this point of the analysis, a first look at the background expectation should be taken to see if there is a deviation in data due to new physics. If this is not the case, the agreement of data and background expectation should be reasonable within the uncertainties. Therefore, the number of expected background events is scaled to the integrated luminosity as described in Sec.6.3.1. Individual contributions for each background are summed up and result in the full expectation. A signal of an excited muon would lead to an excess in data with respect to the background. The statistical uncertainty on the number of background events is calculated by using $\sigma^i_{bkg} = \sqrt{N^i_{passed}}$ where N^i_{passed} is the number of events passing the selection for each MC
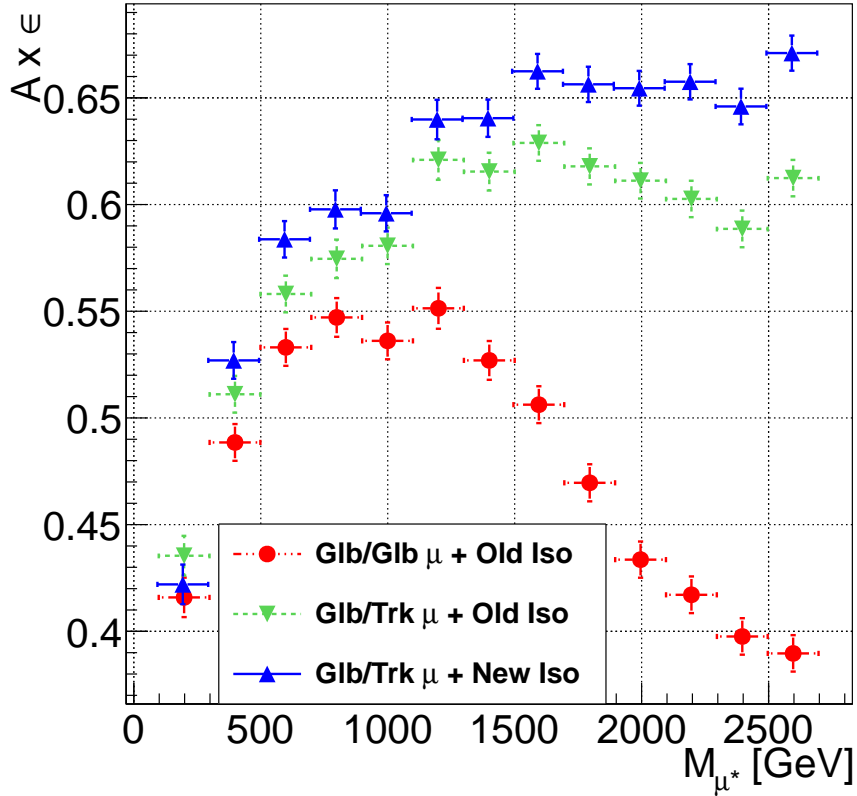
Figure 7.7.: Acceptance × efficiency of the new ID and isolation compared to the old configurations.

sample. This uncertainty then has to be scaled with the same factor as N^i_{passed} afterwards. To get the correct uncertainties of all different backgrounds, they are summed up quadratically. Tab. 7.1 summarizes the values of all samples, their statistical uncertainties, the combined expectation and the number of observed data events. The systematic uncertainties are computed according to Sec. 7.4.

The background expectation at this point is 48.76 ± 0.26 (stat.) ± 7.52 (syst.) events while there are 43 events observed in data. This means that there is less data than expected, but it is still within the systematic uncertainties. Even the statistical uncertainty of the background expectation that is given by $\sqrt{48.76} \approx 6.98$ events, the discrepancy is below one sigma, indicating a reasonable agreement at this point. The table also shows the fraction of each background on the full expectation. As expected, the dominant background process is the $q\bar{q} \rightarrow ZZ$ production with ≈ 93% of the complete background followed by the diboson production via gluon fusion with ≈ 5% such that the combined ZZ production yields in 98% of the total expectation while the other backgrounds contribute to ≈ 2% which is at most one event. Therefore, it is very important to remove as much ZZ background as possible.

In addition to the numbers, it is good to have a look at different characteristic distributions of this analysis. It could be possible to have a serious up-fluctuation in one part of a distribution and a down-fluctuation in another part. This would indicate a wrong background expectation even if the total number of events is reasonable. Fig. 7.8 shows four of the most important

Background	Event Yield	Statistical Uncertainty
$q\bar{q} \to ZZ \to 4\mu$	44.792	0.213
$q\bar{q} \to ZZ \to 2\mu2\tau$	0.274	0.034
$q\bar{q} \to ZZ \to 4\tau$	0.002	0.002
$gg \to ZZ \to 4l$	2.450	0.021
$gg \to ZZ \to 2l2l'$	0.022	0.004
$t\bar{t}Z$	0.556	0.104
$t\bar{t}WW$	0.001	0.001
WWZ	0.199	0.033
WZZ	0.134	0.015
ZZZ	0.086	0.006
$H \to ZZ^* \to 4l$	0.242	0.005
Total	48.76 ± 0.26 (stat.)	
Total (with systematics)	48.76 ± 0.26(stat.) ± 7.52 (syst.)	
Data	43	

Table 7.1.: Event yields for background and data for $\mathscr{L}_{int} = 19.7$ fb^{-1} The corresponding list of the 43 data events is shown in Appendix A.1.

variables for an accurate analysis description. In this plots, "ZZTo4L" stands for the combined background from $q\bar{q}$ annihilation and gluon fusion, "HToZZTo4L" for the combined background from the Higgs production and decay to four leptons, and "Other" for all the other backgrounds. The first distribution (Fig. 7.8(a)) presents the combined invariant mass of all four reconstructed muons. This is the standard variable for most searches concerning four leptons in the final state. This distribution shows a good data over MC agreement. There are no unexpected structures visible. Since this analysis uses a modified ID and isolation for the muons from the Z-boson decay, the ΔR-distribution of those two muons is very important. The Z-boson is selected by searching for opposite sign muon pairs (four per event) and choosing the muon pair with the invariant mass closest to the Z-boson mass $M_Z = 91.19$ GeV. The distribution is given in Fig. 7.8(b), also showing a good agreement. Events with a small ΔR could indicate a signal as well as problems with the modified ID and especially isolation. The last two control distribution are the minimum and maximum invariant mass distributions (Fig. 7.8(c) and 7.8(d)). In Sec. 7.1 it was described that these two distributions are the most characteristic and their combination will be used as the most important indicator for the signal. After reconstructing the Z-boson, one of those distributions should include the reconstructed excited muon if there is one (Fig. 6.6). For all signal except $M_{\mu^*} = 200$ GeV the excited muon tends to be at the high end of the spectrum where the background contribution is small. As it can be seen, at this point of the analysis a good agreement between data and background expectation is given which means that there is no indication for am excited muon here.

7.2.5. Invariant Mass Cuts

As shown in Sec. 7.2.4, there is a reasonable agreement between data and background expectation after applying the identification and isolation criteria. Now, the signal and the background should be separated to see even the smallest possible signal. Therefore, characteristic distributions which are different for signal and background are used. One of the main advantages of this analysis is that one background source is dominating, namely the Standard Model ZZ production constituting in $\approx 98\%$ of the background expectation. Therefore, the prime goal is to discriminate

(a) Invariant mass of all four reconstructed muons

(b) ΔR between the two muons from the Z decay

(c) Minimum invariant mass M_{min}

(d) Maximum invariant mass M_{max}
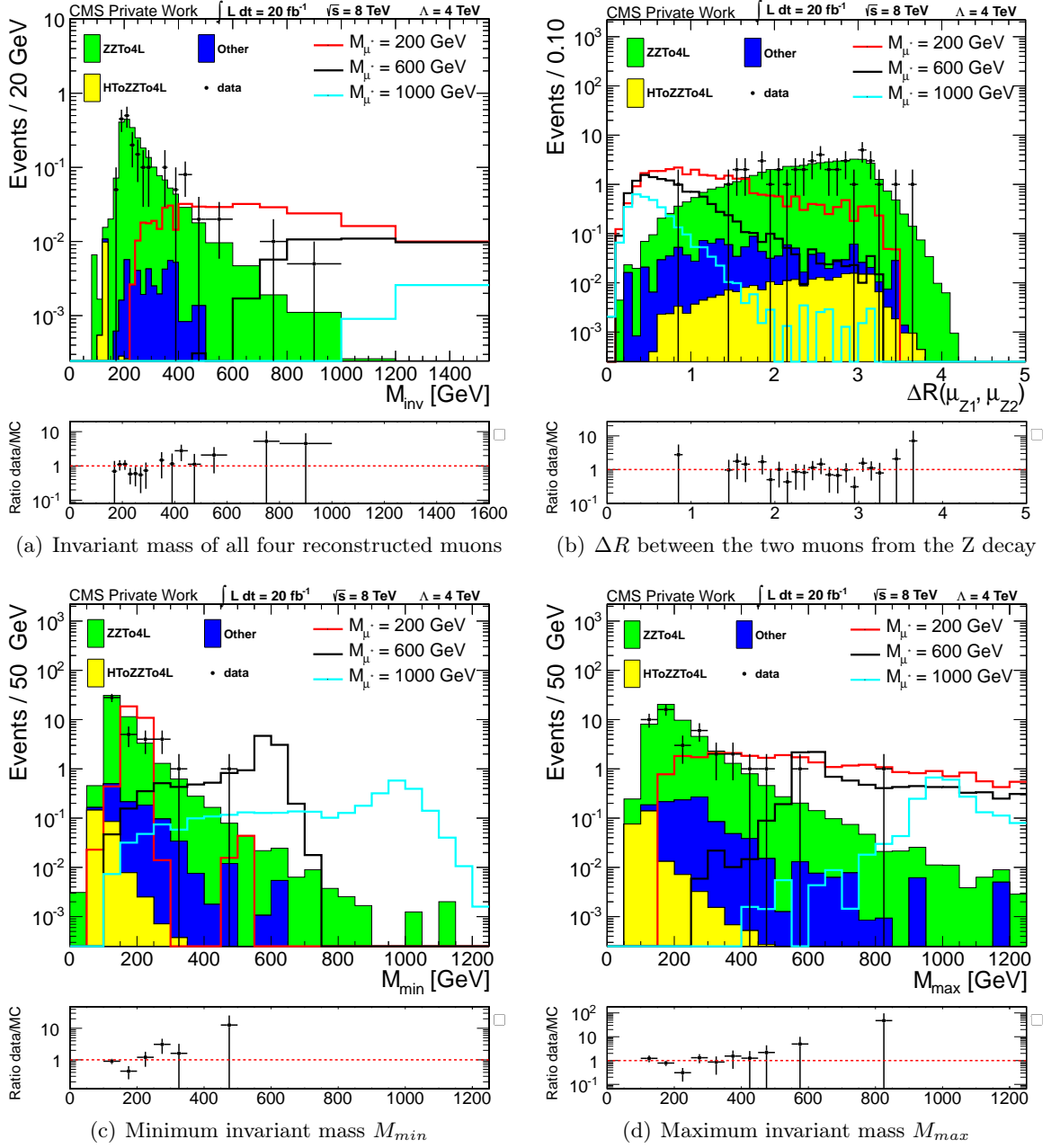
Figure 7.8.: Distributions for the comparison of the agreement between data and Standard Model
            background expectation.

against this background. The main difference between the signal and the diboson background is
the number of Z-bosons. While the signal contains only one Z-boson, the ZZ background should
have two. As explained before, the best Z-boson is selected from opposite sign muon pairs. If
the best one is selected, three other possibilities are left, but only one of them does not contain
a muon which was used to reconstruct the best Z-boson. This pair is used as a second Z-boson.
The distributions of the two reconstructed Z-bosons are given in Fig. 7.9(a) and 7.9(b).

Starting with the first Z-boson in Fig. 7.9(a), one can again observe a reasonable agreement be-
tween data and background. It seems hard to find a selection which would discriminate against

(a) Invariant mass of the best reconstructed Z-boson M_{inv}^{Z}

(b) Invariant mass of the other reconstructed muon pair M_{inv}^{no-Z}

Figure 7.9.: Invariant mass of the two reconstructed muon pairs.

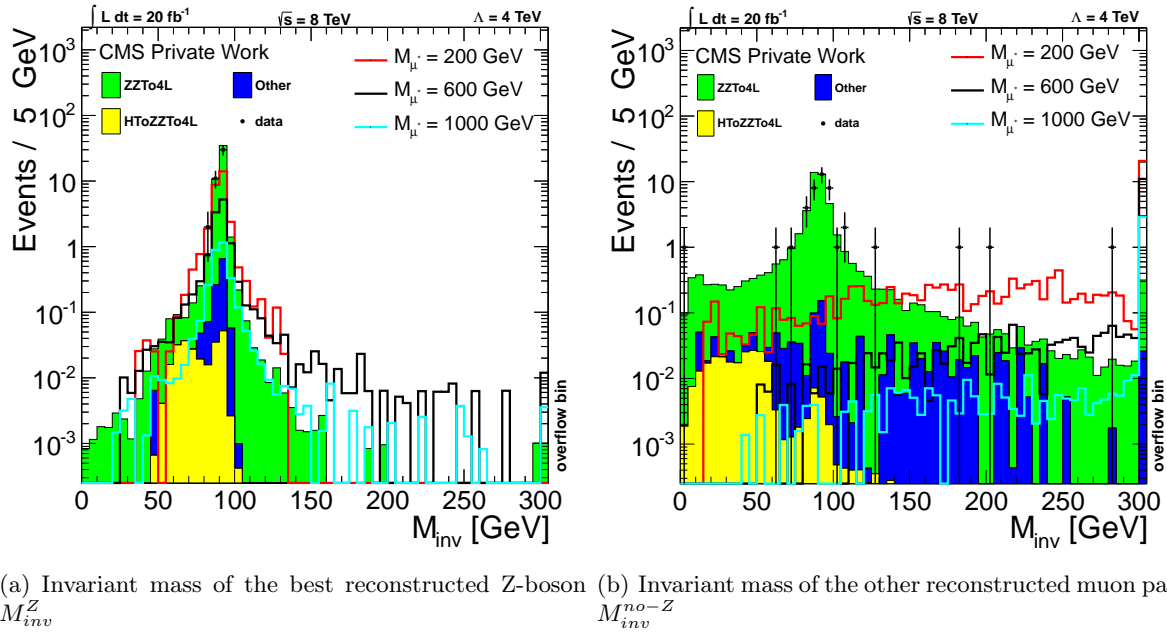the background without cutting also the signal. Nevertheless, to remove the possibility to include not expected events with boosted objects decaying to two muons like for example $J/\Psi \to \mu\mu$, a cut of $M_{inv}^{Z} > 60$ GeV will be set on this muon pair.

The other dimuon mass distribution (Fig. 7.9(b)) looks much more promising. Signal and background clearly have a different shape. Most of the background is gathered around the Z-mass while most of the signal is in the high mass region. With a cut on the invariant mass of $M_{inv}^{no-Z} > 106$ GeV (Z-Veto), the background can be reduced by $\approx 90\%$ while most signal MC sets loose only 1% of their events except the 200 GeV and the 400 GeV signal which loose about 5% and 2.5% of their events due to this cut. Tab. 7.2 summarizes the background expectation after applying the two invariant mass cuts. At this point, only five data events are left while there is a background expectation of 4.74 ± 0.12 (stat.) ± 0.74 (syst.) events. The agreement between data and background is still good after setting the invariant mass cuts and there is no evidence for a signal. Although the Z-Veto was implemented to discriminate against the diboson production, it is still the dominant background. Tab. 7.3 summarizes the five data events which do pass the selection until this point of the analysis, ordered by their maximum invariant mass, starting with the highest one.

7.2.6. Summary of the signal selection criteria

To put everything together, the optimization of the signal selection will be summarized in this section. Starting with the acceptance and trigger cuts, it was decided to use the HLT_Mu17_Mu8 trigger which provides a high efficiency together with acceptance cuts of $|\eta| < 2.4$ and $p_T^{\mu} > 20$ GeV for all four muons. As an identification criteria, the high-p_T muon ID was applied which is optimized for the identification of muons with a transverse momentum beyond 200 GeV. Because of an inefficiency for high μ^*-masses due to nearby muons from the boosted Z decay, this muon identification had been optimized to keep the signal efficiency flat. In addition to this, the

Background	Event Yield	Statistical Uncertainty
$q\bar{q} \to ZZ \to 4\mu$	4.117	0.065
$q\bar{q} \to ZZ \to 2\mu2\tau$	0.016	0.008
$q\bar{q} \to ZZ \to 4\tau$	0	0
$gg \to ZZ \to 4l$	0.156	0.005
$gg \to ZZ \to 2l2l'$	0	0
$t\bar{t}Z$	0.318	0.078
$t\bar{t}WW$	0.001	0.001
WWZ	0.107	0.025
WZZ	0.015	0.005
ZZZ	0.001	0.001
$H \to ZZ^* \to 4l$	0.004	0.0002
Total	4.74 ± 0.12 (stat.)
Total (with systematics)	4.74 ± 0.12 (stat.) ± 0.74 (syst.)
Data	5

Table 7.2.: Event yields for background and data after applying invariant mass cuts.

Run	Lumi Section	Event	M_{min} (GeV)	M_{max} (GeV)
206745	1477	1407561357	299	375
199876	258	299199538	167	329
206512	393	522300157	259	268
206401	87	69962177	129	182
206477	182	276785714	125	172

Table 7.3.: List of events left after applying invariant mass cuts. The corresponding event displays are presented in Appendix A.2.

isolation was modified by removing the contribution of the isolation cone from the other muon. This modifications lead to a high and flat efficiency. After applying the ID and isolation, two invariant mass cuts have been set to optimize the ratio between signal and background. The more important one of this cuts is the Z-Veto which discriminates the background highly while conserving the signal efficiency. Tab. 7.4 summarizes the different selection criteria applied until now. A Cut flow table for each background, data and some signal examples is given in Tab. 7.5 for the main cuts.

Fig. 7.10 shows the breakdown of the acceptance $\times$ efficiency for each cut. It can be seen that the efficiency stays flat up to high masses and that the influence of the invariant mass cuts is very slow except for $\mu^* = 200$ GeV where the efficiency loss is 5 %. The two-dimensional $M_{min} - M_{max}$ plane is shown in Fig. 7.11 and the minimum and maximum invariant mass distributions are presented in Fig. 7.12. The five candidate events which are left after applying the full selection are all in the area around 200 GeV and match the background expectation. The error bands include systematic uncertainties on Pileup re-weighting, muon momentum scale and muon resolution. These and other background uncertainties will be discussed in Sec. 7.4.

Cut Variable	Standard μ-pair	Boosted Z μ-pair
Number of muons	4	
Geometrical Acceptance	$\lvert\eta\rvert < 2.4$	
Transverse Momentum	$p_T > 20$ GeV	
Trigger	HLT_Mu17_Mu8	
Number of muons	2	2
Global Muon	True	False
Tracker Muon	True	True
Muon Hits in Global Track	≥ 1	-
Muon Stations	≥ 2	≥ 2
Tracker Layers	≥ 6	≥ 6
Pixel Hits	≥ 1	≥ 1
Impact Parameter d_{xy}	< 0.02 cm	< 0.02 cm
Longitudinal distance d_z	< 0.5 cm	< 0.5 cm
$\Delta p_T / p_T < 0.3$	True (Cocktail p_T)	True (Tracker p_T)
Particle Flow Isolation	< 0.2	-
Modified Relative Tracker Isolation	-	< 0.1
Opposite Sign	no	yes
Invariant Mass Cut	-	> 60 GeV
Z Veto	> 106 GeV	-

Table 7.4.: Summary of selection steps applied in this analysis.

Sample	Raw	Acceptance	Trigger	ID and Isolation	Mass Cuts
$q\bar{q} \to ZZ \to 4\mu$	1516.05	65.76	65.67	44.79	4.12
$q\bar{q} \to ZZ \to 2\mu2\tau$	3483.11	1.31	1.25	0.27	0.02
$q\bar{q} \to ZZ \to 4\tau$	1516.05	0.01	0.01	0.00	0
$gg \to ZZ \to 4l$	94.62	3.624	3.62	2.45	0.16
$gg \to ZZ \to 2l2l'$	237.14	0.09	0.09	0.02	0
$t\bar{t}Z$	4100.1	11.90	8.31	0.56	0.32
$t\bar{t}WW$	40.15	0.18	0.12	0.00	0.00
WWZ	1247.77	2.77	1.28	0.20	0.11
WZZ	378.87	0.78	0.52	0.13	0.02
ZZZ	90.42	0.20	0.18	0.09	0.00
$H \to ZZ^* \to 4l$	115.05	0.58	0.57	0.24	0.00
Total Background	10971.5	87.19	81.62	48.76	4.74
Data	-	120976	30586	43	5
200 GeV	100%	60.9%	60.8%	42.5%	40.3%
1000 GeV	100%	78.2%	78.1%	60.0%	58.9%
1800 GeV	100%	85.0%	84.8%	65.0%	64.3%
2600 GeV	100%	87.9%	87.7%	67.1%	66.0%

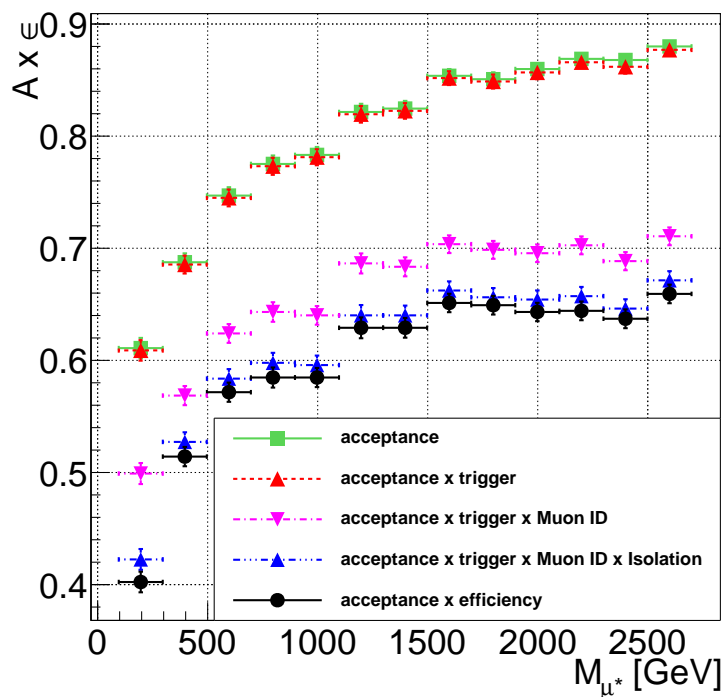Table 7.5.: Cut Flow Table for $\mu\mu^* \to \mu\mu Z \to 4\mu$.

Figure 7.10.: Overall acceptance × efficiency.

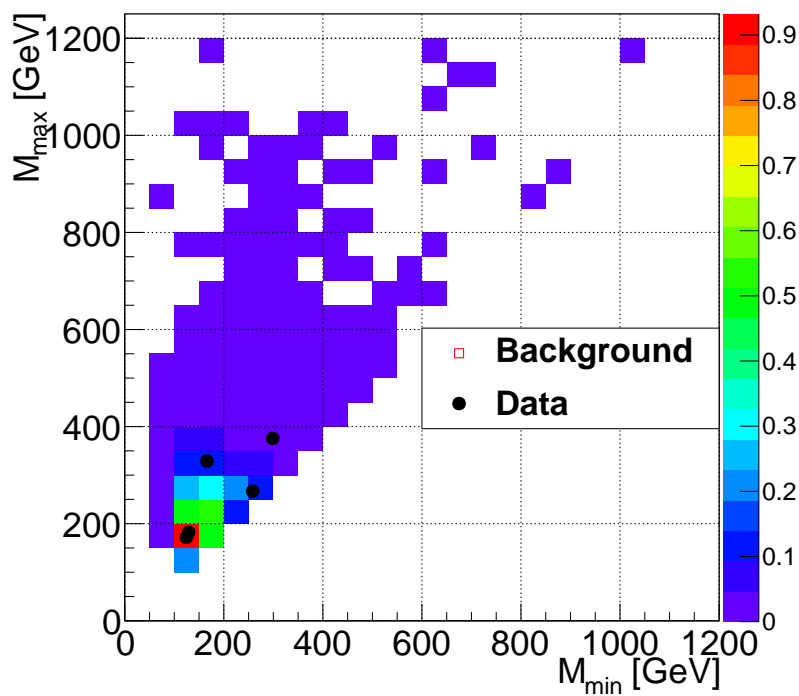Figure 7.11.: Two-dimensional minimum-maximum invariant mass plane for data and background expectation.
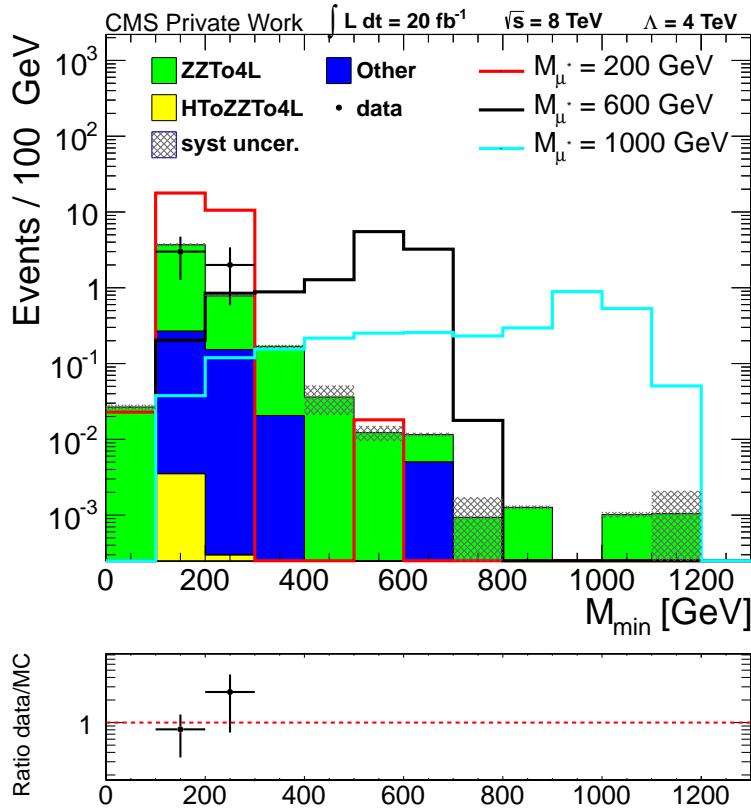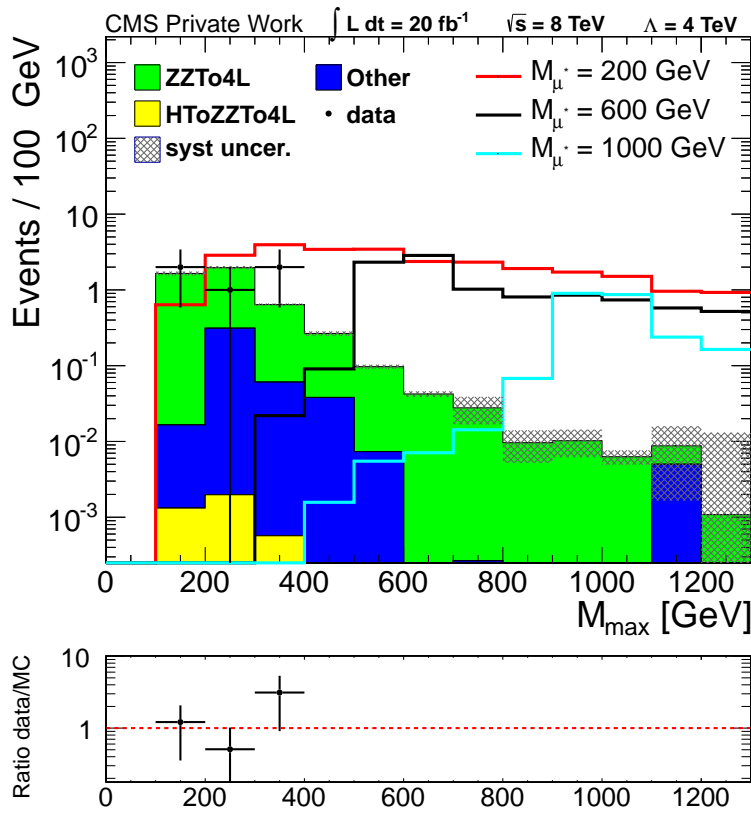
(a) Minimum invariant mass M_{min}

(b) Maximum invariant mass M_{max}

Figure 7.12.: Minimum and maximum invariant mass distribution after applying all the cuts. The uncertainty bands include muon scale, muon resolution and pileup uncertainties, but no uncertainties on the cross section and luminosity.

7.3. Corrections to the background expectation

Although the detector simulation performs quite well, there can be still some differences between data and Monte-Carlo efficiencies that can lead to an imperfect background prediction. Such differences can come from the trigger, the muon ID and isolation, and pileup re-weighting. Since there are no official correction factors for the dimuon-trigger available yet and the efficiency can be expected to be close to one for data and background, no corrections were applied for it. The corrections due to pileup re-weighting and muon identification efficiencies will be discussed below.

Pileup re-weighting

At the LHC, the protons circulate in bunches with a time difference of 50 ns for each bunch crossing. Due to the high amount of protons in each bunch (round about 10^{11}), there are multiple interactions per bunch crossing which are called pileup. Two kinds of pileup can lead to contributions within the detector: The in-time and the out-of-time pileup. While the in-time pileup is produced in the same bunch crossing as the event of interest and therefore is the more important effect, the out-of-time pileup comes from earlier bunch crossings since some of the detector components (for example HCAL) have a response time larger than 50 ns. Both pileup contributions depend on the luminosity, a higher number of protons increases the in-time pileup and a shorter time between two bunch crossings would produce more out-of-time pileup.
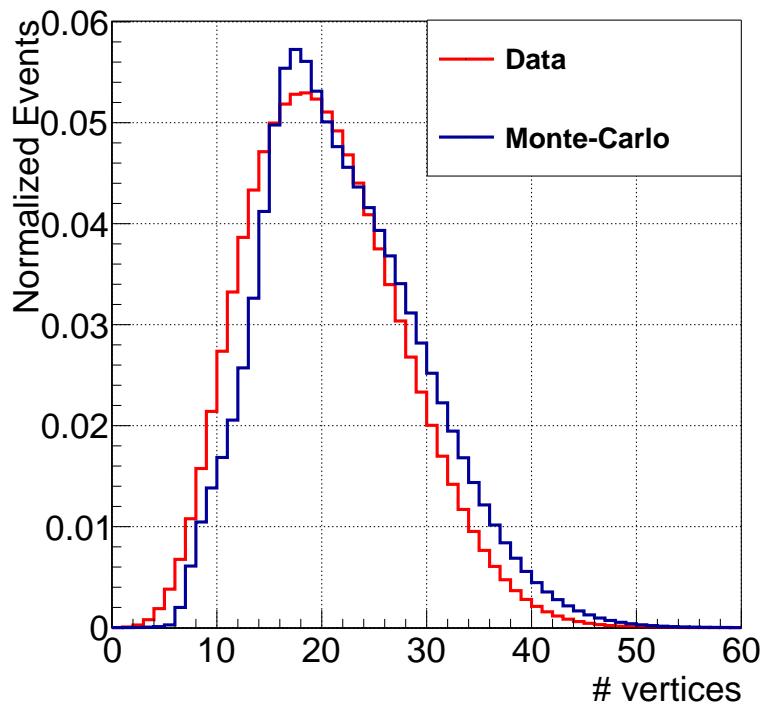

Figure 7.13.: Comparison of the normalized pileup distribution in Monte-Carlo simulation and data.

Although the Monte-Carlo simulation includes a pileup scenario, there can be still some differences between the Monte-Carlo pileup expectation and the real pileup contribution in data. One

reason therefor is that the pileup in data changed with the time while the MC scenario stays the same [74]. A comparison between the normalized pileup distribution in data and Monte-Carlo is presented in Fig. 7.13. Data and Monte-Carlo distribution look similar which means that the expectation fits the measurement quite good. The pileup scenario of the Monte-Carlos used in this analysis is the S10-scenario from Summer 2012. The distribution of it is based on [58].

Although the shape of the pileup distributions in Monte-Carlo and data look similar (see Fig. 7.13), there are still some differences (data > MC for low pileup, data < MC for high pileup) that can cause a discrepancy due to missing re-weighting. Therefore, the Monte-Carlo expectation is weighted according to the ratio of the true number of interactions of an event in data and Monte-Carlo. The best distributions to study the influence of pileup re-weighting on the analysis are the number of vertices before and after applying pileup re-weighting. These distributions are shown in Fig. 7.14 after applying all selection steps except the invariant mass cuts for events with four muons to keep statistics high. In the case of this analysis, the effect of pileup seems to be small, but it is still visible that the distribution after using pileup re-weighting fits the data a bit better. The pileup re-weighting is applied to all data and background distributions shown in this thesis. The systematic uncertainties on this procedure will be discussed in Sec. 7.4.
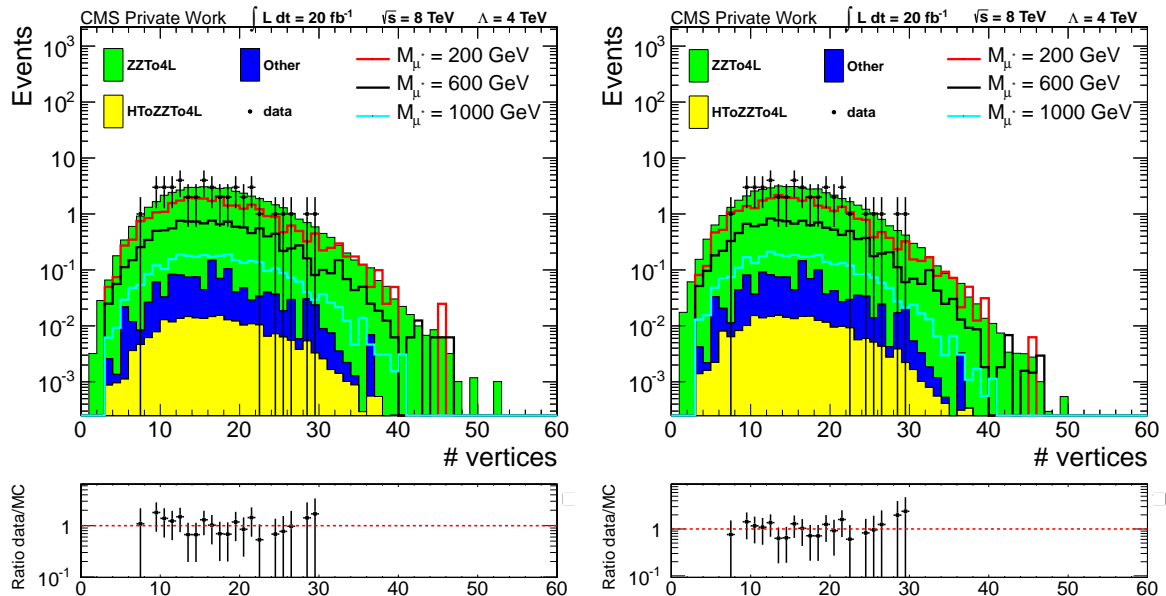
Figure 7.14.: Number of vertices distribution without pileup re-weighting (left) and with pileup re-weighting (right).

Muon Selection Efficiencies

As discussed before, there can be differences in the muon selection efficiency in Monte-Carlo compared to the efficiency in data. In order to get a more accurate description of the background, it has to be weighted with scale factors that are calculated from the ratio of the data efficiency with respect to the Monte-Carlo efficiency for each muon. The scale factors are computed by the Muon POG for each identification criterion and isolation algorithm in dependence of the pseudo-rapidity η for $|\eta| < 0.9$, $0.9 < |\eta| < 1.2$, $1.2 < |\eta| < 2.1$, and $2.1 < |\eta| < 2.4$ using the tag and probe method [75]. If possible, the scale factors provided by the Muon POG will be used [76]. This is the case for the two muons which use the standard high-p_T muon ID with

PF-isolation. In case of the two muons with the modified boosted Z ID and isolation, one has to distinguish between both muons. To the first one which uses the standard high-p_T ID with a modified isolation, the official scale factor for the ID can be applied, but not for the isolation. The other muon has modified ID and isolation criteria which means that there is no official scale factor for it. In this case, scale factors which were computed by the $X \to ZZ \to qqll$ analysis will be used [71]. This analysis also includes boosted Z-bosons decaying to muons and therefore they are using the same modifications. The scale factors applied to the boosted Z muons are summarized in Tab. 7.6 while the factor for the standard muon ID and isolation are presented in Tab. 7.7. The uncertainties are only statistical uncertainties, the systematics uncertainties are discussed in Sec. 7.4

$|\eta|$ bin	p_T (GeV)	GlobalID*ISO	TrackerID*ISO
	20-40	0.9972 ± 0.0004	0.9989 ± 0.0004
	40-60	0.9948 ± 0.0003	0.9973 ± 0.0003
$0 < |\eta| < 0.9$	60-80	1.0018 ± 0.0011	1.0029 ± 0.0010
	80-100	1.0076 ± 0.0025	1.0096 ± 0.0023
	100-500	1.0068 ± 0.0039	1.0075 ± 0.0037
	20-40	0.9971 ± 0.0007	0.9988 ± 0.0007
	40-60	0.9963 ± 0.0005	0.9985 ± 0.0005
$0.9 < |\eta| < 1.2$	60-80	1.0014 ± 0.0022	1.0028 ± 0.0021
	80-100	1.0060 ± 0.0049	1.0060 ± 0.0047
	100-500	1.0058 ± 0.0080	1.0050 ± 0.0077
	20-40	1.0001 ± 0.0004	0.9999 ± 0.0005
	40-60	0.9982 ± 0.0004	0.9985 ± 0.0004
$1.2 < |\eta| < 2.1$	60-80	1.0039 ± 0.0017	1.0039 ± 0.0016
	80-100	1.0129 ± 0.0039	1.0081 ± 0.0036
	100-500	1.0185 ± 0.0065	1.0180 ± 0.0063
	20-40	1.0015 ± 0.0030	1.0028 ± 0.0009
	40-60	0.9955 ± 0.0012	0.9985 ± 0.0009
$2.1 < |\eta| < 2.4$	60-80	0.9929 ± 0.0071	0.9927 ± 0.0024
	80-100	0.9834 ± 0.0092	0.9839 ± 0.0082
	100-500	1.0438 ± 0.0160	1.0083 ± 0.0099

Table 7.6.: Scale factors used for the modified muon ID and isolation, taken from $X \to ZZ \to qqll$ Analysis Note [71].

7.4. Systematic Uncertainties

There are different sources of systematic uncertainties, some of them have a huge impact, others do not add a measurable contribution to the final result. The way how they are applied to the background expectation also differs, depending on the fact if the uncertainties are based on the object characteristics (muon scale and resolution), the event characteristics (pileup) or the full background (ZZ cross section and luminosity). All systematics which have been taken into account are summarized below.

- **Trigger efficiency:** The uncertainty on the trigger efficiency is negligible. The dimuon-trigger has an efficiency of nearly 100 % for a four muon final state and therefore its uncertainty is very small.

(a) Scale factors for standard high-p$_T$ ID.

p_T (GeV)	$|\eta|$ bin	Data	MC	Data/MC
> 20 GeV	$0 < |\eta| < 0.9$	0.9582 ± 0.0001	0.9650 ± 0.0001	0.9930 ± 0.0002
	$0.9 < |\eta| < 1.2$	0.9612 ± 0.0002	0.9668 ± 0.0002	0.9942 ± 0.0003
	$1.2 < |\eta| < 2.1$	0.9535 ± 0.0002	0.9565 ± 0.0002	0.9968 ± 0.0002
	$2.1 < |\eta| < 2.4$	0.9495 ± 0.0004	0.9530 ± 0.0004	0.9963 ± 0.0006
> 45 GeV	$0 < |\eta| < 0.9$	0.95542 ± 0.0002	0.9651 ± 0.0002	0.9900 ± 0.0003
	$0.9 < |\eta| < 1.2$	0.9587 ± 0.0004	0.9661 ± 0.0004	0.9923 ± 0.0006
	$1.2 < |\eta| < 2.1$	0.9506 ± 0.0003	0.9554 ± 0.0003	0.9949 ± 0.0004
	$2.1 < |\eta| < 2.4$	0.9398 ± 0.0008	0.9472 ± 0.0008	0.9923 ± 0.0012

(b) Scale factors for standard PF-isolation.

p_T (GeV)	$|\eta|$ bin	Data	MC	Data/MC
> 20 GeV	$0 < |\eta| < 0.9$	0.6762 ± 0.0001	0.9769 ± 0.0001	0.9994 ± 0.0001
	$0.9 < |\eta| < 1.2$	0.9846 ± 0.0001	0.9801 ± 0.0002	1.0014 ± 0.0002
	$1.2 < |\eta| < 2.1$	0.9846 ± 0.0001	0.9832 ± 0.0001	1.0014 ± 0.0001
	$2.1 < |\eta| < 2.4$	0.9768 ± 0.0004	0.9512 ± 0.0004	1.0269 ± 0.0004

Table 7.7.: Scale factors for the standard high-p_T muon ID and PF isolation, taken from [76].

- **Muon efficiency scale factors:** The systematic uncertainties on the muon efficiencies are estimated to 0.5 % for the muon ID and 0.2 % for the isolation criteria per muon [75]. The effect on the background yield is about 2 % in case of the muon ID and about 0.8 % for the isolation. The statistic uncertainties on the muon scale factor are negligible.

- **Muon momentum:** As discussed several times before, the most important object of this analysis are muons. While most muons of the background have a soft p_T spectrum, the muons of the high mass signals go up to high transverse momenta. In this region, the measurement of the momentum is not very precise. Therefore, the uncertainties on the muon momentum scale and the muon resolution have to be understood well.

  - The **muon momentum scale** was measured by the Muon POG by using cosmic muons. To evaluate the uncertainty on the scale, the transverse momentum of each muon is shifted by $\pm$ 5 % per TeV [77]. This means that a muon with $p_T = 200$ GeV has an uncertainty of 1 %. If it comes to bin-to-bin fluctuation, the muon momentum scale is the dominant uncertainty. The estimation of the muon scale uncertainty leads to two additional histograms of the final distribution after applying each analysis cut with shifted transverse momenta. Although the muon scale uncertainty is dominant for bin-to-bin fluctuation, its influence to the final event yield depends only on the fact if the shifted event passes each cut or not, leading to an uncertainty of 1.5 % on the background and 0.2 % on the signal yield before applying the final selection cut.

  - For the estimate of the **muon resolution** uncertainty, the p_T of each muon is smeared with a Gaussian by a value of 3.2 % [41]. This uncertainty is based on the resolution measurement of cocktail muons at high transverse momentum. In contrast to the muon scale uncertainty, only one shifted histogram is filled. At low transverse momenta, this uncertainty is higher than the muon scale uncertainty, leading to an error of 4.7 % on the background and 0.3 % on the signal yield. In both cases, muon scale and muon resolution, the uncertainty comes mainly from events passing the Z veto. This number is much higher in background events than in signal events.

- **Pileup re-weighting:** There are different sources of uncertainties in the pileup re-weighting procedure. The dominant one is the uncertainty due to the number of interactions. It depends on the luminosity uncertainty and on the measurement of the total inelastic cross section which is expected to be 69.4 mb based on a best fit analysis in data and Monte-Carlo for $Z \to \mu\mu$ events. The combination of these two uncertainties leads to a value of 3.9 % in 2012 for the number of interactions. Additional uncertainties could arise from differences within the kinematic distributions of pileup in data and Monte-Carlo. To cover all these uncertainties, two additional pileup distributions for data with a recommended shift of $\pm$ 5 % in the total inelastic cross section will be produced [78]. These distributions lead to two other final distributions with the same event number, but different event weights. The impact of this uncertainty on the event yield is smaller than 1 %.

- **ZZ cross section:** The cross section of the process $ZZ \to 4l$ is not well known yet since it is a rare process. Therefore, an uncertainty of 15 % will be used for this background based on the measurements from [79]. Since the background is dominated by ZZ production, this uncertainty has an influence on the background yield of nearly 15 %, leading to an up- or down-shift of this order, it has no influence on the signal expectation. In most cases, the ZZ cross section uncertainty will be the dominant background uncertainty within the limit setting.

- **Luminosity:** The uncertainty on the recorded luminosity $\mathscr{L}_{int} = 19.7 \, \text{fb}^{-1}$ is considered to be 2.6 % [54]. Same as for the ZZ cross section uncertainty, this uncertainty influences the background directly. A shift by 2.6 % would lead to the same difference in the background and signal expectation. Therefore, it can directly be applied to the limit calculation.

The relative uncertainty of the bin-to-bin uncertainties (muon scale, muon resolution and pileup re-weighting) with respect to the minimum and maximum invariant mass as well as to the muon p_T is presented in Fig. 7.15. While the invariant mass plots show the uncertainty after applying the invariant mass cuts, the p_T-distribution was produced before this step. Although the final distribution will be the 2-dimensional $M_{min} - M_{max}$-plane, it is easier to see the impact of the uncertainties on each bin in the M_{min}- and M_{max}-distribution. The statistics of the plots is limited which can lead to fluctuation from bin-to-bin. It can be seen that the pileup uncertainty is nearly constant and that its influence on the bin value is very small. The resolution uncertainty is dominant in the low M_{inv} region and the muon scale gets dominant for high invariant masses region. In the next chapter, the uncertainties will be used together with the data, background and signal yields to calculate a cross section limit on the process $\mu\mu^* \to \mu\mu Z \to 4\mu$ in dependence of a final selection cut.
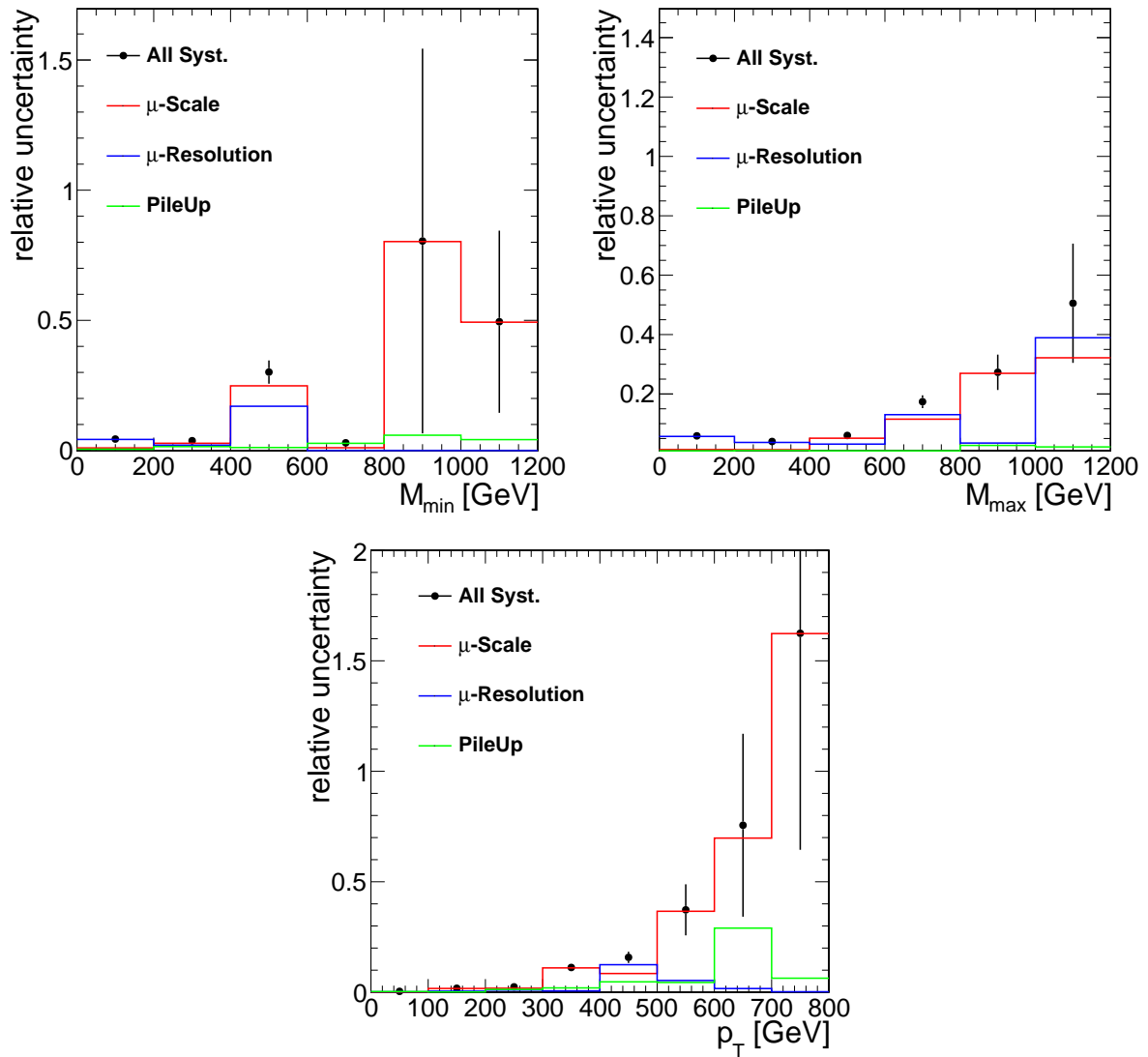
Figure 7.15.: Relative systematic uncertainties on the background expectation for pileup re-weighting, muon momentum scale and muon momentum resolution. Top left: M_{min}-distribution; Top right: M_{max}-distribution; Bottom: p_T-distribution.

8. Results

After applying all selection criteria, there is no visible excess in the minimum or maximum invariant mass spectrum. Since there seems to be no hint for excited muons in the channel $\mu\mu^* \to \mu\mu Z \to 4\mu$, an exclusion limit will be set on the existence of them. Because the theoretical cross section depends on the compositeness scale Λ, the limit changes for different Λ values which will be taken into account.

8.1. Bayesian Limit Method

The strategy is to use a single bin counting experiment for the limit setting. This means the input for the limit calculation will be the expected number of signal events s (or the signal efficiency ϵ), background events b, data events N and the corresponding systematic and statistical uncertainties in a certain search region of the final distribution (Sec. 8.2) which is optimized for the best signal sensitivity in comparison to the background expectation. The selection of the search window of this analysis is based on an "L-shape" cut in the minimum-maximum invariant mass plane and will be discussed more detailed in Sec. 8.2. The selection of single bin counting is appropriate here due to low statistics, a missing excess in data, and a small background expectation. There are two common methods to determine a cross section limit: The frequentist and the Bayesian method. Since this analysis uses the latter one, it will be described more accurately based on [3, 80] here.

While the frequentist method compares the signal plus background hypothesis to the number of measured data events, the Bayesian approach depends on a Poisson Likelihood distribution as a function of N under the precondition of s:

$$L(N|s) = \frac{(s+b)^N}{N!} \cdot e^{-(s+b)} \tag{8.1}$$

where the number of background events b is constant. Based on Bayes' Theorem

$$P(B|A) = \frac{P(A|B) \cdot P(B)}{P(A)} \tag{8.2}$$

one gets the posterior probability density function (p.d.f) for s under the precondition of N

$$p(s|N) = \frac{L(N|s)\pi(s)}{\int L(N|s)\pi(s)ds} \tag{8.3}$$

where $\pi(s)$ is the prior probability for s. Based on the expectation that the mean s is unknown, but positive, $\pi(s)$ is given by

$$\pi(s) = \begin{cases} 0, & s < 0 \\ 1, & s \geq 0 \end{cases} \tag{8.4}$$

in this analysis. Since some quantities include systematic uncertainties, an additional prior function $\pi(\vec{\nu}) = \prod_i \pi(\nu_i)$ is added to the Likelihood to take the uncertainties into account. Every systematic uncertainty is inserted as a component to the vector $\vec{\nu}$ and handled as a nuisance parameter that is based on a log-normal distribution. Every included nuisance parameter results in a smearing of the of the Likelihood function which gets larger for increasing systematic uncertainties. The implementation of the prior function $\pi(\vec{\nu})$ leads to the new p.d.f.

$$p(s|N) = \frac{L(N|s)\pi(s)\pi\vec{\nu}}{\int \int L(N|s)\pi(s)\pi(\vec{\nu})dsd\vec{\nu}}.$$
(8.5)

Based on this function, an upper limit on the signal contribution s_{up} can be computed to a confidence level $1 - \alpha = 95\%$ by using

$$1 - \alpha = 0.95 = \int_{-\infty}^{s_{up}} p(s|N).$$
(8.6)

To get the cross section limit, s_{up} has to be divided by the integrated luminosity. In addition to the observed cross section limit also an expected limit will be calculated to compare the background expectation with the observation. Therefore, the background expectation N_{bkg} will be used as the mean value of a Poisson distribution. Then, a number of pseudo-experiments is performed where the background expectation is diced according to this distribution. The determined number of each experiment is then used as the input for the limit calculation, leading to many different limits on the signal contribution. The median of these limits is used as the expected limit while the 1σ and the 2σ error bands are obtained by the region with 68.3% and 95.4% of all limits. As long as there is no large difference between the background expectation and the data observation, the observed limit should be within the error bands of the expected limit.

8.2. Final Optimization of the Search Window

To optimize the data to background ratio for each signal mass, a final cut will be applied. This is done within the limit setting by Matthias Endres [81] for the excited leptons analysis group [66]. As discussed before, the minimum invariant mass distribution gives the chance to optimize the final cut for low masses while the maximum invariant mass distribution is more helpful in the high mass region. Since cuts in the two mass distributions are correlated, it makes no sense to set a first cut on M_{min} and afterwards a second cut on M_{max}. Therefore, the two-dimensional minimum-maximum invariant mass plane will be used to select the final search window. As shown in Sec. 7.1, the signal should have the shape of an inverted "L" in this plane. Fig. 8.1(a) presents the L-shape distribution for different μ^*-signals after the full selection criteria are applied. In contrast to the L-shape distribution on generator level, the width of the "L" is much larger after the full detector simulation due to muon resolution. The effect of muon resolution gets larger for increasing transverse momentum which is the case for higher μ^*-masses.

While the signal has the shape of an inverted "L", there should not be a similar structure for the background. This will be used to distinguish between signal and background. Therefore, four cuts are set around the shape of the signal, also forming an inverted "L", two on M_{min} in dependence of M_{max} (vertical cuts in the plane) and two on M_{max} in dependence of M_{min} (horizontal cuts). The cuts are applied symmetrically around the signal and are optimized for

(a) Minimum-maximum invariant mass plane for differ-
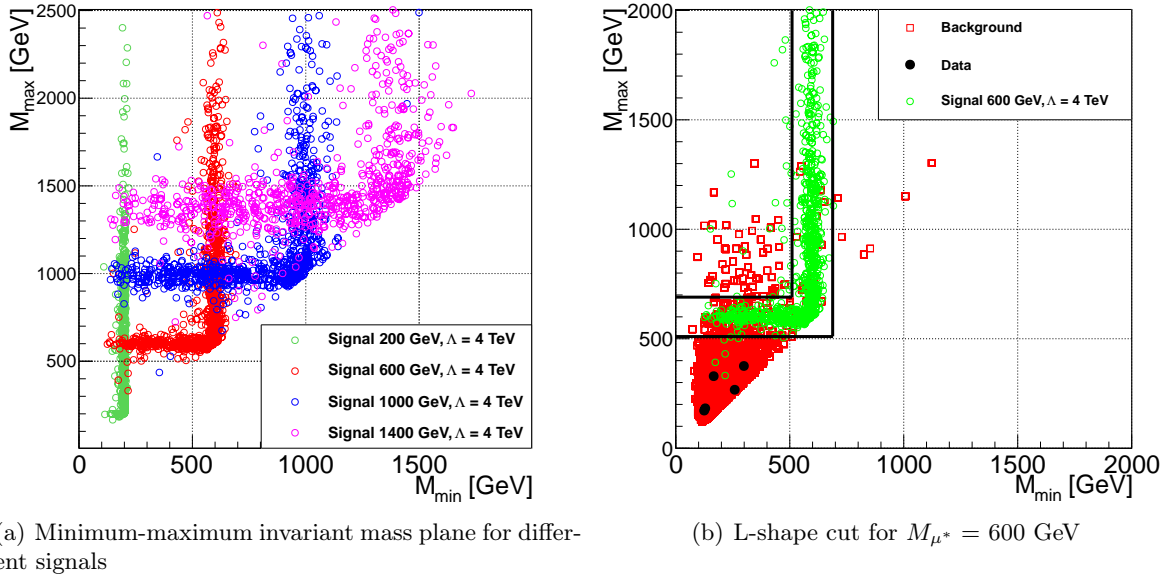ent signals

(b) L-shape cut for $M_{\mu^*} = 600$ GeV

Figure 8.1.: Two-dimensional minimum-maximum invariant mass plane (a) for different signal
masses (Gen-Level in Fig. 7.1) and (b) for the "L-shape" cut of $M_{\mu^*} = 600$ GeV
after applying the full selection. The histogram includes 5 data points, the two on
the bottom-left are close to each other.

the highest sensitivity. The first cut is the lower maximum invariant mass cut which is set
on $M_{max} > M_{\mu^*} - x$ for $0 < M_{min} < M_{\mu^*} + x$ where x is the width of the selected L-shape
cut. The other three cuts which were applied are the upper M_{max} cut ($M_{max} < M_{\mu^*} + x$ for
$0 < M_{min} < M_{\mu^*} - x$), the lower M_{min} cut ($M_{min} > M_{\mu^*} - x$ for $M_{\mu^*} + x < M_{max} < 7000$),
and the upper M_{min} cut ($M_{min} < M_{\mu^*} + x$ for $M_{\mu^*} - x < M_{max} < 7000$). An example how
the L-shape cut looks like is given in Fig. 8.1(b) for $M_{\mu^*} = 600$ GeV. It can be seen that the
selection should conserve the signal efficiency while discriminating against a large part of the
background.

A summary of the results of the final selection is shown in Tab. 8.1. As expected, the width
of the L-shape cut increases with the excited muon mass. For masses beyond 1000 GeV, the
lower maximum invariant mass cut stays the same since there is nearly no background left and
the signal efficiency stays flat in this region (see Tab. 7.5 and Fig. 7.10). Here, the signal
expectation is only limited by the decreasing cross section. As a result, the L-shape cut gets
very broad for high masses and the background expectation as well as the number of data events
stays the same. Except for the 400 GeV mass point, there is no data event left after applying
the final selection cut. The background expectation is below one and the signal efficiency is still
on nearly the same level as before the L-shape cut.

The results of the final selection are now used to calculate a cross section exclusion limit. For
this purpose, the Higgs Combined analysis tool [82] which is based on RooStats [83] will be
used. This tool gives the possibility to calculate single bin limits as well as multi bin limits
and to combine limits for several channels. It also includes different algorithms and methods to
compute limits. As discussed, the Bayesian calculation method will be used here. All the values
which will be computed are with respect to 95 % Confidence Level (C.L.), meaning that there is

M_{μ^*} (GeV)	Cut Range (GeV)	N_{data} (Events)	N_{bkg} (Events)	$N_{\text{signal}}^{\Lambda=M_{\mu^*}}$ (Events)
200	190-210	0	0.93 ± 0.16	252880
400	368-432	1	0.27 ± 0.05	12528
600	510-690	0	0.14 ± 0.03	1835
800	640-960	0	0.07 ± 0.02	372
1000	800-1200	0	0.04 ± 0.01	93.8
1200	800-1600	0	0.04 ± 0.01	30.6
1400	800-2000	0	0.04 ± 0.01	10.1
1600	800-2400	0	0.04 ± 0.01	3.82
1800	800-2800	0	0.04 ± 0.01	1.42
2000	800-3200	0	0.04 ± 0.01	0.585
2200	800-3600	0	0.04 ± 0.01	0.233
2400	800-4000	0	0.04 ± 0.01	0.097
2600	800-4400	0	0.04 ± 0.01	0.043

Table 8.1.: Summary of the L-shape cut results, showing the cut ranges and the selected number of data, background and expected number of signal events for all invariant mass points.

still a chance of five percent that the hypothesis of excluding a certain cross section was wrong. The output of the limit tool is the ratio between the excluded cross section for the Standard Model and the theory cross section which was used as an input. If this value is smaller than one, the theory can be excluded for this mass point. Since we are interested in the exclusion limit of the cross section and want to have the chance to reinterpret it in a model independent way, the ratio has to be multiplied with the input signal cross section. The results of the limit computation are listed in Tab. 8.2, showing the expected limit with uncertainties as well as the observed limit for every mass point. The cross section which can be excluded by this analysis is between 0.5 fb and 0.2 fb, depending on the μ^*-mass. Except for the 200 GeV mass point with zero observed and one expected event and the 400 GeV mass point with 1 observed and 0.27 expected events, there is a very good agreement between the expected and the observed cross section limit. Even those two points are within the uncertainties of the expected limit.

The search windows for the different mass points do not cover the full M_{min}-M_{max} mass plane (Tab. 8.1). For example, there would be no chance to find an excited muon with $M_{min} = 250$ GeV and $M_{max} = 300$ GeV by using these search windows. Therefore, a fit has been applied to fill the gaps between the different search regions. The starting point for this fit is the final distribution from the $ee^* \to eeZ \to 4e$ analysis [66]. Since one goal is the combination of different channels, it is important that all channels have the same mass points. The 4e-channel has the best resolution and therefore, its step size is the smallest and can be used for the other channels, also for $\mu\mu^* \to \mu\mu Z \to 4\mu$. Although the step size can be the same, the width of the search window has to be adapted to the 4μ-channel by taking the increasing resolution into account. After the additional mass points and the corresponding search window widths have been selected, a fit has to be performed to estimate the yield of the signal as a function of the excited muon mass. Since this fit is applied to the number of signal events, it includes the increase of efficiency and the decrease of the cross section. Fig. 8.2 shows the fit result (red line) of the signal numbers for $\Lambda = 2$ TeV as a function of the excited muon mass. The function used for the fit is

M_{μ^*} (TeV)	$\sigma_{\text{theory}}^{\Lambda=M_{\mu^*}}$ (fb)	Exp. Limit $\pm 1\sigma \pm 2\sigma$ (fb)	Obs. Limit (fb)
0.2	36732	$0.605^{+0.194+0.393}_{-0.166-0.176}$	0.444
0.4	1713	$0.329^{+0.147+0.263}_{-0.007-0.014}$	0.495
0.6	207	$0.274^{+0.009+0.139}_{-0.005-0.011}$	0.277
0.8	38.9	$0.264^{+0.006+0.143}_{-0.005-0.010}$	0.264
1.0	9.40	$0.262^{+0.005+0.130}_{-0.005-0.009}$	0.264
1.2	2.65	$0.242^{+0.005+0.119}_{-0.004-0.009}$	0.244
1.4	0.840	$0.242^{+0.005+0.127}_{-0.005-0.009}$	0.242
1.6	0.288	$0.231^{+0.005+0.120}_{-0.004-0.009}$	0.232
1.8	0.105	$0.234^{+0.004+0.115}_{-0.004-0.008}$	0.238
2.0	0.040	$0.233^{+0.005+0.114}_{-0.004-0.008}$	0.235
2.2	0.016	$0.235^{+0.005+0.124}_{-0.004-0.009}$	0.237
2.4	0.006	$0.238^{+0.005+0.122}_{-0.004-0.009}$	0.237
2.6	0.003	$0.227^{+0.005+0.121}_{-0.004-0.008}$	0.224

Table 8.2.: Results of the cross section limit computation for each mass point, showing the expected limit (95 % C.L.) with uncertainties, the observed limit (95 % C.L.) and the theoretical cross section for $\Lambda = M_{\mu^*}$.

$$p_0 \cdot e^{-0.5 \cdot \left(\frac{x-p_1}{p_2}\right)^2} + p_3 \qquad (8.7)$$

leading to a $\chi^2/ndof \approx 0.2$ where ndof is the number of degrees of freedom. The event number can afterwards be scaled to other Λ values. To estimate the systematic uncertainties of the new signal events, similar fits have been performed by shifting the mass points up and down according to the systematic uncertainties (Sec. 7.4). This is indicated by the black lines in Fig. 8.2. For the fitted mass points, new cross section limits have been computed. Tab. A.7 and Tab. A.8 in Appendix A.3 summarize the results from the limit computation of the mass points from the fit. Due to the finer step size between the search windows, the limit does also contain one mass point with two expected events. In this case, a two sigma deviation between the expected and the observed limit can be seen. Now, these cross section limits can be interpreted using the excited muon cross section.
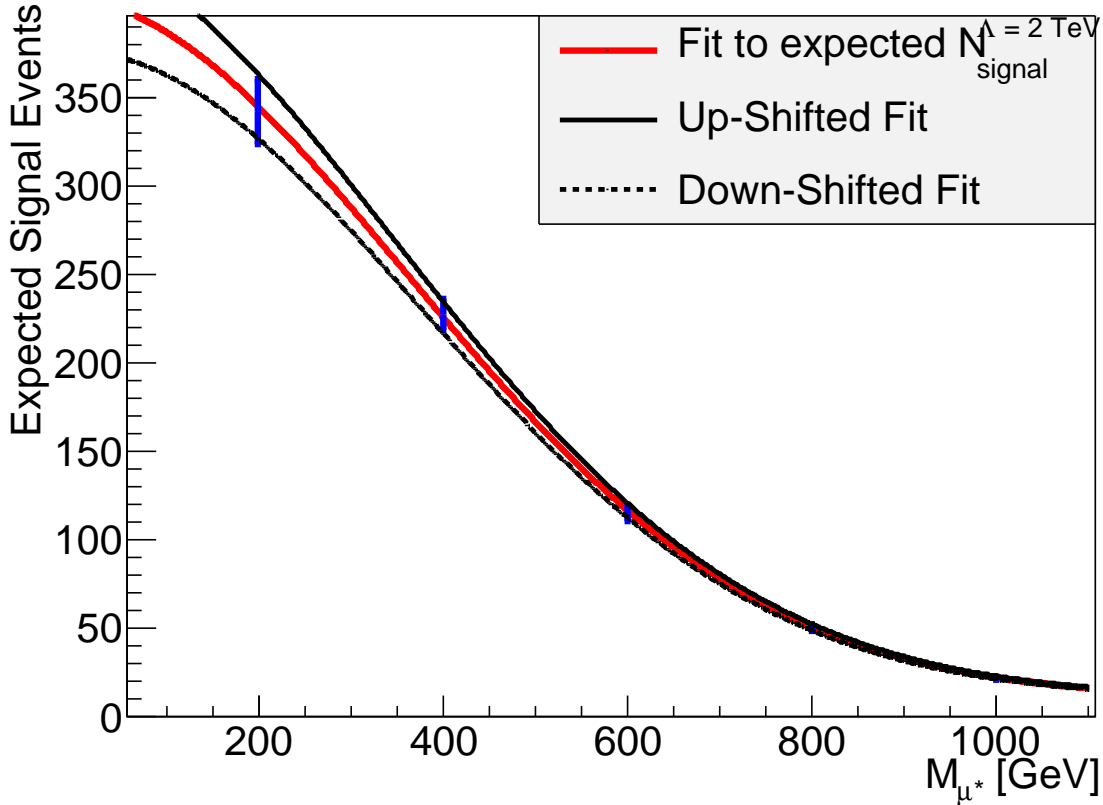
Figure 8.2.: Fit of the expected number of signal events for $\Lambda = 2$ TeV. The numbers at other Λ values are calculated according to Chap. 3.

8.3. M_{μ^*} and Λ limits for $f = f' = 1$

To calculate the limit on the excited muon mass, the cross section of the theory has to be compared with the calculated cross section limit for each mass point. This will be done first for the case $f = f' = 1$ which is the standard way to search for excited objects. The other interesting case ($f = -f' = -1$) where the coupling to the photon vanishes will be discussed later. In contrast to other theories, it is not possible to calculate a simple limit on the excited muon mass since the theory cross section is highly depending on the compositeness scale Λ. This leads to the fact that the excited muon mass can only be excluded for a certain Λ value and that it is possible to give a lower limit on the compositeness scale depending on M_{μ^*}. A natural exclusion limit is given for $\Lambda = M_{\mu^*}$ since the compositeness scale has to be larger than the excited muon mass. This scenario ends up in the highest possible exclusion limit for the excited muon production. Therefore, the limit on the excited muon mass for $\Lambda = M_{\mu^*}$ is the one mostly used for citations in the literature.

μ^*
Fig. 8.3 shows the cross section limit plot including the expected limit (black dashed line) with one σ (green) and two σ (yellow) uncertainty band, the observed limit (blue solid line) and the theoretical cross section of the channel $\mu\mu^* \rightarrow \mu\mu Z \rightarrow 4\mu$ for different Λ values (black solid lines). The masses below the intersection point of a signal cross section line and the expected or
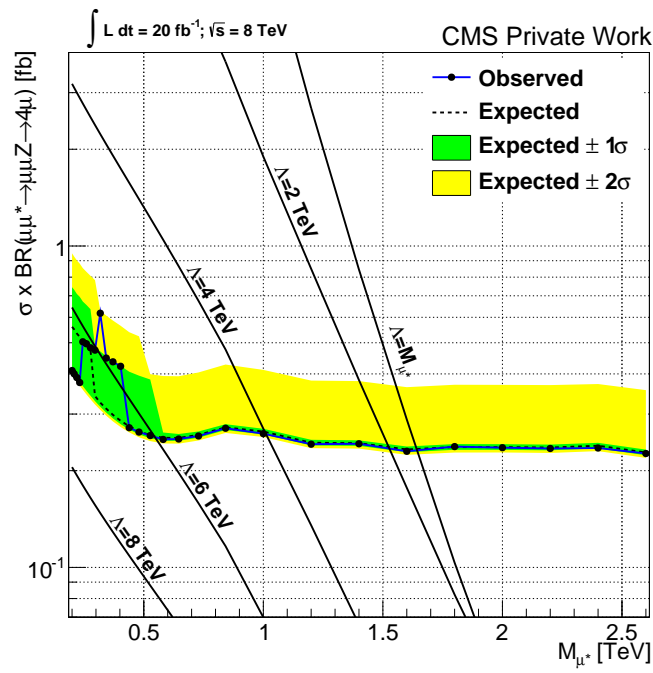
Figure 8.3.: Cross section limit for $\mu\mu^* \to \mu\mu Z \to 4\mu$ as a function of the excited muon mass for $f = f' = 1$.

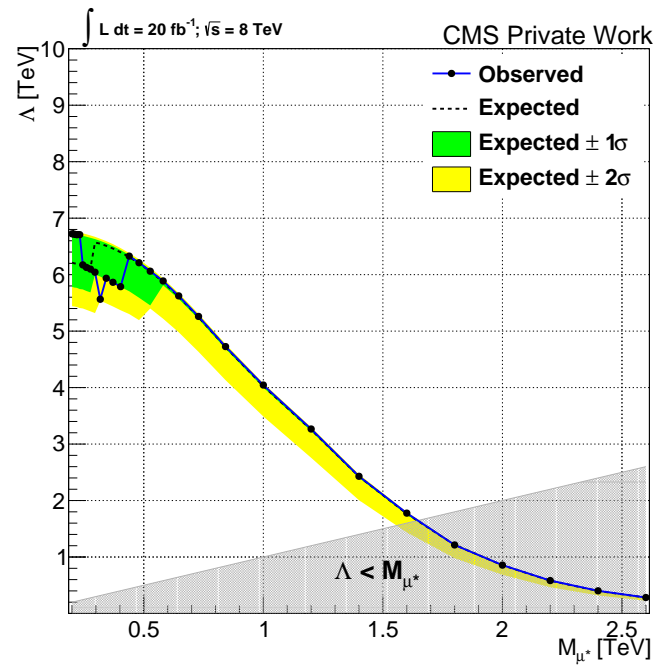Figure 8.4.: Limit on the compositeness scale Λ for $\mu\mu^* \to \mu\mu Z \to 4\mu$ as a function of the excited muon mass for $f = f' = 1$.

observed limit line is excluded at 95 % confidence level. The limit plot shows that the exclusion limit for excited muon production can be set to

$$M_{\mu^*} > 1.64 \text{ TeV} \qquad \text{for} \qquad \Lambda = M_{\mu^*} \qquad @ \text{ 95 \% C.L.} \qquad (8.8)$$

As far as known, this is the first limit on the production of excited muons in the four muon channel. This result matches the expectation that the limit on the excited muon production for this channel is lower than the old limits for the channel $\mu\mu^* \to \mu\mu\gamma$ due to the lower signal cross section (see Sec. 3.3). As discussed before, the limit on the mass depends on the selected Λ value. For example at $\Lambda = 4$ TeV it is given by

$$M_{\mu^*} > 1.00 \text{ TeV} \qquad \text{for} \qquad \Lambda = 4 \text{ TeV} \qquad @ \text{ 95 \% C.L.} \qquad (8.9)$$

In addition to the limit on the mass, a limit on Λ for each mass has to be calculated. A low mass μ^*-production for example is still possible if the compositeness scale has a very large value. The limit on Λ has been computed using the cross section limits depending on the formulas discussed in Sec. 3. Fig. 8.4 shows the limit on the compositeness scale Λ. The highest value is given for $M_{\mu^*} = 200$ GeV where Λ can be excluded for

$$\Lambda > 6.7 \text{ TeV} \qquad \text{for} \qquad M_{\mu^*} = 200 \text{ GeV} \qquad @ \text{ 95 \% C.L.} \qquad (8.10)$$

To estimate the influence of the systematic uncertainties from Sec. 7.4 on the cross section limit, an additional expected limit has been calculated without including them (see Appendix A.5). The expected limit without systematic uncertainties looks similar to the expected limit from Fig. 8.3, there is no visible difference between them. Due to the low background expectation, the limit is completely dominated by the statistic uncertainties. Therefore, the effect of the systematic uncertainties on the final result is negligible in this analysis. Nevertheless, they have been included.

8.4. M_{μ^*} and Λ limits for $f = -f' = -1$

In addition to the scenario $f = f' = 1$ it makes sense to have a look at the limits for $f = -f' = -1$. In this case, the decay of excited muons via photon radiation is not possible and the branching ratio for $\mu\mu^* \to \mu\mu Z \to 4\mu$ is slightly higher. This results in a higher production cross section for the investigated process. The cross section limit which was calculated for the standard case can be used for a reinterpretation as long as the signal efficiency stays the same within the uncertainties. Since the decay kinematics should be consistent with the setting $f = f' = 1$, this can be expected. Fig. 8.5 and Fig. 8.6 present the cross section limit and the limit on Λ for this reinterpretation. As a result of the higher signal cross section, the observed and expected limits for this case are slightly higher. The observed limit for $\Lambda = M_{\mu^*}$ can be set to

$$M_{\mu^*} > 1.89 \text{ TeV} \qquad \text{for} \qquad \Lambda = M_{\mu^*} \qquad @ \text{ 95 \% C.L.} \qquad (8.11)$$
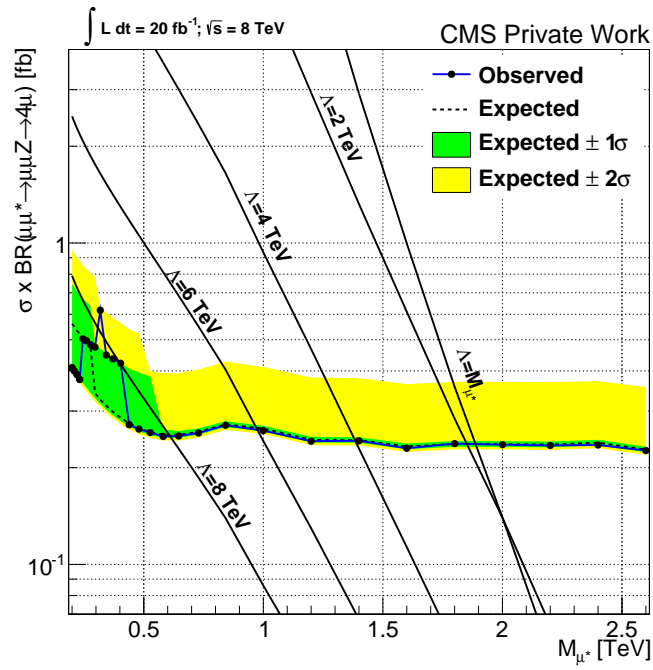
Figure 8.5.: Cross section limit for $\mu\mu^* \to \mu\mu Z \to 4\mu$ as a function of the excited muon mass for $f = -f' = -1$.
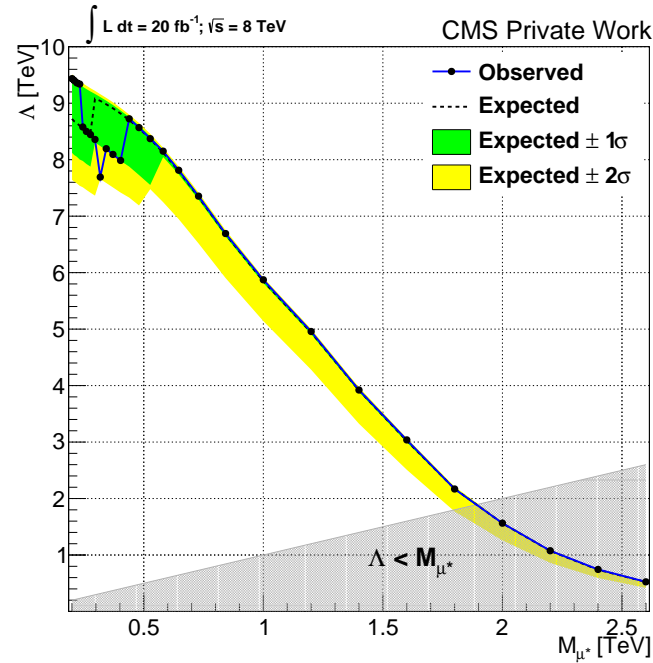

Figure 8.6.: Limit on the compositeness scale Λ for $\mu\mu^* \to \mu\mu Z \to 4\mu$ as a function of the excited muon mass for $f = -f' = -1$.

This limit is comparable to the results from ATLAS and CMS for the channel $\mu\mu^* \to \mu\mu\gamma$ at $\sqrt{s} = 7$ TeV with $\mathscr{L}_{int} = 5$ fb^{-1} of collected data. The best limit on the compositeness scale is given by

$$\mathbf{\Lambda > 9.4 \; TeV} \qquad \mathbf{for} \qquad \mathbf{M_{\mu^*} = 200 \; GeV} \qquad \mathbf{@ \; 95 \; \% \; C.L.} \tag{8.12}$$

which is a much higher value in comparison to the setting $f = f' = 1$.

8.5. Contribution from the Contact Interaction Decay

As mentioned before, the decay via contact interaction can also lead to a four muon final state, but it is not included here due to a missing signal. This decay would have a positive influence on the signal strength and because of that also on the sensitivity of the analysis. Therefore, a short estimation of the contribution of the CI decay to four muons will be given here based on the expected kinematics.
According to the theory, the branching ratio of the CI-decay is 92 % and the ratio of the Z-boson radiation is only 0.9 % for $\Lambda = M_{\mu^*}$. For contact interaction, the ratio of the decay to three muons is $\frac{2}{25} = 8$ % and for the Z-boson, it is 3.3 %. This means that the decay via CI to four muons is expected to happen about $\frac{0.92 \cdot 0.08}{0.009 \cdot 0.033} \approx 250$ times more often than the decay via Z-boson radiation. Not included here is the contribution from τ decays. The efficiency of the acceptance cuts of the CI decay should be comparable to the Z decay. This should also be the case for the muon selection criteria since the modified muon ID has no negative influence on the efficiency of standard muons. Small differences in the efficiency can arise from the two invariant mass cuts. In case of the CI decay, no Z-boson is part of the signal. For an independent analysis of the CI decay, this fact would give the possibility to discriminate against the complete ZZ background since two Z vetos can be applied. At this point of the analysis, no selection step should have a negative impact on the signal efficiency of the CI decay, meaning that it can expected to be close to the Z-channel efficiency.
The only selection that that can discriminate against the CI contribution is the L-shape cut because there is no way to distinguish the four muons from the CI decay. Nevertheless, it can be expected that still a huge contribution remains after this cut. If the ratio of the efficiencies $\frac{\epsilon_{CI}}{\epsilon_Z}$ is larger than 4 %, the expected number of events from the CI decay is more than ten times higher compared to the Z decay. For the case $\epsilon_{CI} = \epsilon_Z$, the factor is about 250. According to Tab. 8.1, a mass point can be excluded if about four events are expected while there is nearly no background expectation. This means that for $\epsilon_{CI} = 0.04 \cdot \epsilon_Z$ the 2 TeV mass point could be excluded and for $\epsilon_{CI} = \epsilon_Z$ masses up to 2.6 TeV for $\Lambda = M_{\mu^*}$.

8.6. Combination with $\mu\mu^* \to \mu\mu Z \to 2\mu2e$

A similar analysis has been performed by Shu-Hao Mai from the Central National University in Taiwan in the $\mu\mu^* \to \mu\mu Z \to 2\mu2e$ channel where the Z-boson decays to two electrons [66]. The analysis strategy is comparable to the 4μ-channel, the selection is also dominated by the decay of boosted Z-bosons. Here, the muon-photon dataset with the $HLT\_Mu22\_Photon22$ trigger has been used. The choice of the trigger is driven by an inefficiency of the muon-electron trigger due to an isolation requirement for the electrons which is not included in the muon-photon trigger. In addition, the p_T thresholds are set to 25 GeV instead of 20 GeV for all for leptons. For the selection of the muons, the standard high-p_T muon ID is used while for the electrons, the HEEP

ID [84] is applied with small modifications according to [85]. In contrast to the decay to muons, an inefficiency in the selection is only caused by the isolation and not by the ID criteria, but an additional effect takes place in the electron channel: If the ΔR between two electron is too small, they are merged together in the ECAL. As a results, some events do only contain one electron instead of two and therefore, the efficiency slightly decreases for very high masses. This effect decreases the efficiency by about 5 %. Since the HEEP ID is 5 % less efficient than the high-p_T muon ID per lepton, the full acceptance $\times$ efficiency in the $2\mu2e$ channel is about (15-20) % worse in comparison to the 4μ channel. Therefore, the limits are also worse and excited muons in the channel $\mu\mu^* \to \mu\mu Z \to 2\mu2e$ can only be excluded up to $M_{\mu^*} > 1.60$ TeV for $\Lambda = M_{\mu^*}$. Fig. 8.7 shows the shape of the signal in the $M_{min} - M_{max}$ plane for the electron channel (left) and the L-shape cut for $M_{\mu^*} = 600$ GeV on the right side. Here, only one data event is left after applying the full selection. Since this event has a maximum invariant mass below 200 GeV, it does not contribute to the limit calculation.
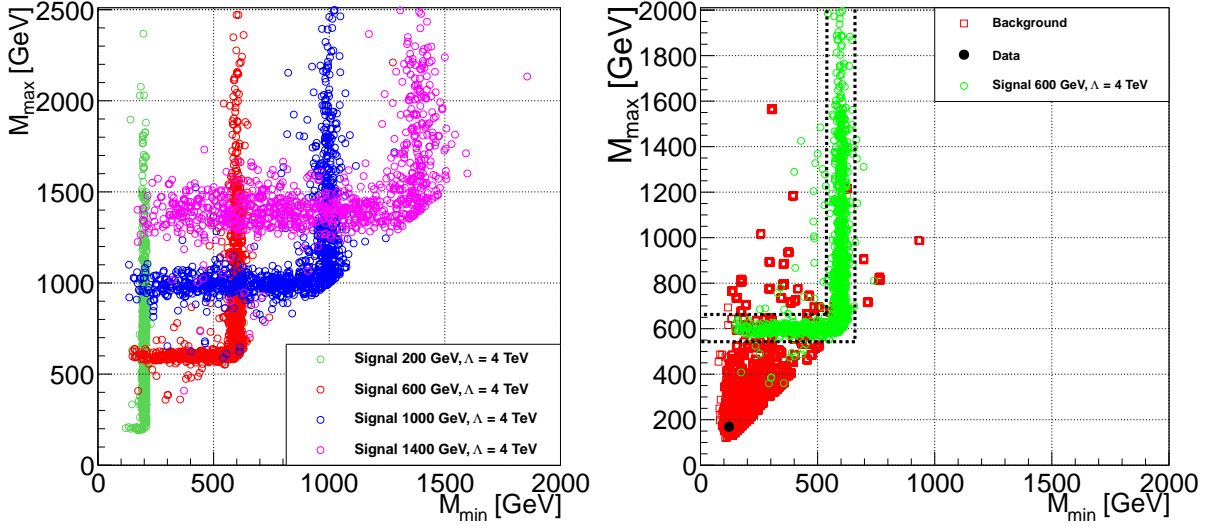

Figure 8.7.: Left: Shape of the $2\mu2e$ signal in the $M_{min} - M_{max}$ plane after applying the full selection. Right: L-shape cut for $M_{\mu^*} = 600$ GeV.

The results of the two channels are combined using the Higgs Combined Tool [82], taking the systematic uncertainties of both channels into account. It is expected that both channels have the same cross section and therefore, the signal cross section for $\mu\mu^* \to \mu\mu Z \to 2\mu2l$ $(l = e, \mu)$ is two times higher per mass point compared to Tab. 8.2. The results of the combined limit computation are shown in Fig. 8.8. The observed as well as the expected exclusion limit for the production of excited muons can be set to

$$M_{\mu^*} > 1.75 \text{ TeV} \qquad \text{for} \qquad \Lambda = M_{\mu^*} \qquad @ \ 95 \ \% \ \text{C.L.} \tag{8.13}$$

Here, it is expected that $f = f' = 1$. By combining the two channels, the limit can be extended by about 0.1 TeV. The combined limit on the compositeness scale Λ is given by

$$\Lambda > 7.6 \text{ TeV} \qquad \text{for} \qquad M_{\mu^*} = 200 \text{ GeV} \qquad @ \ 95 \ \% \ \text{C.L.} \tag{8.14}$$
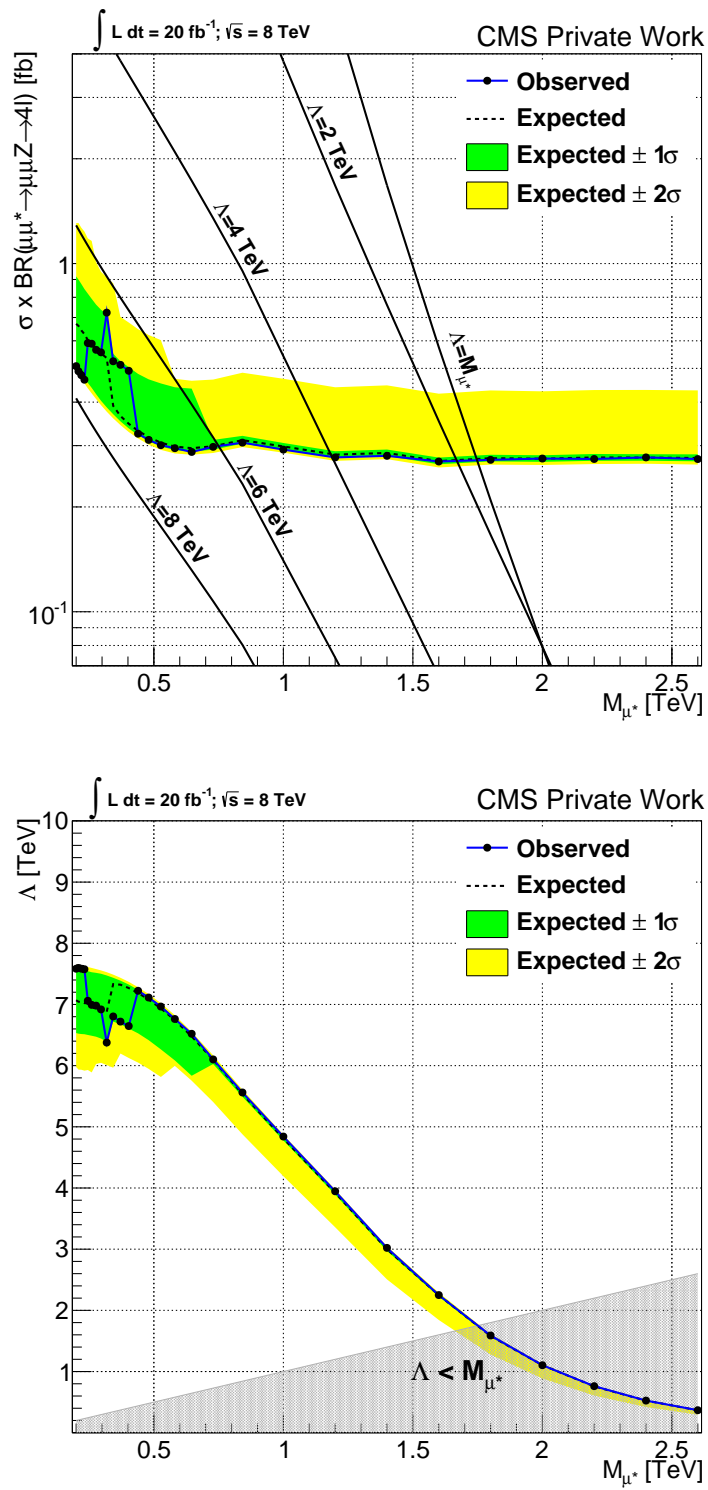
Figure 8.8.: Combined Limit for $\mu\mu^* \rightarrow \mu\mu Z \rightarrow 2\mu 2l$ ($l = e, \mu$) as a function of the excited muon mass for $f = f' = 1$. Top: Cross section limit; bottom: Limit on the compositeness scale Λ.

which is about 0.9 TeV higher than without the combination. Tab. 8.3 summarizes the results
of the combined limit calculation for each mass point (without the points from the fit).

$M_{\mu*}$ (TeV)	$\sigma_{\text{theory}}^{\Lambda=M_{\mu*}}$ (fb)	Exp. Limit (fb)	Obs. Limit (fb)
0.2	73463	0.792	0.586
0.4	3426	0.413	0.609
0.6	413	0.338	0.333
0.8	77.7	0.314	0.308
1.0	18.8	0.306	0.306
1.2	5.29	0.290	0.289
1.4	1.68	0.293	0.293
1.6	0.575	0.273	0.271
1.8	0.209	0.281	0.277
2.0	0.079	0.279	0.278
2.2	0.031	0.281	0.280
2.4	0.012	0.282	0.279
2.6	0.005	0.280	0.278

Table 8.3.: Results of the combined cross section limit computation for each mass point, showing
the expected limit, the observed limit (95 % C.L.) and the theoretical cross section
for $\Lambda = M_{\mu*}$.

9. Conclusion and Outlook

This thesis has presented the search for excited muons in the decay channel $\mu\mu^* \to \mu\mu Z \to 4\mu$ with data from the CMS experiment at the LHC. The data was recorded in the year 2012 at a center-of-mass energy of $\sqrt{s} = 8$ TeV and corresponds to an integrated luminosity of $\mathscr{L}_{int} = (19.7 \pm 0.5)\,\mathrm{fb}^{-1}$. This is the first time that a search for excited muons was performed in the four muon final state. Although the branching ratio of this decay channel is expected to be much smaller, it is an important addition to the standard search channel $\mu\mu\gamma$.

The target of the analysis was an optimization of the signal to background ratio. Since the final state muons have a very high transverse momentum for a high mass signal, the high-p_T muon identification criteria have been applied. It has been shown that the signal efficiency suffers from the decay of highly boosted Z bosons to a nearby dimuon pair for increasing μ^*-masses due to a problem with the global muon reconstruction. A solution for this problem has been presented by changing the ID for one muon from the boosted Z decay. In addition to this, the isolation of both muons has been modified by removing the contribution of the other muon. These two changes lead to a flat efficiency for increasing μ^*-masses. The comparison of data with respect to the Standard Model background expectation shows no deviation, 43 events have been observed while 48.8 ± 0.3 (stat.) ± 7.5 (syst.) events are expected.

In addition to the ID selection, two invariant mass cuts on the two dimuon pairs have been adopted to reduce the dominant ZZ background. The muon pair from the Z decay should have an invariant mass larger than 60 GeV and the other pair beyond 106 GeV. The latter cut drastically discriminates the ZZ background without influencing the signal very much. After these cut, 5 events with respect to 4.7 ± 0.1 (stat.) ± 0.7 (syst.) expected events are observed. Since there has been no evidence for excited muons, a cross section limit has been set on the excited muon production in dependence of the compositeness scale Λ. For this purpose, the signal to background ratio has been improved by putting a final selection cut within the two-dimensional minimum-maximum invariant mass plane. Tab. 9.1 summarizes the limits on the excited muon mass for different Λ values for f = f' = 1.

Λ (TeV)	Exp. Limit (GeV)	Obs. Limit (GeV)
2	1.52	1.52
4	1.00	1.00
6	0.54	0.30 and 0.42-0.54
$\Lambda = M_{\mu^*}$	1.64	1.64

Table 9.1.: Summary of limits on the excited muon mass for different Λ values with the scenario $f = f' = 1$ at 95 % C.L.

Since there is the possibility of the existence of excited muons without a decay via photon radiation for the scenario $f = -f' = -1$, the cross section limit has been reinterpreted for this case. The results of the reinterpretation are shown in Tab. 9.2.
In addition to the limits for the 4μ channel, a combination with the $2\mu2e$ channel where the

Λ (TeV)	Exp. Limit (TeV)	Obs. Limit (TeV)
2	1.85	1.85
4	1.38	1.38
6	0.97	0.97
8	0.60	0.31 and 0.33-0.53
$\Lambda = M_{\mu^*}$	1.89	1.89

Table 9.2.: Summary of limits on the excited muon mass for different Λ values with the scenario $f = -f' = -1$ at 95 % C.L.

Z-boson decays to two electrons has been performed for $f = f' = 1$. The cross section limits for the combination are summarized in Tab. 9.3.

Λ (TeV)	Exp. Limit (TeV)	Obs. Limit (TeV)
2	1.67	1.67
4	1.17	1.17
6	0.73	0.74
$\Lambda = M_{\mu^*}$	1.75	1.75

Table 9.3.: Summary of the combined limits for $\mu\mu^* \to \mu\mu Z \to 2\mu 2l$ for different Λ values with the scenario $f = f' = 1$ at 95 % C.L.

A similar analysis is also performed in the channel $\mu\mu^* \to \mu\mu Z \to 2\mu 2j$ by other analysers. A combination of all three channels and maybe with the $\mu\mu\gamma$ channel is one of the future targets for this analysis with 2012 data. In addition, it is also interesting to produce a contact interaction signal with a decay to four leptons which would be the next step for this analysis. A new analysis can also be very interesting when the LHC starts its work after the upgrade to $\sqrt{s} = 13$ TeV with a higher luminosity. The possibility to discriminate the background by conserving a high signal efficiency would result in an even better signal to background ratio for a higher amount of data. In any case, it is helpful to have an additional channel in comparison to the $\mu\mu\gamma$ channel since the theory allows the appearance of excited muons without photon radiation. For this purpose, the four lepton final state is much more suitable than the decay via W-boson radiation since it has no missing transverse energy.

A. Appendix

A.1. List of Events after ID and Isolation

Please turn the page.

Run	Lumi Section	Event	M_{min} (GeV)	M_{max} (GeV)
190895	839	836690441	243.514	299.778
191226	508	714036395	149.586	158.625
194704	415	372667387	140.042	177.868
194897	81	146471772	103.31	180.193
194912	899	1347277781	125.225	257.827
195147	419	502821363	143.125	179.494
195251	80	147388276	150.477	151.326
195378	616	761725481	230.801	266.51
195774	90	174957822	126.475	159.123
195774	387	660605607	494.116	554.718
195950	667	630954116	116.204	147.475
195950	781	719208626	123.63	145.095
196197	238	352383455	283.322	469.343
196239	766	687711552	210.199	392.82
198230	872	787588132	289.991	847.436
198272	382	345644314	124.278	137.602
198487	1522	1511453808	147.362	408.87
198955	493	575302642	121.225	145.657
198969	937	1103535297	313.982	338.905
199021	1083	1238510739	160.278	225.631
199409	303	402443918	134.881	160.086
199428	548	654887173	139.69	143.923
199752	104	133641846	155.384	175.134
199876	258	299199538	166.583	328.831
199876	290	331969560	167.953	176.468
200600	1019	1248257881	121.641	164.521
200992	324	279759749	119.661	159.486
201191	156	199183870	125.891	207.525
201611	163	159726794	130.759	131.095
201668	121	114003150	113.79	142.858
202178	448	563981267	130.943	148.48
204564	580	637834076	116.22	177.138
205781	458	617795227	133.618	147.246
205834	49	70540430	111.315	184.404
206401	87	69962177	129.377	182.439
206477	182	276785714	124.901	171.739
206512	393	522300157	258.973	267.914
206594	225	322510503	109.113	262.916
206745	1477	1407561357	299.096	374.739
206859	271	395759900	129.17	182.759
207231	999	1344760175	126.32	243.523
207269	501	673638714	228.799	261.14
207515	503	792210029	131.119	137.862

Table A.1.: List of the 43 events left after applying ID and isolation criteria. The green event is the one with the highest M_{max}, the red events are the five that survive the invariant mass cuts.

A.2. Event Displays

Run: 206745, Lumi Section: 1477, Event: 1407561357
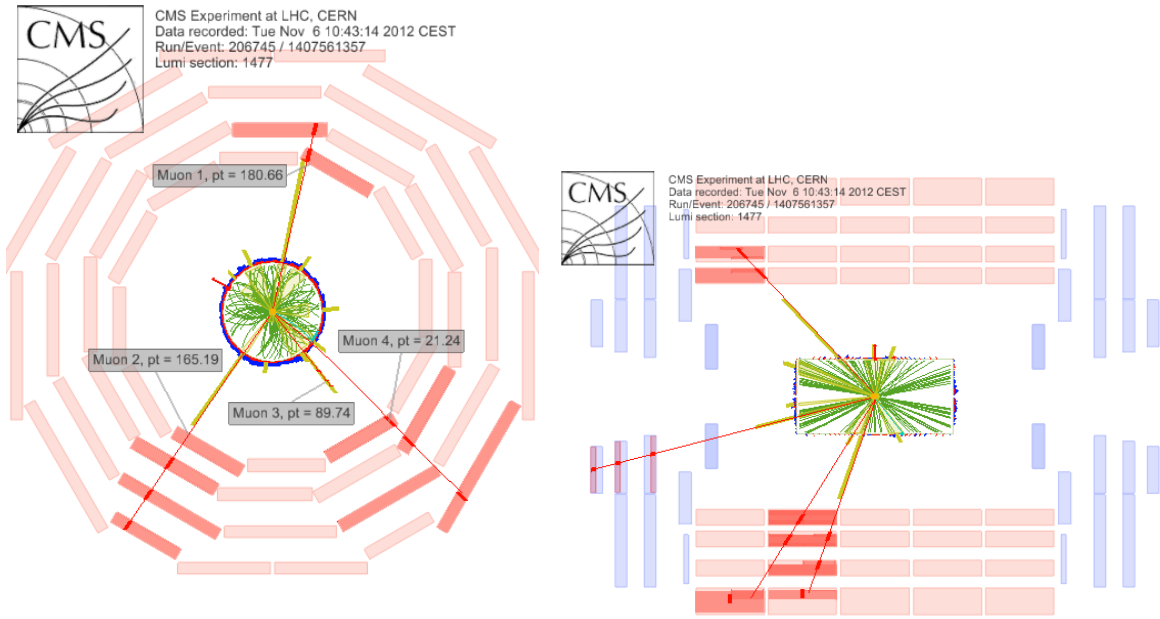
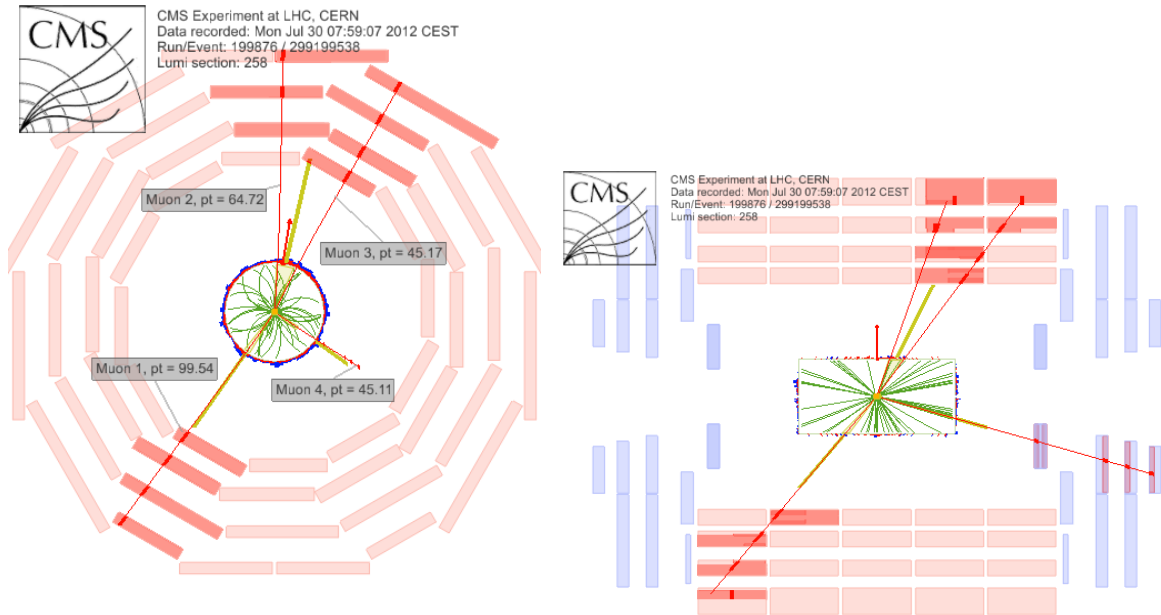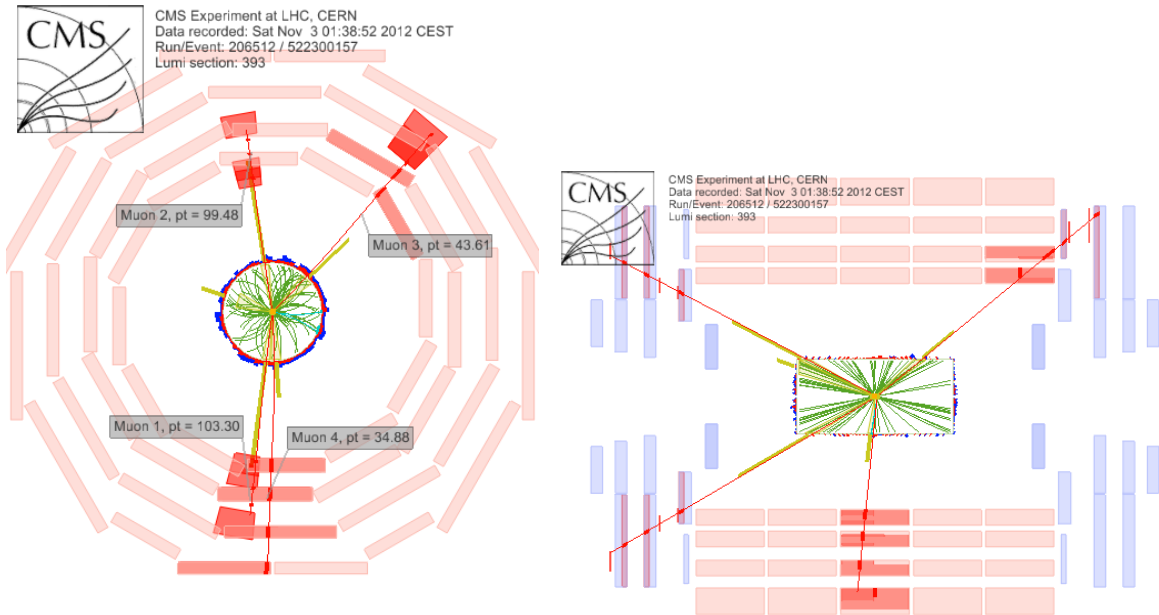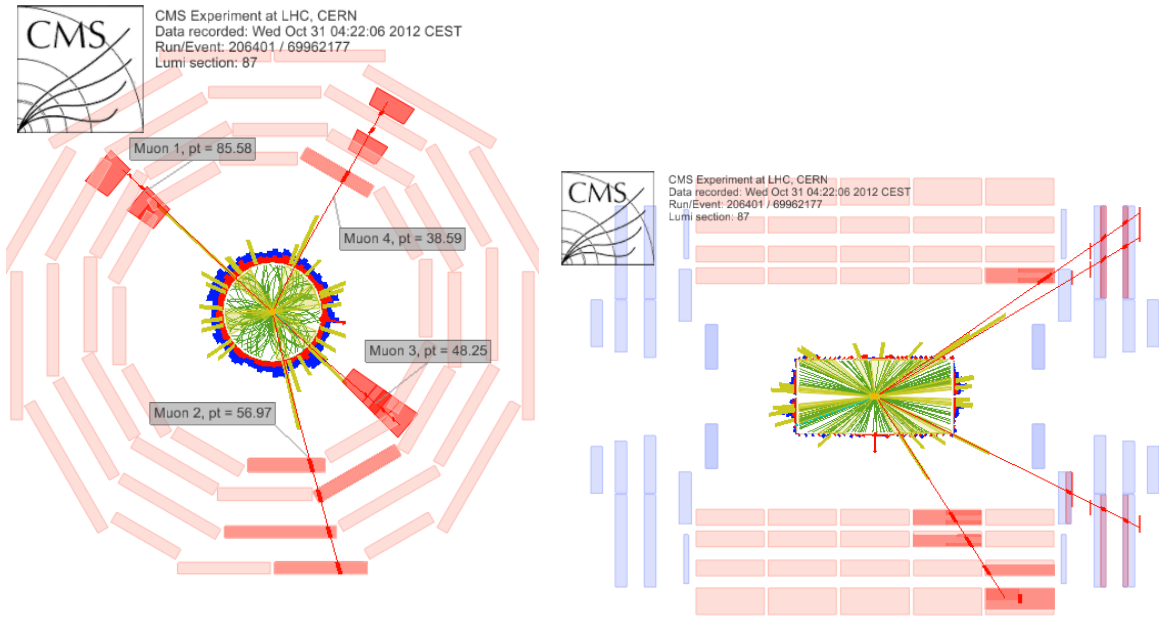

Figure A.1.: Event display of the highest maximum invariant mass event. Left: $\rho{-}\phi$ view; Right: $\rho - z$ view.

M_{min} (GeV)	299.1		
M_{max} (GeV)	374.7		
Object	p_T (GeV)	η	ϕ
Muon 1	180.7	-0.84	1.36
Muon 2	165.2	-0.34	-2.18
Muon 3	89.7	-2.07	-0.91
Muon 4	21.2	-0.59	-0.63

Table A.2.: Summary of the characteristics of the lowest invariant mass event. The muons are ordered by their transverse momentum, beginning with the highest one.

Run: 199876, Lumi Section: 258, Event: 299199538


Figure A.2.: Event display of the second highest maximum invariant mass event. Left: $\rho - \phi$
view; Right: $\rho - z$ view.

M_{min} (GeV)	166.6		
M_{max} (GeV)	328.8		
Object	p_T (GeV)	η	ϕ
Muon 1	99.5	-0.77	-2.17
Muon 2	64.7	0.35	1.49
Muon 3	45.2	0.69	1.13
Muon 4	45.1	1.98	-0.60

Table A.3.: Summary of the characteristics of the second highest invariant mass event. The
muons are ordered by their transverse momentum, beginning with the highest one.

Run: 206512, Lumi Section: 393, Event: 522300157

Figure A.3.: Event display of the third highest maximum invariant mass event. Left: $\rho - \phi$ view; Right: $\rho - z$ view.

M_{min} (GeV)	259.0		
M_{max} (GeV)	267.9		
Object	p_T (GeV)	η	ϕ
Muon 1	103.3	-1.31	-1.70
Muon 2	99.5	-1.40	1.73
Muon 3	43.6	1.02	0.78
Muon 4	34.9	-0.10	-1.51

Table A.4.: Summary of the characteristics of the third highest invariant mass event. The muons are ordered by their transverse momentum, beginning with the highest one.

Run: 206401, Lumi Section: 87, Event: 69962177

Figure A.4.: Event display of the second lowest maximum invariant mass event. Left: $\rho - \phi$ view; Right: $\rho - z$ view.

M_{min} (GeV)	129.4		
M_{max} (GeV)	182.4		
Object	p_T (GeV)	η	ϕ
Muon 1	85.6	1.28	2.41
Muon 2	57.0	0.60	-1.36
Muon 3	48.3	1.45	-0.76
Muon 4	38.6	1.16	1.13

Table A.5.: Summary of the characteristics of the second lowest invariant mass event. The muons are ordered by their transverse momentum, beginning with the highest one.

Run: 206477, Lumi Section: 182, Event: 276785714
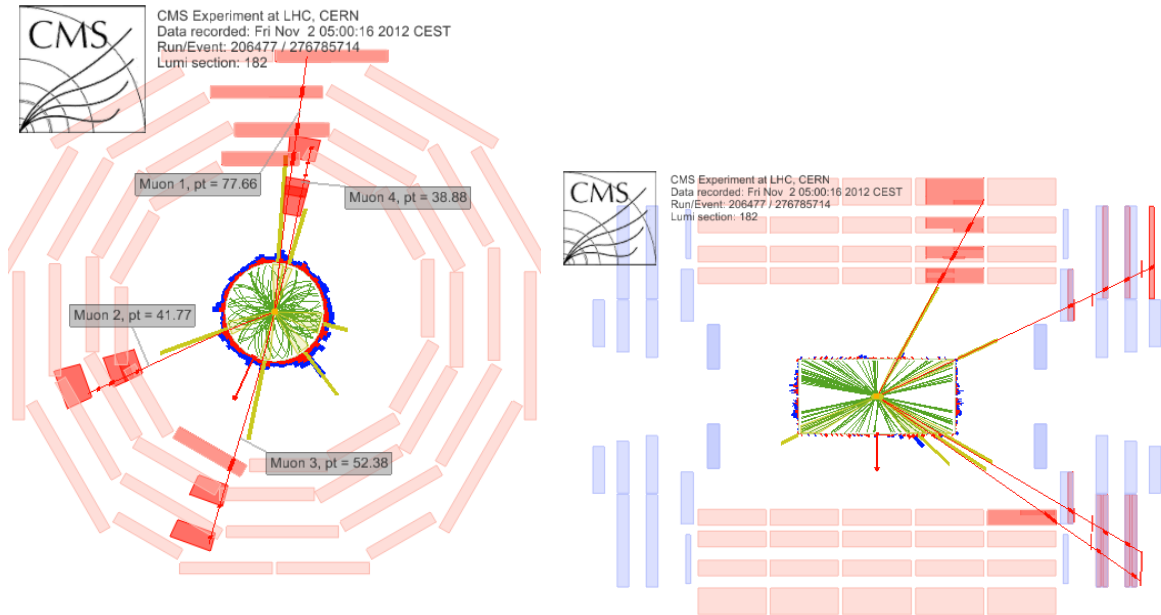
Figure A.5.: Event display of the lowest invariant mass event. Left: $\rho - \phi$ view; Right: $\rho - z$ view.

M_{min} (GeV)	124.9		
M_{max} (GeV)	171.7		
Object	p_T (GeV)	η	ϕ
Muon 1	77.7	0.52	1.48
Muon 2	52.4	1.15	-1.80
Muon 3	41.8	1.30	-2.78
Muon 4	38.9	1.50	1.30

Table A.6.: Summary of the characteristics of the lowest invariant mass event. The muons are ordered by their transverse momentum, beginning with the highest one.

A.3. Results from the Window Fit

M_{μ^*} (GeV)	Cut Range (GeV)	N_{data} (Events)	N_{bkg} (Events)	$N_{\text{signal}}^{\Lambda=M_{\mu^*}}$ (Events)
209	198-220	0	0.91 ± 0.15	212475
220	207-233	0	0.94 ± 0.16	178705
232	218-246	0	0.88 ± 0.15	145143
245	230-260	1	0.91 ± 0.15	118557
260	243-277	1	0.83 ± 0.14	93757
277	258-296	1	0.75 ± 0.13	72915
296	275-317	1	0.62 ± 0.11	55907
318	295-341	2	0.50 ± 0.09	41589
343	317-369	1	0.43 ± 0.07	30453
371	342-400	1	0.35 ± 0.06	21798
403	370-436	1	0.30 ± 0.05	15225
439	395-483	0	0.30 ± 0.05	10407
480	424-536	0	0.25 ± 0.04	6903
527	458-596	0	0.19 ± 0.03	4415
581	496-666	0	0.15 ± 0.03	2705
646	539-753	0	0.12 ± 0.02	1539
729	593-865	0	0.09 ± 0.02	773
842	673-1011	0	0.06 ± 0.01	318

Table A.7.: Summary of the L-shape cut results, showing the cut ranges and the selected number of data, background and signal events for all invariant mass points.

M_{μ^*} (GeV)	$\sigma_{\text{theory}}^{\Lambda=M_{\mu^*}}$ (fb)	Exp. Limit $\pm 1\sigma \pm 2\sigma$ (fb)	Obs. Limit (fb)
209	28611	$0.550^{+0.184+0.389}_{-0.152-0.164}$	0.400
220	22983	$0.534^{+0.175+0.368}_{-0.146-0.156}$	0.390
232	18261	$0.522^{+0.173+0.360}_{-0.144-0.154}$	0.376
245	14375	$0.505^{+0.166+0.348}_{-0.139-0.148}$	0.503
260	11038	$0.492^{+0.164+0.339}_{-0.137-0.146}$	0.496
277	8289	$0.476^{0.160+0.332}_{-0.133-0.142}$	0.482
296	6130	$0.341^{+0.145+0.442}_{-0.012-0.020}$	0.474
318	4400	$0.325^{+0.144+0.304}_{-0.009-0.016}$	0.618
343	3087	$0.312^{+0.142+0.296}_{-0.009-0.015}$	0.448
371	2126	$0.298^{+0.141+0.288}_{-0.007-0.014}$	0.435
403	1427	$0.286^{+0.138+0.279}_{-0.007-0.013}$	0.422
439	939	$0.275^{+0.132+0.265}_{-0.006-0.012}$	0.272
480	602	$0.265^{+0.130+0.258}_{-0.006-0.011}$	0.264
527	375	$0.258^{+0.127+0.142}_{-0.006-0.012}$	0.257
581	226	$0.253^{+0.010+0.141}_{-0.005-0.010}$	0.250
646	128	$0.253^{+0.007+0.141}_{-0.005-0.010}$	0.251
729	66.0	$0.258^{+0.006+0.145}_{-0.005-0.010}$	0.256
842	28.7	$0.273^{+0.006+0.155}_{-0.005-0.011}$	0.271

Table A.8.: Results of the cross section limit computation for each mass point from the fit, showing the expected limit with uncertainties, the observed limit and the theory cross section for $\Lambda = M_{\mu^*}$.

A.4. Limit Plots without Search Window Fit

(a) Cross section limit

(b) Limit on the compositeness scale Λ
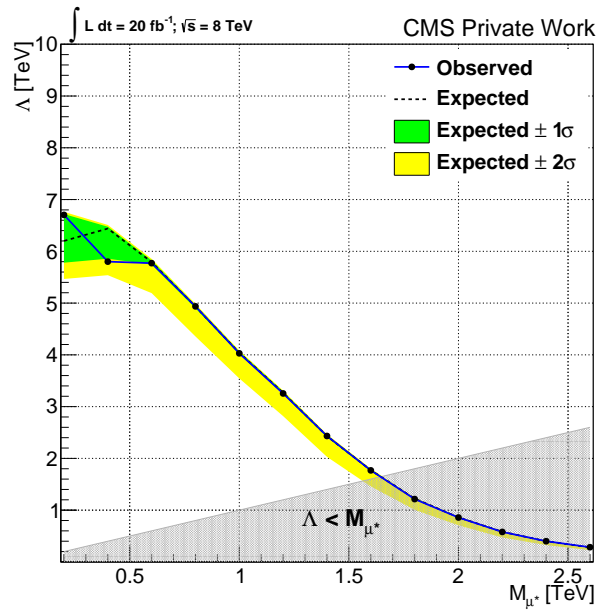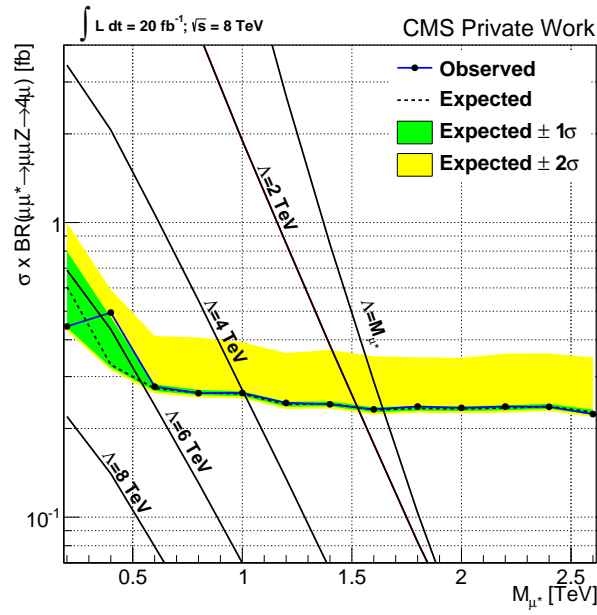
Figure A.6.: Limits on the cross section and the compositeness scale Λ as a function of the excited muon mass for $\mu\mu^* \to \mu\mu Z \to 4\mu$ ($f = f' = 1$) without applying the fit function to the number of expected signal events.
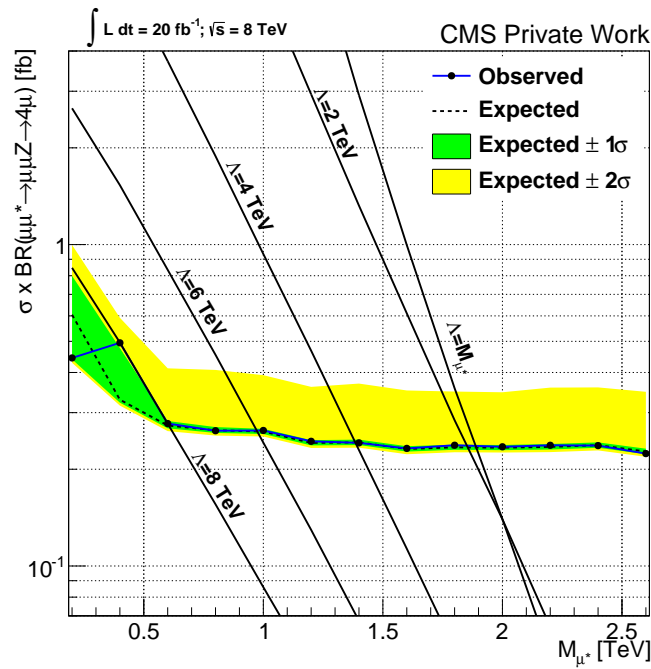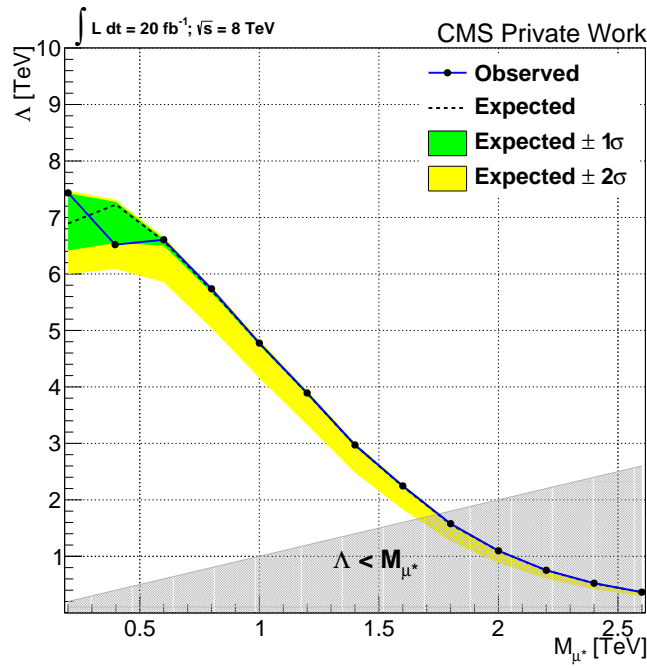
(a) Cross section limit
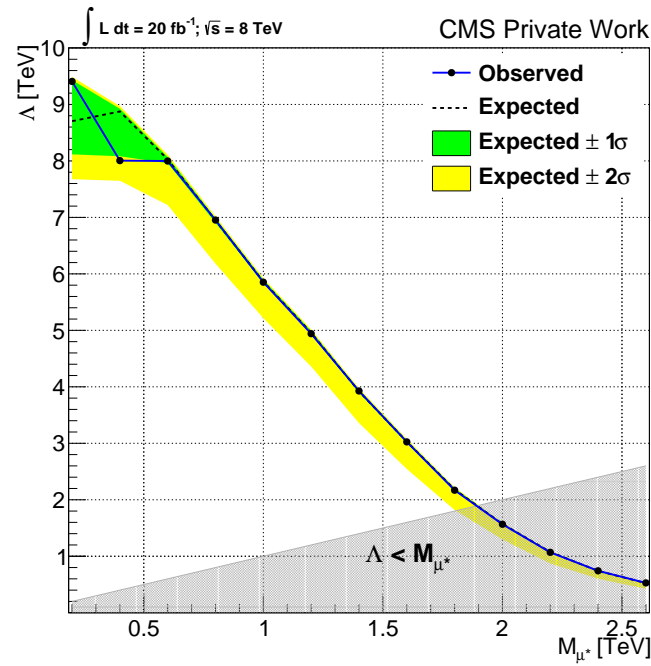
(b) Limit on the compositeness scale Λ

Figure A.7.: Limits on the cross section and the compositeness scale Λ as a function of the excited muon mass for $\mu\mu^* \to \mu\mu Z \to 4\mu$ ($f = -f' = -1$) without applying the fit function to the number of expected signal events.
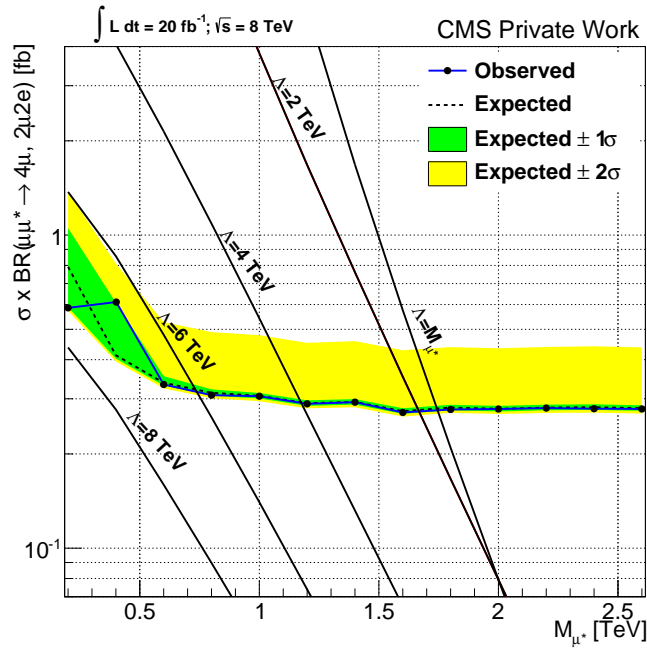
(a) Combined cross section limit

(b) Combined limit on the compositeness scale Λ

Figure A.8.: Combined limits on the cross section and the compositeness scale Λ as a function of the excited muon mass for $\mu\mu^* \to \mu\mu Z \to 2\mu2e$ ($f = f' = 1$) without applying the fit function to the number of expected signal events.

A.5. Effect of the systematic uncertainties on the limit
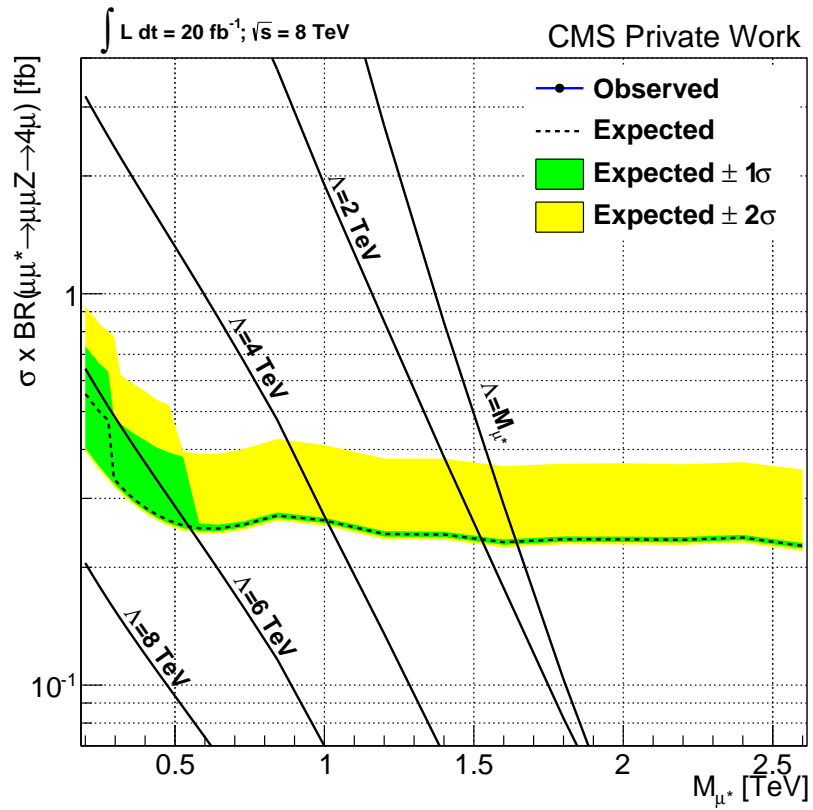
Figure A.9.: Expected cross section limit without applying systematic uncertainties in the limit setting procedure for $(f = f' = 1)$.

Bibliography

[1] D. Griffiths, "Introduction to Elementary Particles". WILEY-VCH Verlag, Weinheim, second edition, 2008.

[2] L. Feld, "Skript zur Vorlesung Elementarteilchenphysik I", RWTH Aachen, WS 2011/2012.

[3] Particle Data Group, "Review of Particle Physics", July, 2012.

[4] The CMS Collaboration, "Observation of a new Boson at a mass of 125 GeV with the CMS experiment at the LHC", 2012. `doi:10.1016/j.physletb.2012.08.021`.

[5] The ATLAS Collaboration, "Observation of a new particle in the search for the Standard Model Higgs boson with the ATLAS detector at the LHC", 2012. `doi:10.1016/j.physletb.2012.08.020`.

[6] The CMS Collaboration, "CMS Higgs Physics Results, TWiki Website". `https://twiki.cern.ch/twiki/bin/view/CMSPublic/PhysicsResultsHIG`, 2013.

[7] The ATLAS Collaboration, "Higgs Public Results, TWiki Website". `https://twiki.cern.ch/twiki/bin/view/AtlasPublic/HiggsPublicResults`, 2013.

[8] "The Nobel Prize in Physics 2013". `http://www.nobelprize.org/nobel_prizes/physics/laureates/2013/`.

[9] L. Alvarez-Gaume and J. Ellis, "Eyes on a Prize Particle", 2011.

[10] U. Baur, M.Spira and P. M. Zerwas, "Excited-quark and -lepton production at hadron colliders", *Physical Review D* **42** (1990), no. 3, p. 815–824. `doi:10.1103/PhysRevD.42.815`.

[11] O. Cakir, C. Leroy, R. Mehdiyev and A. Belyaev, "Prodution and Decay of Excited Electrons at the LHC", *Eur. Phys. J.* **C 42** (2004) , p. 1–17, `arXiv:0212006v2`.

[12] O.J.P. Éboli, S.M. Lietti, and P.Mathews, "Excited Leptons at the CERN Large Hadron Collider", `arXiv:0111001v2`. `doi:10.1103/PhysRevD.65.075003`.

[13] T. N. Trinh and E. Sauvan, "Single Production of Excited Leptons at the LHeC". `http://cds.cern.ch/record/1354237/files/ExcitedFermions.pdf`, 2011.

[14] K. Hagiwara, S. Komamiya and D. Zeppenfeld, "Excited Lepton Production at LEP and HERA", *Z. Phys. C - Particles and Fields* **29** (1985) , p. 115–122. `doi:10.1007/BF01571391`.

[15] Volker Vorwerk, "Search for Excited Electrons with the D0 Experiment at the Tevatron Collider", *Diploma Thesis, RWTH Aachen University, Aachen* (2006).

[16] The ALEPH Collaboration, "Search for excited leptons at 130-140 GeV", *Phys. Lett.* **B 385** (1996) 445–453. `doi:10.1016/0370-2693(96)00961-6`.

[17] The OPAL Collaboration, "Search for Unstable Heavy and Excited Leptons at LEP2", *Eur. Phys. J.* **C 14** (2000) 73–84, `arXiv:0001056`. `doi:10.1007/s100520050734`.

[18] The DELPHI Collaboration, "Search for excited leptons in e$^+$+e$^-$ collisions at $\sqrt{s} =$ 189-209 GeV", *Eur. Phys. J.* **C 46** (2006) 277–293, `arXiv:0603045`. `doi:10.1140/epjc/s2006-02501-3`.

[19] The L3 Collaboration, "Search for Excited Leptons at LEP", *Phys. Lett.* **B 568** (2003) 23–34, `arXiv:03060015`. `doi:10.1016/j.physletb2003.05.004`.

[20] The ZEUS Collaboration, "Searches for excited fermions in ep collisions at HERA", *Phys. Lett.* **B 549** (2002) 32–47, `arXiv:0109018`. `doi:10.1016/S0370-2693(02)02863-0`.

[21] The H1 Collaboration, "Search for Excited Electrons in ep Collisions at HERA", *Phys. Lett.* **B 666** (2008) 131–139, `arXiv:0805.4530`. `doi:10.1016/j.physletb.2008.07.014`.

[22] The CDF Collaboration, "Search for Excited and Exotic Muons in the mu+gamma Decay Channal in p-pbar Collisions at $\sqrt{s}$ 1.96 TeV", *Phys. Rev. Lett.* **97** (2006) 191802, `arXiv:0606043`. `doi:10.1103/PhysRevLett.97.191802`.

[23] The D0 Collaboration, "Search for Excited Muons in ppbar collisions at $\sqrt{s} = 1.96$ TeV", *Phys. Rev.* **D 73** (2006) 111102, `arXiv:0604040`. `doi:10.1103/PhysRevD.73.111102`.

[24] The CMS Collaboration, "Search for excited leptons in pp collisions at $\sqrt{s} = 7$ TeV", *Phys. Letter* **B 720** (2013) 309–329, `arXiv:1210.2422`. `doi:10.1016/j.physletb.2013.02.031`.

[25] The ATLAS Collaboration, "Search for excited electron and muons in $\sqrt{s} = 8$ TeV proton-proton collisions with the ATLAS detector", *New Journal of Phys.* **15** (2013) `arXiv:1308.1364`.

[26] L. Evans and P. Bryant, "LHC Machine", *Journal of Instrumentation 3* (2008), no. 08, S08001.

[27] The LEP Collaboration, "LEP design report", *CERN, Geneva* (1984).

[28] The ATLAS Collaboration, "The ATLAS Experiment at the CERN Large Hadron Collider", *Journal of Instrumentation 3* (2008), no. 08, S08003.

[29] The CMS Collaboration, "The CMS Experiment at the CERN LHC", *Journal of Instrumentation 3* (2008), no. 08, S08004.

[30] The LHCb Collaboration, "The LHCb Detector at the LHC", *Journal of Instrumentation 3* (2008), no. 08, S08005.

[31] The ALICE Collaboration, "The ALICE Experiment at the CERN LHC", *Journal of Instrumentation 3* (2008), no. 08, S08002.

[32] CERN, "The CERN accelerator complex". `http://cds.cern.ch/record/1260465`, 2008.

[33] The CMS Collaboration, "CMS-PHO-GEN-2012-002-5". `http://cds.cern.ch/record/1433717`, 2012.

[34] The CMS Collaboration, "The CMS Tracker System Project: Technical Design Report", 1998.

[35] The CMS Collaboration, "The CMS Electromagnetic Calorimeter Project: Technical Design Report", 1997.

[36] The CMS Collaboration, "The CMS Hadron Calorimeter Project: Technical Design Report", 1997.

[37] The CMS Collaboration, "The CMS Muon Project: Technical Design Report", 1997.

[38] The CMS Collaboration, "Performance of CMS muon detector in proton-proton collisions at $\sqrt{s} = 7$ TeV at the LHC", 2013.

[39] The CMS Collaboration, "The TriDAS Project: Technical Design Report, The Trigger System", 2000.

[40] I. Bird et al, "LHC Computing Grid: Technical Design Report". `http://cds.cern.ch/record/840543`, 2005.

[41] The CMS Collaboration, "Performance of CMS muon reconstruction and identification in pp collision events at $\sqrt{s} = 7$ TeV", 2012. `doi:10.1088/1748-0221/7/10/P10002`.

[42] G. Abbiendi et al., "Muon Reconstruction in the CMS Detector", *CMS Analysis Note AN-08-097* (2009).

[43] R. Frühwirth, "Application of Kalman filtering to track and vertex fitting", 1987. `doi:10.1016/0168-9002(87)90887-4`.

[44] Piotr Traczyk, "Muon Object Review". `https://indico.cern.ch/getFile.py/access?contribId=6&resId=0&materialId=slides&confId=172473`, 2012.

[45] Julien Caudron, "Retuning of muon cocktail for high p_T muons with fully segment based fit". `https://indico.cern.ch/getFile.py/access?contribId=7&resId=0&materialId=slides&confId=184964`, 2012.

[46] The CMS Collaboration, "CMSSW Application Framework, TWiki Website". `https://twiki.cern.ch/twiki/bin/view/CMSPublic/WorkBookCMSSWFramework`, 2013.

[47] J. Alwall et al., "MadGraph/MadEvent v4: the new web generation", *JHEP* **09** (2007) 028. `doi:10.1088/1126-6708/2007/09/028`.

[48] S. Alioli, P. Nason, C. Oleari et al., "NLO vector-boson production matched with shower in POWHEG", *JHEP* **07** (2008) 060. `doi:10.1088/1126-6708/2008/07/060`.

[49] T. Sjöstrand, S. Mrenna, and P. Z. Skands, "PYTHIA 6.4 Physics and Manual", *JHEP* **05** (2006) 026, `arXiv:0603175`.

[50] Z. Was, "TAUOLA the library for tau lepton decay", *Nucl. Phys. Proc. Suppl.* **98** (2001) 96–102, `arXiv:0011305`.

[51] J. Allison et al., "Geant4 developments and applications", *IEEE Trans. Nucl. Sci.* **53** (2006) 270. `doi:10.1109/TNS.2006.869826`.

[52] C. Magass et al., "Aachen 3A Susy Analysis, TWiki Website". `https://twiki.cern.ch/twiki/bin/viewauth/CMS/Aachen3ASusy`, 2011.

[53] The ROOT Team, "The ROOT User's Guide". `http://root.cern.ch/drupal/content/users-guide`, 2013.

[54] The CMS Collaboration, "CMS Luminosity Based on Pixel Cluster Counting - Summer 2013 Update", *CMS PAS LUM-13-001* (2013).

[55] The CMS Luminosity Group, "The official CMS Luminosity Calculation Tools, TWiki Website". `https://twiki.cern.ch/twiki/bin/viewauth/CMS/LumiCalc`, 2013.

[56] The CMS DQM Group, "Data Certification at DQM Group, TWiki Website". `https://twiki.cern.ch/twiki/bin/viewauth/CMS/DataCertificationatDQMGroup`, 2012.

[57] A. Martin, W. Stirlin, R. Thorne et al., "Parton distributions for the LHC", *Eur. Phys. J.* **C 63** (2009) 189–285, `arXiv:0901.0002`. `doi:10.1140/epjc/s10052-009-1072-5`.

[58] The CMS Collaboration, "Pileup Scenarios for MC, TWiki Website". `https://twiki.cern.ch/twiki/bin/viewauth/CMS/Pileup_MC_Gen_Scenarios`, 2012.

[59] P. Lenzi, S. Padhi, G. Gomez, C. Retuerto, F. Wuerthwein, "Standard Model Cross Sections for CMS at 8 TeV, TWiki Website". `https://twiki.cern.ch/twiki/bin/viewauth/CMS/StandardModelCrossSectionsat8Tev`, 2013.

[60] T. Binoth, N. Kauerm, and P. Mertsch, "Gluon-induced QCD corrections to $pp \to ZZ \to l\bar{l}l'\bar{l}'$", `arXiv:0807.0024`.

[61] The CMS Collaboration, "Measurements of the properties of a Higgs boson in the four-lepton final state", `arXiv:1312.5353`.

[62] LHC Higgs Cross Section Working Group, "Higgs cross section at 7, 8 and 14 TeV, TWiki Website". `https://twiki.cern.ch/twiki/bin/view/LHCPhysics/CrossSections#Higgs_cross_sections_at_7_8_and`, 2014.

[63] T. Sjöstrand, S. Mrenna, P. Skands, "A brief introduction to Pythia 8.1", *Computer Physics Communications* **178** (2008) 852–867, `arXiv:0710.3820v1`. `doi:10.1016/j.cpc.2008.01.036`.

[64] Julien Caudron, "Private Communication", 2012.

[65] Swapan Majhi, "QCD corrections to excited lepton (pair) production at LHC", *Phys. Rev.* **D 88** (2013) 074028, `arXiv:1210.8307`. `doi:10.1103/PhysRevD.88.074028`.

[66] M. Endres, T. Esch, T. Hebbeker, K. Hoepfner, C.-M. Kuo, S.-H. Mai, and Y. Maravin, "Search for excited leptons in the channel $ll^* \to llZ$ with four leptons in the final state", *CMS Analysis Note AN-13-263* (2013).

[67] The CMS Muon Object Group, "Baseline muon selections, TWiki Website". `https://twiki.cern.ch/twiki/bin/viewauth/CMSPublic/SWGuideMuonId`, 2013.

[68] The CMS Collaboration, "Muon Particle Object Group, TWiki Website". `https://twiki.cern.ch/twiki/bin/viewauth/CMS/MuonPOG`, 2013.

[69] M. Mulders, I. Block, E. James et al., "Muon Identification in CMS", *CMS Analysis Note AN-2008/098* (2008).

[70] The CMS Collaboration, "Commissioning of the Particle-Flow Reconstruction in Minimum-Bias and Jet Events from pp Collisions at 7 TeV", 2010.

[71] The CMS Collaboration, "Search for a narrow spin-2 resonance decaying to Z bosons in the semileptonic final state". `http://cds.cern.ch/record/1596494`, 2013.

[72] The CMS Collaboration, "Search for anomalous production of highly boosted Z bosons decaying to dimuons in proton-proton collisions at $\sqrt{s} = 7$ TeV", *Phys. Lett. B* **722** (2013) 28, `arXiv:1210.0867v2`. `doi:10.1016/j.physletb.2013.03.037`.

[73] The CMS Collaboration, "Search for W'/technirho in WZ using leptonic final states". `http://cds.cern.ch/record/1596494`, 2013.

[74] The CMS Collaboration, "Utilities for Accessing Pileup Information for Data, TWiki Website". `https://twiki.cern.ch/twiki/bin/viewauth/CMS/PileupJSONFileforData#2012_Pileup_JSON_Files`, 2013.

[75] The CMS Muon Particle Object Group, "Tag and Probe, TWiki Website". `https://twiki.cern.ch/twiki/bin/viewauth/CMS/MuonTagAndProbe`, 2013.

[76] The CMS Muon Particle Object Group, "Reference muon id and isolation efficiencies, TWiki Website". `https://twiki.cern.ch/twiki/bin/viewauth/CMS/MuonReferenceEffs`, 2013.

[77] The CMS Muon Particle Object Group, "Reference muon momentum scale and resolution, TWiki Website". `https://twiki.cern.ch/twiki/bin/viewauth/CMS/MuonReferenceResolution`, 2013.

[78] The CMS Collaboration, "Estimating Systematic Errors Due to Pileup Modeling, TWiki Website". `https://twiki.cern.ch/twiki/bin/viewauth/CMS/PileupSystematicErrors`, 2013.

[79] The CMS Collaboration, "Measurement of the ZZ production cross section and anomalous triliniar gauge couplings in lll'l' decays at $\sqrt{8} = 8$ TeV at the LHC", 2013.

[80] J. Heinrich et al., "Interval estimation in the presence of nuisance parameters. 1. Bayesian approach", `arXiv:0409129`.

[81] Matthias Endres, "Private Communication", 2013.

[82] The CMS Collaboration, "Documentation of the RooStats-based statistics tool for Higgs PAG, TWiki Website". `https://twiki.cern.ch/twiki/bin/viewauth/CMS/SWGuideHiggsAnalysisCombinedLimit`, 2013.

[83] The RooStats Collaboration, "RooStats page in CMS TWiki". `https://twiki.cern.ch/twiki/bin/viewauth/CMS/RooStats`, 2012.

[84] The CMS Collaboration, "HEEP Electron ID and isolation, TWiki Website". `https://twiki.cern.ch/twiki/bin/viewauth/CMS/HEEPElectronID`, 2012.

[85] The CMS Collaboration, "Boosted Z To Electrons - Modified Isolation, TWiki Website". `https://twiki.cern.ch/twiki/bin/viewauth/CMS/BoostedZToEEModIso`, 2012.

Danksagung

DANKE!

Selbständigkeitserklärung

Hiermit versichere ich schriftlich, dass ich die Arbeit selbstständig verfasst, keine anderen als die hier angegebenen Quellen und Hilfsmittel verwendet, sowie Zitate kenntlich gemacht habe.

_____
Ort, Datum

_____
Thomas Esch